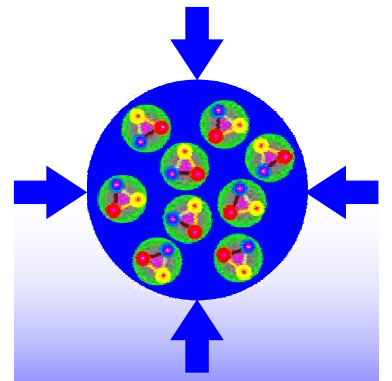
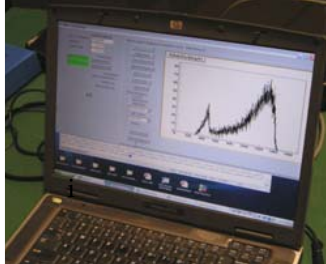
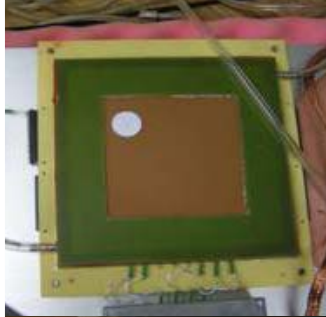
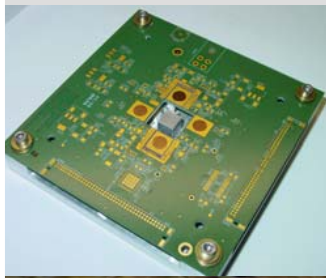
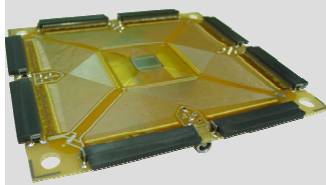
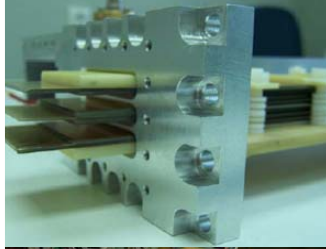
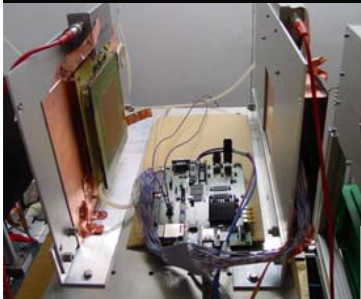
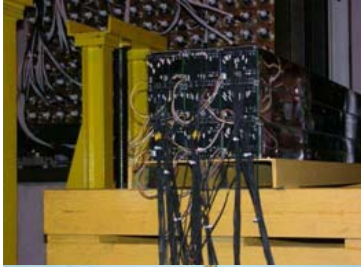
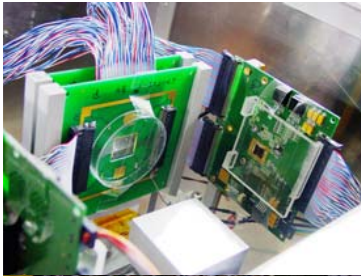
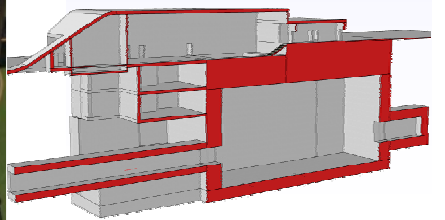


CBM PROGRESS REPORT 2008

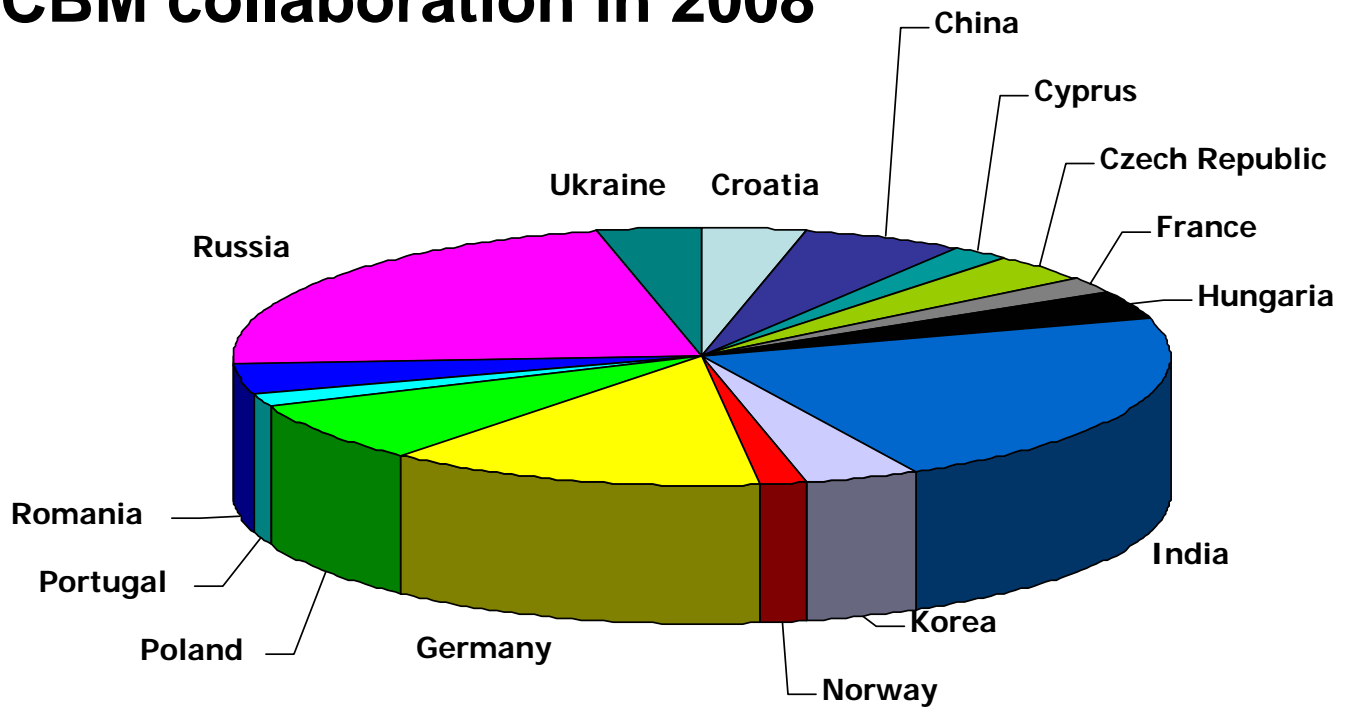


CBM

Compressed Baryonic Matter
experiment
at FAIR



CBM collaboration in 2008



Preface

This report reviews the activities within the CBM project in 2008. Substantial progress has been made in detector optimization by realistic feasibility studies, and in the development, construction and test of hardware components.

The track reconstruction studies for the Silicon Tracking System (STS) are now based on realistic detector response functions and cluster finding. A first small STS demonstrator module has been assembled and tested. The design of the next generation full-size CBM micro-strip prototype detector has been completed. The development of radiation hard detectors resulted in a new prototype wafer, designed and produced in 2008 in cooperation with CIS. The requirements concerning radiation hardness have been quantified by simulations using the FLUKA transport code which provided detailed information on the radiation dose distribution in the cave.

The development of fast algorithms for track and vertex reconstruction needed for online event selection advanced significantly. The Kalman filter based track fit used for the Silicon tracking system has been ported to a graphics card framework, and a throughput of about 22 million tracks/s has been achieved.

The feasibility studies of open charm identification have been performed for a detector setup with realistic material budget. The Micro-Vertex Detector (MVD) model now comprises sensors, cooling and support structure. The R&D on the MVD concentrates on the development of radiation hard and fast sensors. A large Monolithic Active Pixel Sensor with massive parallel read-out has been built and successfully tested. The construction of a demonstrator is in progress.

The Ring Imaging Cherenkov (RICH) detector has been reduced in size and number of read-out channels. The RICH design now is based on commercially available components like glass mirrors and multi-anode photomultipliers. The ring recognition algorithms have been improved to cope with the increased ring density. The optimization of the TRD concept resulted in a reduction of the number of stations and read-out channels. Real-size high-rate prototype detectors with a double gas layer and central pad readout are under construction.

The muon detector system has been further optimized with respect to the number and thickness of absorbers, and the number of detector layers. Feasibility studies of muon pair reconstruction have been performed for several beam energies and collision systems. A dimuon trigger concept has been developed. Prototype muon tracking chambers based on GEM technology have been built and tested. A prototype multi-layer segmented straw-tube detector has been built and tested. This technology is an option for the large area muon tracking chambers.

The FEE development for the RPC-TOF system proceeded with design and submission of the PADI preamplifier and GET4 digitizer ASICs. Studies of the radiation tolerance of UMC 180nm process used for many CBM ASICs gave very promising results.

A major milestone in 2008 was the successful test of detector and read-out systems with a proton beam at GSI in September 2008. The setup comprised two double-sided silicon micro-strip detectors and two GEM detectors coupled to a complete free streaming read-out chain consisting of front-end electronics (n-XYTER chips), read-out controllers, and the data acquisition system.

In 2008 four institutions joined the CBM collaboration: the University of Bucharest (Romania), the Institute for Nuclear Research (Kiev, Ukraine), the Gauhati University (Guwahati, India), the Tsinghua University (Beijing, China)

Many thanks to all the colleagues who have contributed to this report.

February 2009

Peter Senger

This work was supported by the EU Integrated Infrastructure Initiative HadronPhysics (I3HP) under contract number RII30CT-2004-506078, INTAS refs. 06-1000012-8914, 06-1000012-8729, 06-1000014-6110, the International Science & Technology Center (ISTC) under contract number 3540, the Bundesministerium für Bildung und Forschung (06FY173I, 06MN2291), the GSI Hochschulprogramm MAMAEN, and the Federal Agency of Russia for Atomic Research (ROSATOM).

GSI Report 2009-03
ISSN 171-4546
ISBN 978-3-9811298-6-1

Editors: Walter F. J. Müller and Volker Friese

© 2009 GSI Darmstadt, D-64291 Darmstadt, Germany
<http://www.gsi.de>

Printed in Darmstadt by GSI Darmstadt

Contents

Preface	iii
General	1
P. Senger: <i>Status of the CBM experiment at FAIR</i>	1
Micro-Vertex Detector	3
S. Seddiki et al.: <i>Occupancy study of the Micro-Vertex Detector for the CBM experiment</i>	3
C. Dritsa et al.: <i>Detector response simulation of the CBM Micro Vertex Detector</i>	4
M. Winter et al.: <i>A swift high resolution pixel sensor for the CBM MVD</i>	5
M. Deveaux et al.: <i>Radiation hardness studies on Monolithic Active Pixel Sensors</i>	6
S. Amar-Youcef et al.: <i>R&D for the demonstrator of the CBM-Micro-Vertex Detector (MVD)</i>	7
Silicon Tracking System	8
R. Karabowicz, A. Kotynia, and J. Heuser: <i>Progress with layout studies of the CBM Silicon Tracking System</i>	8
S. Chatterji and J. Heuser: <i>Development of radiation hard silicon detectors for the CBM Silicon Tracking System using simulation approach</i>	9
J. Heuser et al.: <i>Development of microstrip detectors for the CBM Silicon Tracking System</i>	10
J. Heuser et al.: <i>First test of a prototype CBM silicon detector system in a proton beam at GSI</i>	11
V. M. Borshchov et al.: <i>Design and assembly of STS demonstrator module 0-B</i>	12
Y. Murin et al.: <i>Test of STS demonstrator module 0-B in a 50 GeV proton beam</i>	13
V. Pugatch et al.: <i>Characterization of CBM01 sensors for the Silicon Tracking System</i>	15
V. Pugatch et al.: <i>Laser stand for testing STS silicon microstrip detector modules</i>	16
V. Pugatch et al.: <i>Supporting frame and microcable properties for the STS microstrip detector module prototype</i>	17
V. Jakovlev et al.: <i>Radiation hardness tests of silicon microstrip detectors with the KRI cyclotron</i>	18
S. N. Igolkin et al.: <i>Ultra light-weight carbon-fiber structures for the CBM Silicon Tracking System</i>	19
Ring Imaging Cherenkov Detector	20
S. Lebedev, E. Belolaptikova, and C. Höhne: <i>Layout study of the RICH detector in the CBM experiment</i>	20
M. Dürr, A. Braem, and C. Höhne: <i>Development of a CBM-RICH mirror prototype – first measurements</i>	21
J.G. Yi et al.: <i>Research & Development of a mini-RICH Detector with gas radiator as first step towards a CBM-RICH prototype</i>	22
V. Brekhovskikh et al.: <i>Progress in photodetector development for the CBM RICH</i>	24
P. Koczon et al.: <i>Investigation of wavelength shifter properties of p-terphenyl and TPB</i>	26
Muon System	27
A. Kiseleva et al.: <i>Optimization of the CBM muon detection system</i>	27
E. Kryshen, V. Nikulin, and M. Ryzhinskiy: <i>Detailed geometry for MUCH tracker and FEE requirements</i>	28
D. Dutta, A. Kiseleva, and C. Höhne: <i>Segmentation study of the CBM muon detector</i>	29
P. Garg et al.: <i>Preliminary simulation results of THGEM geometry and detector gas for the CBM muon detector</i>	30
E. Chernyshova et al.: <i>R&D of Micromegas, GEM, TGEM and GEM/Micromegas based detectors for the CBM muon detection system</i>	31
A.K. Dubey et al.: <i>Multi-GEM prototypes for muon detection in CBM experiment</i>	32
A. Zinchenko et al.: <i>Feasibility evaluation of the straw tube detector option for the CBM muon system</i>	34
V. Peshekhonov et al.: <i>Segmented straw tubes for CBM-MUCH</i>	35

Transition Radiation Detectors	36
V. Ivanov et al.: <i>Layout study of the TRD in the CBM experiment</i>	36
D. Gonzalez-Diaz et al.: <i>The rate challenges of the CBM-TRD</i>	37
S. Chernenko et al.: <i>Research and development of fast gas detectors for the CBM experiment</i>	38
Resistive Plate Chambers	39
L. A. Diaz et al.: <i>Low resistivity materials for the low polar angle of the CBM-TOF wall</i>	39
A. Berezutskiy et al.: <i>Cross-talk studies oriented to stripped tRPCs at high multiplicities</i>	40
V. Ammosov et al.: <i>Progress for high rate glass tRPCs with pads</i>	41
D. Bartos et al.: <i>In-beam test results of the Pestov Glass Resistive Plate Counter prototypes</i>	42
I. Deppner et al.: <i>Characterisation of FOPI narrow strip RPCs</i>	43
Calorimeters	44
S. Belogurov et al.: <i>Reconstruction of photons and reoptimization of the CBM calorimeter system</i>	44
A. Artamonov and Y. Kharlov: <i>Particle identification in ECAL with longitudinal segmentation</i>	46
A. Akindinov et al.: <i>Prototypes of muon system and preshower counters</i>	48
Magnet	50
E.A. Matyushevskiy et al.: <i>SC dipole magnet for CBM</i>	50
FEE and DAQ	51
K. Kasinski, A. Czermak, and R. Szczygiel: <i>Test results of n-XYter silicon strip readout chip</i>	51
S. Löchner: <i>Radiation studies on the UMC 180 nm CMOS process</i>	52
T. Armbruster, P. Fischer, and C. Kreidl: <i>Front-end electronics for CBM</i>	53
M. Ciobanu et al.: <i>PADI2-3, the second iteration of FEE for CBM time-of-flight measurements</i>	54
H. Flemming and H. Deppe: <i>The GSI event-driven TDC with 4 channels GET4</i>	55
N. Abel et al.: <i>Software development for CBM readout controller board</i>	56
F. Lemke and U. Brüning: <i>A generic link protocol for the CBM DAQ system</i>	57
W. Gao et al.: <i>Improved Active Buffer Board of CBM</i>	58
J. Adamczewski-Musch et al.: <i>Data Acquisition Backbone Core DABC v1.0</i>	59
Physics Performance	60
I. Vassiliev and I. Kisel: <i>D^0 decay feasibility study in the CBM experiment</i>	60
I. Vassiliev and I. Kisel: <i>D^+ decay feasibility study in the CBM experiment</i>	61
I. Vassiliev and I. Kisel: <i>$H - \text{dibaryon} \rightarrow \Lambda\Lambda$ detectability study in the CBM experiment</i>	62
D. Kresan and C. Höhne: <i>Event-by-event fluctuations of the K/π yield ratio in the CBM experiment</i>	63
T. Galatyuk, C. Höhne, and J. Stroth: <i>Systematic investigations on di-electron reconstruction in CBM</i>	64
A. Maevskaya, C. Höhne, and A. Kurepin: <i>Feasibility study for a J/ψ trigger in the electron-positron decay mode</i>	65
M. Klein-Bösing et al.: <i>Measurement of direct photons via conversions into e^+e^- pairs in CBM</i>	66
A. Kiseleva et al.: <i>Muon measurements at different beam energies in CBM</i>	67
A. Kiseleva et al.: <i>Muon reconstruction at high particle multiplicities in CBM</i>	68
A. Kiseleva et al.: <i>The di-muon trigger for CBM</i>	69
P. Bhaduri, S. Chattopadhyay, and P. Ghosh: <i>Development of a trigger algorithm for the measurement of rare probes in the CBM experiment at FAIR</i>	70
S. M. Kiselev: <i>Feasibility study of $\eta \rightarrow \gamma\gamma$ reconstruction with ECAL</i>	71
V. Pozdnyakov and Y. Vertogradova: <i>Study of hadron azimuthal correlations with CBM</i>	72
D. Bertini and E. Paulova: <i>CBM radiation levels study</i>	73
Software and Algorithms	74
M. Al-Turany and F. Uhlig: <i>Status of the FairRoot simulation and analysis framework</i>	74
M. Al-Turany, K. Schwarz, and F. Uhlig: <i>GRID setup for CBM</i>	75
D. Golubkov et al.: <i>Cellular automaton track finder in a realistic STS detector geometry</i>	76
H. Bjerke et al.: <i>Scalability of a Kalman filter based track fit on Intel many-core CPUs</i>	77
M. Bach et al.: <i>Porting a Kalman filter based track fit to NVIDIA CUDA</i>	78
I. Kisel, I. Kulakov, and I. Vassiliev: <i>A standalone package for on-line event selection in the CBM experiment</i>	79
C. Steinle, A. Kugel, and R. Männer: <i>Implementation of a Hough Tracker for CBM</i>	80
A. Lebedev et al.: <i>Track reconstruction in the MUCH and TRD detectors of CBM</i>	81

T. P. Akishina, O. Y. Denisova, and V. V. Ivanov: <i>Study of the electron energy losses in the TRD</i>	82
T. P. Akishina, O. Y. Denisova, and V. V. Ivanov: <i>Systematic study of e/π identification with the TRD applying a multilayer perceptron</i>	83
S. Lebedev, C. Höhne, and G. Ososkov: <i>Electron identification in the CBM experiment</i>	84
S. Lebedev and G. Ososkov: <i>Wavelet application for handling invariant mass spectra</i>	85
Appendices	86
Publications 2008	86
CBM Notes 2008	87
CBM Meetings, Workshops, Conferences	87
List of Institutions	88
Contacts	90

Status of the CBM experiment at FAIR

P. Senger
GSI Darmstadt

Observables and experimental challenges

The Compressed Baryonic Matter (CBM) experiment at FAIR is designed to explore the QCD phase diagram in the region of high baryon densities. With CBM we will enter a new era of nuclear matter research by measuring rare diagnostic probes never observed before at FAIR energies, and thus CBM has a unique discovery potential. In order to obtain a complete picture, a comprehensive set of observables will be measured in proton-proton, proton-nucleus, and nucleus-nucleus collisions over the full FAIR energy range. The observables include particles containing charm quarks (D-mesons and charmonia), low-mass vector mesons decaying into lepton pairs (ρ , ω and ϕ mesons), and Ω hyperons (consisting of 3 strange quarks). The measurement of event-by-event fluctuations, correlations, and of the collective flow of hadrons (including rare probes) will provide important information on the dynamics of the fireball.

The experimental challenge is to identify hadrons and leptons in collisions with up to 1000 charged particles at event rates of up to 10 MHz. These measurements require fast and radiation hard detectors, free-streaming read-out electronics, online event-selection based on future CPU/GPU architectures, and a high-speed data acquisition (DAQ) system. Particularly demanding is the measurement of particles with open charm which is based on the real-time selection of displaced vertices with an accuracy of 50 μm .

The CBM experimental facility

The CBM detector system comprises various components. Inside a large aperture dipole magnet there is a Silicon Tracking and Vertexing System which consists of two parts: a Micro-Vertex Detector (MVD, 2 silicon pixel layers) and the Silicon Tracking System (STS, up to 8 layers of silicon micro-strip detectors). The Silicon detector array has to provide the capabilities for track reconstruction, determination of primary and secondary vertices, and momentum determination. A large-area detector array consisting of Resistive Plate Chambers (RPC) serves for hadron identification by measuring the particle time-of-flight with high precision. An electromagnetic calorimeter (ECAL) will be used for the identification of photons. Projectile spectator fragments will be detected with a hadron calorimeter (PSD). Both calorimeters are based on lead/scintillator "Shashlik" technology. Electron-positron pairs from the decay of low mass vector mesons will be identified by a Ring Imaging Cherenkov (RICH) detector

and a Transition Radiation Detector (TRD). The upper part of Fig. 1 depicts the CBM experimental setup with RICH and TRD. The RICH will be constructed such that it can be removed and replaced by a muon detection system consisting of hadron absorber layers (made of iron) sandwiched by large area tracking detector layers (see lower part of Fig. 1). In the following we briefly review the status of the feasibility studies and the detector R&D for CBM.

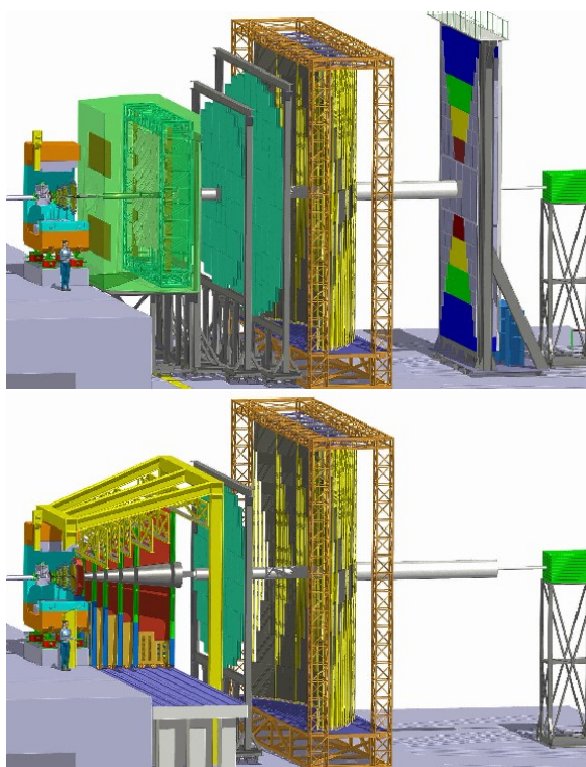


Figure 1: The Compressed Baryonic Matter (CBM) experiment at FAIR with RICH and TRD (upper part), and with the muon detection system replacing the RICH (lower part).

The Silicon Tracking System

Progress with the development of the Silicon Tracking System was achieved in several fields. The prototype micro-strip detectors CBM01, designed and produced in 2007, were assembled into a first small STS demonstrator system. Equipped with prototypes of self-triggering front-end electronics, the system was successfully tested with a 2.5 GeV proton beam at GSI. Another demonstrator system consisting of micro-strip detectors read out through

first prototypes of ultra-thin micro-cables was successfully tested with a 50 GeV proton beam at IHEP Protvino. The CBM demonstrator was integrated into the beam tracker of the SVD-2 experiment and contributed to data taking. The simulation studies of the STS system were improved by implementing realistic detector response functions and cluster finding at the input of the track reconstruction code. The next generation full-size CBM micro-strip prototype detector has been simulated and its performance has been assessed. The development of radiation hard detectors has been addressed with the prototype wafer CBM02, designed and produced in 2008 in cooperation with CIS, Erfurt. It provides various test detectors to explore several radiation tolerant designs. Simulation tools are being set up at GSI to carry out detailed calculations of the radiation tolerance of forthcoming CBM silicon detectors.

D meson identification and vertex detector

The Micro-Vertex Detector (MVD) is needed for open charm measurements which require high-precision vertexing. The MVD consists of two layers of silicon pixel detectors composed of Monolithic Active Pixel Sensors (MAPS) which can be made very thin in order to reduce multiple scattering. The R&D on the MVD concentrates on the development of radiation hard and fast sensors. A large MAPS with massive parallel read-out was built and successfully tested. The construction of a demonstrator is in progress. Feasibility studies were performed for the measurement of particles with open charm (D^0 , D^\pm , D_s , and Λ_c) using a detector setup consisting of the MVD and 8 double-sided micro-strip silicon detector stations. The MVD was implemented with a realistic material budget which includes sensors, cooling, and support structure.

Hadron identification by time-of-flight

Hadron identification in CBM is performed by combining the tracks in STS and TRD with hits in the timing RPC. The total reconstruction efficiency is on the level of 86%. With 80 ps time resolution, kaons and pions are separated by 2σ in the squared mass distribution for $p < 3.5$ GeV/c. To achieve a certain purity of selected kaons for e. g. the study of event-by-event K/π fluctuations, momentum cut-offs have to be applied. Simulations demonstrate that this procedure results in a systematic increase of dynamical fluctuations on the order of (1-2)% compared to an analysis in the full momentum range. The R&D on prototype timing RPCs concentrates on high rate capability, low resistivity material, long term stability, and the realization of large arrays with overall excellent timing performance.

Electron identification with RICH and TRD

The gaseous RICH detector was redesigned in order to reduce its size and costs without loss of performance. This was achieved by changing the radiator from N_2 to CO_2 , and by improving the ring recognition algorithm for high

ring densities. Detailed simulations showed that 6 mm thick glass mirrors and an aluminum support structure do not deteriorate the global tracking performance. First glass mirror prototypes purchased from a standard production process from FLABEG, Germany, were tested and showed good reflectivity while still having a deficiency in surface homogeneity. The use of wavelength-shifter films for an enhanced number of measured Cherenkov photons is reinvestigated and shows promising results. The TRD concept was optimized such that it is possible to reduce the number of stations. Real-size prototype detectors with a double gas layer and central pad readout are under construction. This technology is well suited for high-rate operation and will be used in inner part of the TRD stations. For the detectors placed in the outer parts of the stations, the rate requirements are less harsh, and the gas gap could be larger. Simulations for low-mass dileptons and charmonium clearly show the feasibility of these measurements. The development of a J/ψ trigger algorithm is in progress.

Muon measurements with hadron absorbers

The CBM muon detector consists of an alternating absorber detector system located just behind the Silicon Tracking System (STS). Optimized tracking routines provide a tracking efficiency of more than 95% for muons passing the absorber. The largest source of background tracks are muons from weak decays of hadrons in the muon absorber system. The track reconstruction efficiency is robust against additional background from uncorrelated and correlated noise hits. The muon detector system was optimized with respect to the number and thickness of absorbers, and the number of detector layers. A flexible detector segmentation algorithm was developed to find a compromise between track reconstruction efficiency and number of readout channels. Feasibility studies on muon pair reconstruction were performed for several beam energies and collision systems. Finally, a dimuon trigger concept was developed. The muon detector development concentrates on the construction and test of prototype gaseous detectors based on GEM technology. A successful test of prototype GEM detectors coupled to a free-streaming data read-out and acquisition system was performed at GSI with a proton beam.

Online event selection

A stand alone package for on-line event selection was developed in order to investigate its performance on different modern and future CPU/GPU architectures. A Kalman filter based track fitting procedure was ported to NVIDIA graphics cards. As a result, the speed of track reconstruction could be improved to 46 ns/track. The scalability of the SIMD Kalman filter based track fit was investigated on different multi-core CPU systems.

Occupancy study of the Micro-Vertex Detector for the Compressed Baryonic Matter experiment

S. Seddiki^{1,2}, M. Deveaux¹, I. Fröhlich¹, C. Müntz¹, J. Stroth^{1,3}, and C. Trageser¹

¹IKF, Frankfurt, Germany; ²IPHC, Strasbourg, France; ³GSI, Darmstadt, Germany

The Micro-Vertex Detector (MVD) [1] of CBM is intended to detect the hadronic decays of open charmed particles by means of the identification of their displaced decay vertex. Therefore the MVD has to be located close to the collision point and will be exposed to the intense particles flux from the high heavy ion collision rates foreseen in CBM. The design of the MVD requires a detailed knowledge of the detector occupancies and the corresponding data rates, which were simulated in this work.

We focused on the study of δ -electrons, which are produced by the Au beam passing the Au target. They were generated with GEANT3+GALOR by shooting Au ions with 25 AGeV through the target of CBM. The yield and spectrum of the simulated δ -electrons were compared with literature [2] and exceed this prediction by few 10% in the electron momentum region of interest ($p = 10$ MeV/c to $p = 100$ MeV/c). Accounting for the 1% interaction target, 100 of those ions were combined with the particles produced by one UrQMD nuclear collision with random impact parameter. This normalization assumes that the time resolution of the MVD is sufficient to separate the individual nuclear collisions.

After some centimeters of trajectory, the 1 Tm dipole field of CBM deflects most of the δ -electrons out of the detector acceptance. The occupancy of the MVD stations thus varies strongly with the distance (dz) between the stations and the target (fig. 2). Moreover, the occupancy of individual stations is very inhomogeneous (fig. 1 right).

The contribution of the δ -electrons increases the mean occupancy caused by a nuclear collision by factors of 13.5 and 5 at $dz = 5$ cm and $dz = 10$ cm, respectively (fig. 2). The maximal occupancy in the hot spots reaches 3.5 and 1 hit/mm²/collision at $dz = 5$ cm and $dz = 10$ cm, respectively (see the right panel of fig. 1).

In order to reduce those high occupancies, the exami-

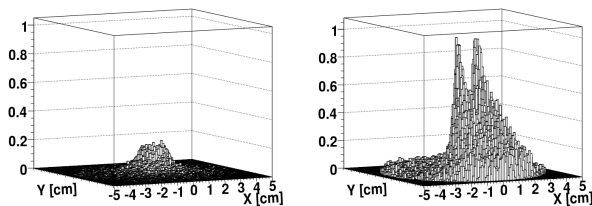


Figure 1: Number of hits per cell (1 mm²) per collision for a MVD station at $dz = 10$ cm originating from nuclear collisions only (left panel) and including δ -electrons (right panel)

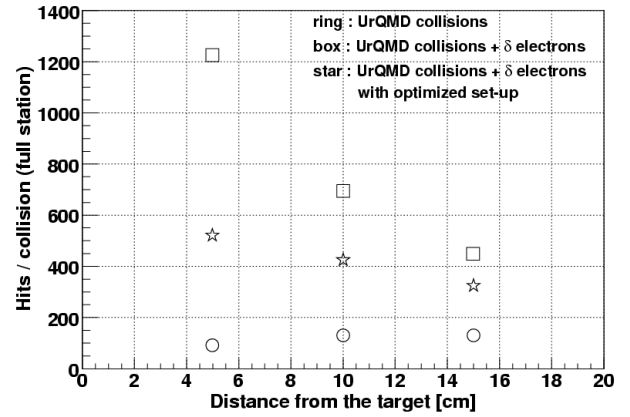


Figure 2: Occupancy per event for different distances (dz) of the MVD station

nation of the deposition time of the hits permitted us to elaborate several strategies. We observed that raising the magnetic field by 1 T within a small volume around the target improves the deflection of δ -electrons and decreases the number of prompt hits. This modified field configuration increases the amount of late coming hits from spiraling electrons, absorbed however by the mechanical support ring of the MVD stations. This strategy reduces the total occupancy by factors of 2.5 and 2 at $dz = 5$ cm and $dz = 10$ cm, respectively (fig. 2). Nevertheless, the peak of occupancy is only decreased by 30% at both distances, as it is caused by very stiff electrons.

Our studies were completed by estimating the data flow of the MVD. We assumed a collision rate of $10^5/s$ and an on-chip zero suppression as tested with SUZE-01 [3]. The resulting data flow of several GBits/s per station may be increased by one order of magnitude if the MVD is operated with a moderate pile-up of nuclear collisions. Moreover, a security margin for fake hits has to be foreseen.

References

- [1] A. Besson et al., *Achievement of CMOS Pixel Sensors for the CBM Micro-Vertex Detector*, CBM Progress Report 2007, Darmstadt, 2008
- [2] R. M. Barnett et al., *Phys. Rev. D* 54 (1996) p. 134
- [3] M. Winter et al., *A Swift High Resolution Pixel Sensor for the CBM MVD*, this report

Detector response simulation of the CBM Micro Vertex Detector

C. Dritsa^{1,2}, J. Baudot², R. De Masi², M. Deveaux³, V. Friese¹, F. Rami², and M. Winter²

¹GSI, Darmstadt, Germany; ²IPHC, Université de Strasbourg, Strasbourg, France; ³IKF, Johann Wolfgang Goethe-Universität, Frankfurt, Germany

One of the major physics topics of the CBM experiment is the study of the production of open charm in nucleus-nucleus collisions at FAIR energies. For this purpose, the CBM Collaboration is planning to use a high-performance Micro-Vertex Detector (MVD) based on Monolithic Active Pixel Sensors (MAPS) [1]. CBM running conditions call for a MVD with high granularity, radiation tolerance, and readout speed. The efficient optimisation of the detector design requires detailed simulations of the detector response.

So far, the MVD detector response in the CBM simulation software (CBMRoot) [2] has been described by applying a Gaussian smearing of the hit position provided by GEANT. This simple approach ignores effects like generation of clusters of pixels from impinging particles and is therefore not suited for reproducing the high track-density environment of the MVD. In the present work, we implemented a more realistic MVD detector response simulation program based on a software package which was developed recently within the framework of the ILC in order to describe the response of MAPS sensors to the passage of charged particles [3]. This package employs a MAPS response model which takes into account the sensitive volume of the sensor, its pixel structure, and its intrinsic noise. The path of a charged particle traversing the thin sensitive layer of the detector is subdivided into n segments. The energy deposited by the particle in the silicon is translated into a signal charge using a conversion factor of 3.62 eV per electron/hole pair. The diffusion of the signal electrons in the sensitive layer of the sensor is modeled by a Gaussian distribution with width tuned to measured data. This allows to convert the hit associated to the particle trajectory into a charge distributed over several pixels. It is possible to simulate the readout with a discrimination threshold and a digitisation with up to 12 bit ADC.

A cluster finder algorithm was also implemented in the CBM simulation framework in order to reconstruct the hit position on the readout plane. This is done by determining the center-of-gravity of the charge stored in the fired pixels.

The model was validated with real data collected with a MAPS prototype, called MIMOSA-17 (30 μm pixel pitch, 14 μm thick epitaxial layer), exposed to a 120 GeV/c pion beam at the CERN-SPS. On the left of Fig. 1, the probability is shown that the charge collected by neighbours of an already identified seed pixel (index 0) exceeds the discrimination threshold of 75 electrons (5 times the noise of MIMOSA-17) for simulated and for real data. If restricted to this comparison, an excellent agreement is observed between experiment and simulation for particles with incident

angles of 40° - 90° with respect to the detector's plane; nevertheless, disagreements observed for very small incident angles (10° - 30°), e.g. in reproducing the cluster shape, remain to be investigated.

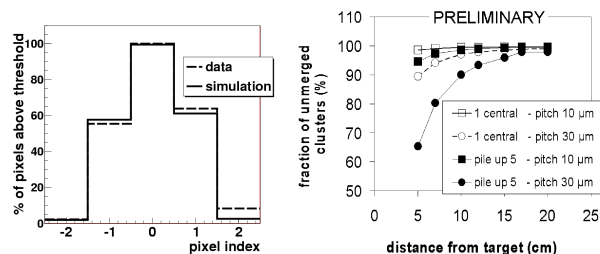


Figure 1: (Left) Percentage of pixels above threshold for the row of the cluster to which the seed pixel belongs. The impinging particle's trajectory is vertical to the detector plane (90°). (Right) Percentage of unmerged clusters as a function of distance between the station and the target, for different combinations of pile-up and pixel pitch. A pile-up of 5 collisions is defined as 1 central and 4 minimum bias collisions.

A typical objective of the digitiser is illustrated in Fig. 1 (right), where the evolution of cluster merging with respect to the distance of each station from the target is studied for different assumptions. Cluster merging occurs if several individual clusters get combined in a single one after cluster reconstruction. Because of the high collision rate, several collisions may pile up in a single MVD readout cycle. One of the consequences of this pile-up is an increased probability that clusters merge. The merging probability is governed by pixel size and track density and, hence, by the distance to the target.

The software is now mature for the detailed studies needed to optimise the MVD conceptual geometry, accounting for the most influential parameters such as radiation hardness, occupancy, pixel pitch, and readout speed. These studies will incorporate software improvements mitigating the residual discrepancies between real and simulated data.

References

- [1] <http://iphc.cnrs.fr/~CMOS-ILC-.html>
- [2] M. Al-Turany and F. Uhlig, *FairRoot Framework*, submitted to Proceedings of Science (ACAT08)
- [3] M. Battaglia, Nucl. Instr. Meth. Phys. Res. A572 (2007) 274

A swift high resolution pixel sensor for the CBM MVD *

M. Winter, J. Baudot, A. Besson, A. Brogna, G. Claus, C. Colledani, R. De Masi, A. Dorokhov, G. Dozière, W. Dulinski, M. Goffe, A. Himmi, Ch. Hu-Guo, K. Jaaskelainen, F. Morel, I. Valin, and G. Voutsinas

IPHC, Strasbourg, France

Introduction

Swift, high resolution CMOS pixel sensors are being developed for the CBM Micro Vertex Detector (MVD), allowing for high density particle tracking. Designed at IPHC, the sensors are manufactured by the CMOS industry and can be thinned down to $\leq 50 \mu\text{m}$.

To accommodate the data rate, the signals delivered by the sensors are discriminated before being filtered by an integrated zero-suppression logic. A fast read-out is achieved by grouping the pixels composing the sensitive area in columns read out in parallel. The development of this architecture relies on two parallel tasks. One of them addresses the upstream part of the signal conditioning chain, including the pixel array and the discriminators ending the columns. The other concerns the downstream part, combining a zero-suppression logic with output memories.

Pixel array with binary outputs

Small prototypes were fabricated and tested in previous years to develop the upstream part of the sensor architecture [1]. *MIMOSA-22* is the final prototype of this R&D line supported by the European project EUDET [2]. Two complementary versions were designed and fabricated. They were both characterised in 2008, first at IPHC with an ^{55}Fe source and next at the CERN-SPS, mounted on a silicon-strip beam telescope.

The sensor features 136 columns read out in parallel, each containing 576, $18.4 \mu\text{m}$ pitch, pixels. 128 columns are ended with a discriminator, while 8 columns have analog outputs for test purposes. The chip incorporates a JTAG controller. The frame read-out time is $92.5 \mu\text{s}$. Various pixel designs were integrated in the chip, allowing to explore different sensing diode sizes, amplification schemes, ionising radiation tolerant designs, etc.

A modest noise value was found for most pixel designs, ranging from about 10 to $14 e^- \text{ENC}$, with a mild operating temperature dependence. The 128 discriminators exhibited a modest threshold dispersion ($\pm 4 \%$ standard deviation) and contributed marginally to the total noise. No significant non-uniformity was found over the sensitive area of any of the 6 sensors tested.

When exposed to a 120 GeV π^- beam at the CERN-SPS, a signal-to-noise ratio in the range 17–21 (most probable value) was observed, depending on the pixel design. Table 1 illustrates the measured detection performances.

*Work supported by the European project EUDET(FP6) and GSI.

Threshold	Detection eff.	Fake rate	Resolution
3 mV	99.8 ± 0.05 (stat) %	$\sim 4 \cdot 10^{-4}$	$\sim 3.7 \mu\text{m}$
4 mV	99.7 ± 0.05 (stat) %	$\sim 7 \cdot 10^{-5}$	$\sim 3.5 \mu\text{m}$

Table 1: Detection efficiency, average fake hit rate and single point resolution measured at the CERN-SPS with *MIMOSA-22* for two discriminator threshold values.

The observed detection efficiency remains $> 99.5 \%$ for threshold values high enough to keep the fake hit rate $< 10^{-4}$, a value ensuring that the signal processing micro-circuits will not be saturated by pixel noise fluctuations. The single point resolution is $< 4 \mu\text{m}$, well below the MVD requirement of $\lesssim 5 \mu\text{m}$. These results validate the architecture for its integration in the complete sensor.

Zero-suppression micro-circuit

SUZE-01 incorporates the zero-suppression micro-circuit and output memories composing the downstream part of the sensor architecture. Fabricated in 2007 within the EUDET project, it was tested extensively at IPHC until Spring 2008 with millions of patterns at its nominal clock frequency (100 MHz) and above. No failures were spotted for frequencies ≤ 115 MHz. This guarantees that the architecture is suited to the complete sensor specifications.

Towards a complete sensor

A complete, full scale, sensor (called *MIMOSA-26*) was designed in 2008 within the EUDET project and sent for fabrication. It combines the architecture of *MIMOSA-22* and *SUZE-01* in a comprehensive charge sensing and signal read-out chain, providing discriminated signals in a binary mode including the pixel address. It features 1152 columns of 576 pixels, read out in $\sim 100 \mu\text{s}$. It will be extensively tested in 2009 and equip the final version of the EUDET telescope. If satisfactory, this architecture will next be evolved progressively to shorter read-out time, aiming for the target value of $\sim 10 \mu\text{s}$ required for the MVD.

References

- [1] M. Winter et al., "Achievements of CMOS Pixel Sensors for the CBM Micro-Vertex Detector", GSI Scientific Report 2007.
- [2] EUDET collaboration, "Detector R&D towards the International Linear Collider", supported by the E.U. within FP6, <http://www.eudet.org/>.

Radiation hardness studies on Monolithic Active Pixel Sensors*

M. Deveaux¹, S. Amar-Youcef¹, J. Baudot², A. Büdenbender¹, D. Doering¹, W. Dulinski²,
M. Koziel², C. Müntz¹, J. Stroth¹, F. M. Wagner³, and M. Winter²

¹Goethe University Frankfurt, Frankfurt/Main, Germany; ²IPHC Strasbourg, France; ³Forschungsneutronenquelle Heinz Maier-Leibnitz (FRM II), Technische Universität München, Garching, Germany

CMOS Monolithic Active Pixel Sensors (MAPS) form a promising sensor technology for the micro vertex detector (MVD) of the Compressed Baryonic Matter (CBM) experiment. The technology allows for building very thin ($\sim 50 \mu\text{m}$) detectors with a spatial resolution of few μm and a satisfactory time resolution of $10 \mu\text{s}$. It is expected that within one run of CBM, the MVD will be exposed to a radiation dose of $\sim 3 \text{ Mrad}$ and $10^{13} \text{ n}_{\text{eq}}/\text{cm}^2$. A joined research program of GSI, the Goethe University Frankfurt and the IPHC Strasbourg aims to expand the radiation tolerance of MAPS beyond this level.

Our activities in 2008 followed three research lines which were the study of the Random Telegraph Signal observed in irradiated sensors[1], the search for improved sensor designs based on conventional CMOS processes and the identification and evaluation of dedicated CMOS processes allowing for building depleted sensors.

RTS is a non-Gaussian noise of CMOS components. As illustrated in figure 1, it manifests itself as a rectangular modulation of the dark signal of neutron irradiated MAPS, which is sufficient to exceed the discrimination threshold of the sensor and to generate false hit indications. We studied RTS as function of temperature and radiation dose with MIMOSA-18¹ and MIMOSA-19² prototypes, which were irradiated with fission neutrons [2] at the MEDAPP facility of the FRM II reactor. We observed that up to few 10% of all pixels show occasionally RTS signatures. However, at a temperature of -20°C , the SB-pixels of MIMOSA-18 showed a reasonably low fake hit rate of $\ll 10^{-4}$ after a dose of $10^{13} \text{ n}_{\text{eq}}/\text{cm}^2$. This low rate (one order of magnitude lower than observed with the conventional 3T-pixels of MIMOSA-19) is due to the intrinsic leakage current compensation of the SB-pixels.

Our studies on MIMOSA-18 and -19 aimed also to test strategies to improve the signal over noise ratio (S/N) of MAPS being irradiated with non-ionizing doses. This S/N is mostly degraded by a drop of the charge collection efficiency (CCE) of the sensor, which is due to the shrinking lifetime of the signal electrons in silicon suffering from radiation induced bulk damage. The CCE is partially recovered if an accelerated charge collection process collects the electrons before they recombine. As already demonstrated [3], this acceleration may be reached by reducing the pixel pitch, which however substantially increases the number of

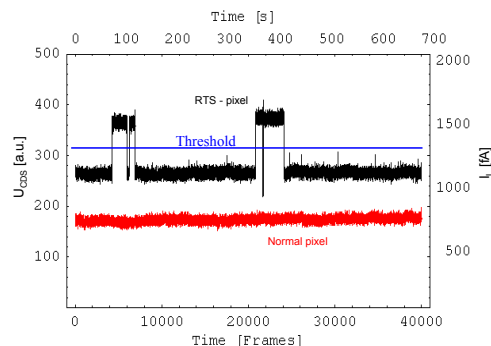


Figure 1: Dark signal of a 3T-pixel showing RTS (black) and of a normal pixel (red/gray).

channels in the MVD. An alternative strategy, the use of big sensing diodes, was tested with MIMOSA-19.

The CCE and radiation hardness of this chip was studied with a ^{55}Fe source and compared with the performances of the conventional pixels of MIMOSA-18. As expected, the pixels of MIMOSA-19 reach a significantly higher CCE than the pixels of MIMOSA-18 but show also a substantially higher capacitive noise ($\sim 20\text{e ENC}$ instead of $\sim 12\text{e ENC}$). The S/N of MIMOSA-19 is therefore smaller than the one of MIMOSA-18. However, according to our preliminary results, MIMOSA-19 is expected to show a fairly good detection efficiency ($> 95\%$ for MIPs) up to the highest neutron dose applied ($2 \cdot 10^{13} \text{ n}_{\text{eq}}/\text{cm}^2$).

An even higher radiation tolerance might be reached by depleting the sensors, which is however not compatible with the highly (some $10^{15} \text{ at}/\text{cm}^2$) doped silicon of standard CMOS processes. This attracted our attention to the XFAB $0.6 \mu\text{m}$ process, which includes a substantially lower doped epitaxial layer. A prototype (MIMOSA-25) featuring partially depleted sensors was designed in order to evaluate this process. First promising test results from neutron irradiated MIMOSA-25 were obtained.

References

- [1] J. Bogaerts, B. Dierickx, R. Mertens, “Random Telegraph Signals in a Radiation-Hardened CMOS Active Pixel Sensor”, *IEEE Trans. Nucl. Sci.* **49**, 249 (2002).
- [2] H. Breitschütz, F. M. Wagner, A. Rührmoser, W. Petry, “Spectral fluence rates of the fast reactor neutron beam MedApp at FRM II”, *Nucl. Instrum. Meth. A* **593**, 466 (2008).
- [3] A. Besson et al., “Achievements of CMOS Pixel Sensors for the CBM Micro-Vertex Detector”, *GSI Scientific Report* 2007.

* Supported by BMBF (06FY173I), GSI Darmstadt (F&E) and Helmholtz Research School Frankfurt

¹262k pixels with $10 \mu\text{m}$ pitch, $15 \mu\text{m}^2$ collection diodes.

²73k pixels with $12 \mu\text{m}$ pitch, 40 and $57 \mu\text{m}^2$ collection diodes.

R&D for the demonstrator of the CBM-Micro-Vertex Detector (MVD) *

S. Amar-Youcef^{1,2}, N. Bialas¹, M. Deveaux¹, D. Doering¹, J. Heuser³, I. Fröhlich¹, J. Michel¹, C. Müntz¹, S. Seddiki^{1,4}, C. Schrader¹, J. Stroth¹, T. Tischler^{1,4}, and B. Wiedemann¹

¹IKF, University Frankfurt; ²Helmholtz Research School, Frankfurt; ³GSI, Darmstadt; ⁴IPHC, Strasbourg

In CBM, open charm mesons will be identified by reconstructing their secondary decay vertices. This requires a vertex detector with very good secondary vertex resolution ($\sigma_{SV} \sim 50 \mu\text{m}$ along the beam axis). To match this requirement, a highly granular pixel detector with excellent spatial resolution ($\sim 5 \mu\text{m}$) and minimum material budget (few 0.1% X_0) will be installed in the vacuum close to the target. A short readout time ($\sim 10 \mu\text{s}/\text{frame}$) and good radiation hardness (some MRad, $> 10^{13} \text{ n}_{\text{eq}}/\text{cm}^2$) are needed to handle the high collision rate ($10^5 - 10^6 \text{ Au+Au collisions/s}$) required for studying open charm.

To study the electrical and mechanical system integration the future CBM Micro Vertex Detector (MVD), the so-called demonstrator (see Fig.1) is set up in the IKF Technology Lab. The demonstrator is not designed to match the requirements of the MVD but to provide a development platform for the software and hardware solutions needed. It integrates two Mimosa-20 sensors (with each 640×320 pixels on $19.2 \times 9.6 \text{ mm}$ active surface) on a light, vacuum compatible, cooling support. The four serial output lines of the demonstrator provide each a 50 MHz analog signal. The corresponding 2.4 Gbit/s raw data stream is to be compressed by a real time cluster finding logic.

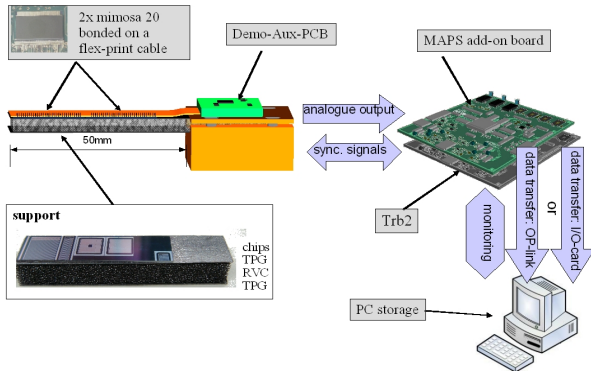


Figure 1: Sketch of MAPS Demonstrator

Mechanical concept

The cooling support of the demonstrator is formed from two layers of Thermal Pyrolytic Graphite (TPG), which surround a spacer made from the very light Reticulated Vitreous Carbon (RVC). The sensors, which are readout via a light flex print cable (FPC), are directly glued on the highly

* In co-operation with IPHC. Work supported by BMBF (06FY173I), GSI Darmstadt (F&E) and Helmholtz Research School Frankfurt



Figure 2: Add-on board and TRBv2 on back side.

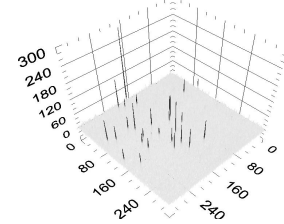


Figure 3: CDS-corrected frame of a Mimosa-20 matrix with several hits.

heat conductive TPG, which transports their heat towards a heat sink outside the MVD acceptance. The validity of this cooling concept was confirmed by finite element simulations. Within the last year, the cooling support and the FPCs were build and are being tested.

The readout of the demonstrator

The FPC, which has been designed by the electronic department of the IKF, integrates all electrical lines required to steer and readout both MIMOSA-20 sensors. It will be connected to the chip by wire bonding and to an intermediate readout board via a fine pitch connector. The intermediate board will buffer the signal of the sensors and send it to an ADC board (see Fig.2), which is an add-on board for the TRBv2 standard [1]. This board hosts four 12-bit ADCs to sample the analog signals of the two Mimosa20-chips, an FPGA (XC4VLX40) and 3 GB of SDRAM [2]. Those resources are sufficient to process the data of the sensors on-line with pipelined algorithms for correlated double sampling (CDS) and hit discrimination. The latter will reduce the data stream to be sent via the optical link (2 Gbit/s) of the TRBv2 to $\lesssim 200 \text{ Mbit/s}$. The ADC board has been build and tested with a preliminary firmware, which allows to write uncompressed data to a hard drive of a PC.

A dedicated ROOT-based offline analysis software allowed for extracting clusters from an ^{55}Fe source from this data (see Fig.3). It will also be used to support the ongoing development of the FPGA based data sparsification algorithms.

References

- [1] I. Froehlich et al., A General Purpose Trigger and Readout Board (TRB), IEEE Trans. Nucl. Sci., 2007.
- [2] C. Schrader et al., A Readout System for the CBM-MVD Demonstrator, GSI Report 2007.

Progress with layout studies of the CBM Silicon Tracking System

R. Karabowicz¹, A. Kotynia^{1,2}, and J. M. Heuser¹

¹GSI, Darmstadt, Germany; ²Warsaw University, Poland

Efficient charged particle tracking and high momentum resolution is one of the central performance requirements for the CBM Silicon Tracking System (STS). The aim of ongoing layout studies is to design a highly granular and low mass detector system that can track the 1000 charged particles that are typically generated in Au+Au collisions at 25 GeV/u projectile energy. A low mass detector is required to achieve a momentum resolution down to 1%. Progress has been made with implementing realistic detector response functions. The performance of the next prototype detectors to be manufactured have been studied.

Detector Layout

The current STS layout comprises eight detector stations fully based on micro-strip detectors. The stations have a ladder structure and are build of $300\mu\text{m}$ thick double-sided silicon micro-strip sensors with horizontal size of 6 cm and a strip pitch of $60\mu\text{m}$. The strip length was matched to a maximum occupancy of less than 5% and results in a vertical size of one sensor from 2 to 6 cm. Groups of sensors (sectors) are individually read out with the read-out electronics at the perimeter of the STS. Signals from the sectors are sent through thin capton micro-cables to the front-end boards. One of the changes in the current STS layout compared to the version presented in [1] is the orientation of the sensor strips. Previously, one side of the detector had its strips under a 15° stereo angle. The new layout describes strips rotated by a stereo angle of $\pm 7.5^\circ$ on the front and back planes. This is illustrated in Fig. 1.

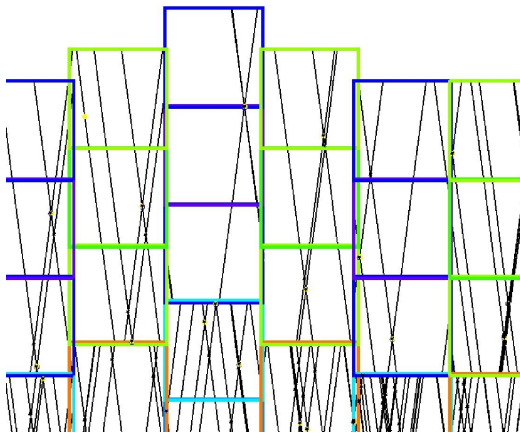


Figure 1: Event display showing active strips in a STS station. The angle between front and back strips is 15° .

Performance Studies

The performance of STS detector was evaluated. Realistic detector response functions were implemented that include signal sharing between strips and the formation of hit clusters. The cluster finding method is based on charge smearing due to particle diffusion in the electric field. The algorithm defines a cluster by finding nearby strips with a signal above a certain threshold. The left part of Fig. 2 shows a graphical illustration of the cluster finding method. The cluster position is calculated by means of a center-of-gravity algorithm. The right part of Fig. 2 shows the distribution of cluster sizes when reconstructing tracks from central collision at 25 GeV/u.

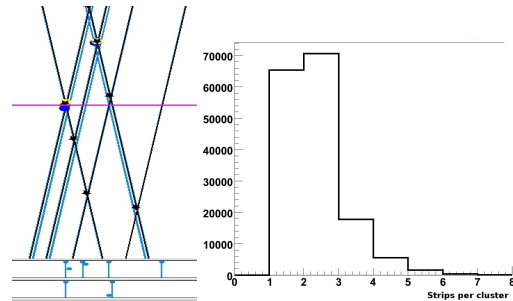


Figure 2: Left: Illustration of the cluster finding method. The bottom part of the figure shows the charge division sampled at the horizontal line in the middle of the picture. Right: Distribution of the number of fired strips per cluster.

When we apply the Cellular Automaton for track finding and the Kalman Filter for track fitting [2] as tuned for previous studies of ideal detector response, the tracking efficiency drops from 97% down to about 90%, for tracks with momenta exceeding 1 GeV/c.

Next steps

To recover the tracking efficiency, we will include the cluster finding method and further aspects of a realistic response model, e.g. channel dead time, into the reconstruction code. The correct determination of the errors of the hit positions is another topic being studied at the moment.

References

- [1] R. Karabowicz and J. M. Heuser, "Layout studies of the Silicon Tracking System for the CBM experiment", CBM Progress Report 2007 33
- [2] I. Kisel et al., "Fast SIMDized Kalman filter based track fit", CBM Progress Report 2007

Development of radiation hard silicon detectors for the CBM Silicon Tracking System using simulation approach

Sudeep Chatterji and Johann M. Heuser
 GSI Darmstadt

The very intense radiation environment of the planned Compressed Baryonic Matter (CBM) experiment at the international research center FAIR makes radiation hardness a very important issue for the Silicon Tracking System (STS). The STS will consist of eight stations of double sided strip detectors at a distance between 25 cm to 100 cm downstream of the target. It is expected that the total integrated fluence will reach $1 \times 10^{15} \text{ cm}^{-2}$ 1 MeV neutrons equivalent which is more than expected at LHC at CERN. The major macroscopic effect of radiation damage in determining the viability of long-term operation of silicon sensors is the change in the effective charge carrier concentration (N_{eff}), leading to type inversion. For the safe operation over full CBM life time, detectors are required to sustain very high voltage operation, well exceeding the bias voltage needed to fully deplete the heavily irradiated sensors. Thus, the main effort in the development of silicon sensors is concentrated on a design that avoids p-n junction breakdown at operational biases.

Simulations are carried out to study the effect of change in N_{eff} on the breakdown performance of the device using the device simulation package PISCES [1]. The simulation grid is shown in Fig. 1. Detailed calculations with the Hamburg Model [2] have allowed the parameterization of these effects to simulate the operation scenario of silicon detectors over full CBM life time. Also, the impact of various crucial geometrical parameters like device depth (W_N), width of back N^+ layer (W_N^+), strip width (W) and strip pitch (P) on the guard ring equipped structure after type-inversion has been studied in detail. It is clear from Fig. 2 that the peak electric field occurs at the junction curvature which is responsible for the premature breakdown of the device. Also process simulations have been performed using SUPREM-4 [3] for studying the annealing behaviour of Boron implanted in silicon. Fig. 3 shows the impact of annealing parameters on the electrical characteristics of the device.

We plan to procure 3-dimensional simulation packages from Synopsis [4] through EuroPractice Software Service of which GSI is a member so that we can accurately simulate double sided strip detectors.

References

- [1] <http://home.comcast.net/~john.faricelli/tcad.htm>
- [2] M. Moll et al., Nucl. Instr. Meth. A439 (2000) 282
- [3] <http://mems.mirc.gatech.edu/ece4752/suprem.html>
- [4] <http://www.te.rl.ac.uk/europractice/software/synopsys.html>

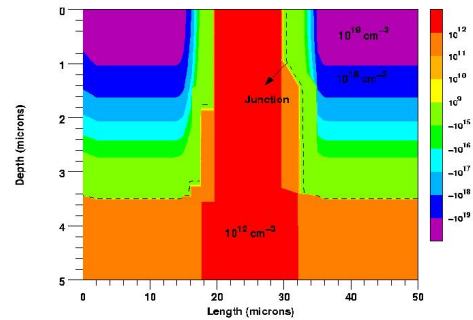


Figure 1: Cut through two neighbouring strips of a microstrip detector. Doping concentration profile in the PISCES simulation grid.

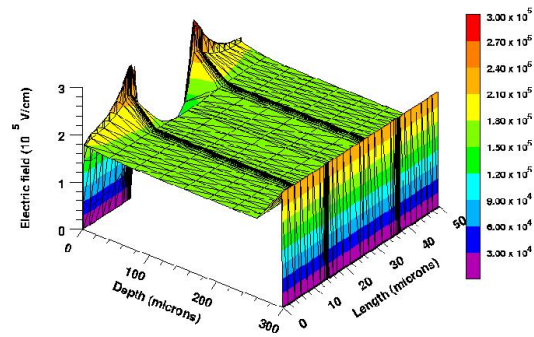


Figure 2: 3-D Electric field profile within the detector at breakdown.

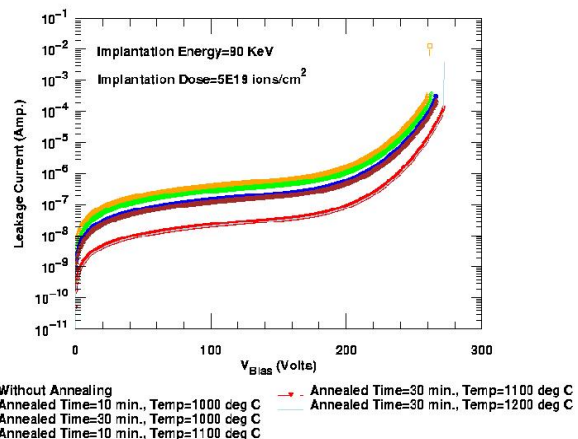


Figure 3: Impact of annealing time and temperature on the electrical characteristics of the device.

Development of microstrip detectors for the CBM Silicon Tracking System

J.M. Heuser¹, C.J. Schmidt¹, A. Lymanets², R. Röder³, and L. Long³

¹GSI, Darmstadt, Germany; ²FIAS, University of Frankfurt, Germany; ³CIS, Erfurt, Germany

The first prototypes of double-sided microstrip detectors for the CBM Silicon Tracking System, designed and produced in 2007 in cooperation of GSI and CIS [1], have meanwhile been applied to in-beam experiments of CBM prototype detector systems. These *CBM01* [2] sensors were primarily designed for investigations of a detector topology compatible with the proposed construction of particularly low-mass tracking stations.

New detector developments in 2008 addressed the exploration of radiation tolerant design features. With support from BMWI [3], a new wafer *CBM02* has been designed at CIS carrying 2 pixel detectors, 18 strip detectors and various test structures including *pin* diodes. The layout of the 4" wafer is shown in Fig. 1. The largest structures are double-sided orthogonal microstrip detectors with 256 AC-coupled strips of 50 and 80 μm pitch per side. Every detector is different and includes either structures for punch-through biasing, poly-silicon biasing, or a combination of both. On the n-side, the strip insulation was realized in p-stop, p-spray and field plate technology. Various guard ring structures have been implemented. A batch of 18 wafers was produced on 285 μm thick n-type float-zone material, every wafer with a different p doping concentration. The detectors, shown in Fig. 2 after wafer dicing, are being characterized in the laboratory. A bias voltage scan for a 50 μm pitch strip detector is shown in Fig 3. A reference tracking telescope under construction for the CBM beam test runs at GSI will utilize these detectors. First irradiation experiments with *pin* diodes as shown in the photo have been performed very recently in neutron beams. Their evaluation is ongoing and are supposed to yield information on the effectiveness of the different designs towards radiation tolerance.

We plan to design a next full-size double-sided CBM detector prototype with poly-silicon biasing and a ± 7.5 degree stereo angle of the strips w.r.t. the detector edge. The new layout has several advantages for the engineering of module components. The detector, to be produced in several sizes, i.e. strip lengths, will feature a double-metal interconnection layer on both stereo sides.

References

- [1] CIS Research Institute for Micro Sensors and Photovoltaics GmbH, Erfurt, Germany, <http://www.cismst.de>
- [2] J.M. Heuser et al., GSI Report 2008-1 9
- [3] German Federal Ministry of Economics and Technology (BMW), project INNOWAT SPID

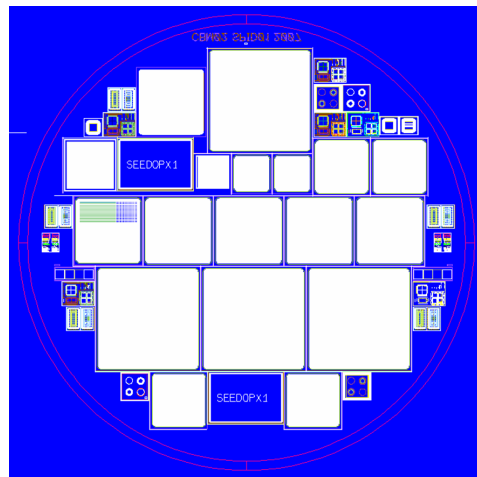


Figure 1: Layout of the CBM02 wafer with various double-sided microstrip test detectors and other test structures.

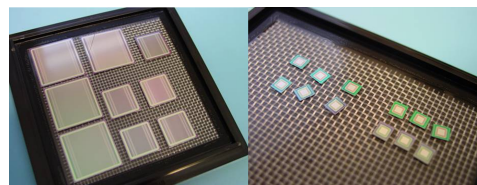


Figure 2: CBM02 test detectors and pin diodes.

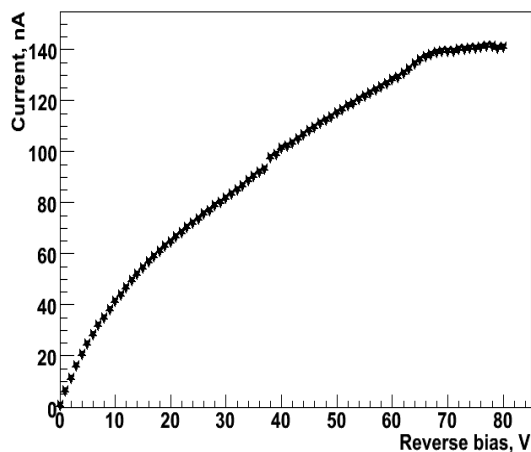


Figure 3: Operation of a CBM02 test detector with poly-silicon biasing structure. Full depletion is reached at about 70 V reverse bias.

First test of a prototype CBM silicon detector system in a proton beam at GSI

J.M. Heuser¹, W. Niebur¹, R. Karabowicz¹, W. Müller¹, V. Friese¹, C.J. Schmidt¹, R. Lalik²,
A. Lymanets³, Y. Murin⁴, P. Nomokonov⁴, and the CBM Collaboration

¹GSI Darmstadt; ²AGH Krakow; ³FIAS University of Frankfurt; ⁴JINR Dubna

In September 2008, the CBM collaboration performed the first essential test of two prototype detector systems in a 2.5 GeV proton beam at GSI. The experiment at the HTD beam line in Cave C comprised prototype micro-strip detectors of the Silicon Tracking System, and gas-electron-multiplier (GEM) detectors. The detectors were coupled to a self-triggering front-end electronics and data acquisition system. This novel data read-out and acquisition concept is being developed for nuclear interaction rates of up to 10 millions per second. It aims at enabling the online reconstruction of collision events with up to 1000 produced particles. In a further measurement the radiation tolerance of Field Programmable Gate Arrays (FPGAs) was investigated.

The silicon detector setup is shown in Fig. 1. It comprised two detector boards equipped with prototype microstrip sensors *CBM01* developed by the GSI-CBM group and CIS Erfurt [1], and two readout boards developed at GSI around the *n-XYTER* [2] chip, developed in a different project. The readout chain included further *Syscore* controller boards [3] for communicating with the *n-XYTER* electronics, and the GSI data acquisition system *DABC* [4].

The commissioning of the silicon detector system was performed with a radioactive source. The ADC spectra of several readout channels are shown in Fig. 2. Response to the proton beam is shown in Fig. 3. The correlation of fired horizontal and vertical strips from the up-stream and the down-stream detector is clearly visible, only linked through the time measurement done by the front-end electronics.

The test demonstrated the validity of the CBM data acquisition concept based on detector systems read out with self-triggering front-end electronics. Three different detector partitions were commonly read out. The full data chain was successfully realized, from the detectors' front end to data in the acquisition system's raw format and FairRoot format, allowing for on-line monitoring during the experiment and subsequent detailed off-line analysis. For the characterization of forthcoming prototype components of the CBM Silicon Tracking System, a reference tracking telescope is under preparation.

References

- [1] J.M. Heuser et al., GSI Report 2008-1 9
- [2] A.S. Brogna et al., Nucl. Instr. Meth. Phys. Res. A568 (2006) 301-308
- [3] W.F.J. Müller, GSI DOC-2007-Apr-100
- [4] <http://dabc.gsi.de>



Figure 1: Test system with two CBM01 silicon microstrip detectors and n-XYTER readout boards.

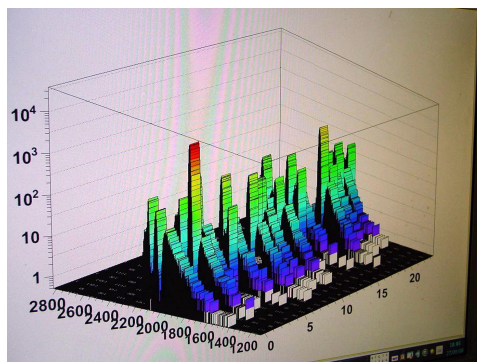


Figure 2: Commissioning of the test system: ADC spectra from a ^{90}Sr β^- source in several readout channels.

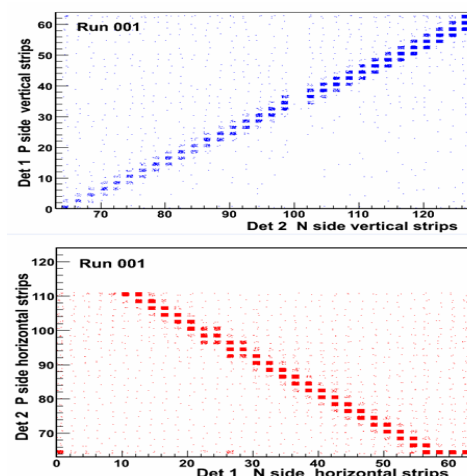


Figure 3: Correlation of fired strips in two silicon microstrip detectors.

Design and assembly of STS demonstrator module 0-B

V.M. Borshchov¹, J.M. Heuser², Yu. A. Murin³, M.V. Zamirets¹, O.M. Listratenko¹,
M.A. Protsenko¹, I.T. Tymchuk¹, and the CBM-MPD STS Consortium

¹State Enterprise Scientific Research Technological Institute of Instrumental Engineering (SE SRTIIE), Kharkov, Ukraine; ²GSI, Darmstadt, Germany; ³Joint Institute for Nuclear Research (JINR), Dubna, Russia

A first demonstrator module for the micro-strip detector prototype CBM01B2 was developed by the CBM-MPD STS Consortium participants and manufactured with usage of aluminium-polyimide commutation elements and innovative “chip-on-flex” assembly technology in SE SRTIIE, Kharkov, Ukraine. As a result of the activity, one technological and two working demonstrators were produced.

Design of the demonstrator

The demonstrator is shown in Fig. 1 and consists of:

1. Baby sensor CBM01B2 - 1 pc.;
2. Rigid board - 1 pc.;
3. Flexible board - 1 pc. Material: foiled dielectric FDI-A-50 (thickness of aluminium layer is 30 μm , thickness of polyimide layer is 20 μm). Configuration in bonding areas:
 - for ERNI-flex-mounts: traces pitch is 635 μm , pads width is 500 μm ;
 - for Sensor cables: traces pitch is 300 μm , pads width is 200 μm ;
4. Flexible sensor cables - 4 pcs. Material: foiled dielectric FDI-A-24 (thickness of aluminium layer is 14 μm , thickness of polyimide layer is 10 μm). Configuration in bonding areas:
 - traces to flex board: pitch 300 μm , width 80 μm ;
 - traces to Sensor: pitch 101,4 μm , width 34 μm .

The Sensor cables design ensures 100% automatically test (shorts, traces breaks) before assembly with applying of a standard contact device (on the basis of Socket IC51-4364) for testing;
5. ERNI 114805 connectors on flex-mounts - 8 pcs.;
6. LEMO connectors (bias lines) - 4 pcs.;
7. 1 MOhm SMD resistors on flex-mounts - 4 pcs.

Assembly of the demonstrator

The assembly has been executed in three stages:

1. Ultra-sonic bonding of cables to sensor (see Fig. 2).
 - US bonding of flex cables to sensor (n-side): (128 traces + 2 bias lines) \times 2 = 260 bonds;
 - bonds protection (glue EpoTec T7110);
 - US bonding of flex cables to sensor (p-side): (128 traces + 2 bias lines) \times 2 = 260 bonds;
 - bonds protection (glue EpoTec T7110).
2. Assembly of flexible-rigid board.
 - gluing of “balconies” to rigid board (glue Araldite 2011);

- gluing of flexible board to rigid board (glue UP10-14-2);
- mounting of SMD on flex-mounts to flexible-rigid board. US bonding: $6 \times 4 = 24$ bonds, and bond protection (glue EpoTec T7110);
- mounting of ERNI connectors on flex-mounts to flexible-rigid board. Gluing, US bonding: $64 \times 8 = 512$ bonds, soldering and bond protection (glue EpoTec T7110).

3. Mounting of sensor assembly to board.

- soldering LEMO connectors to flex-rigid board;
- mounting of sensor assembly to flex-rigid board. Gluing (glue Araldite 2011), US bonding: $130 \times 4 = 520$ bonds and bond protection (glue EpoTec T7110).

We hope that the experience acquired by us with the development of a design, improvement of assembly and manufacturing technology on the basis of flexible-rigid boards will be useful for CBM-MPD STS Consortium in the future for next investigations of sensors and prototype modules.

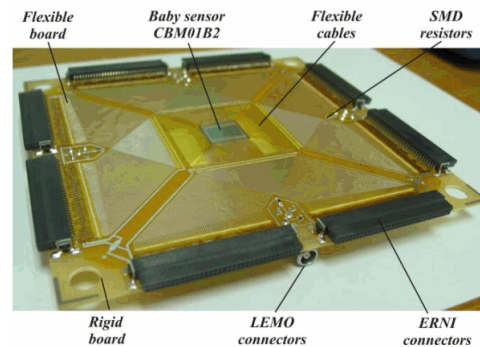


Figure 1: Assembled STS demonstrator module “0-B”.

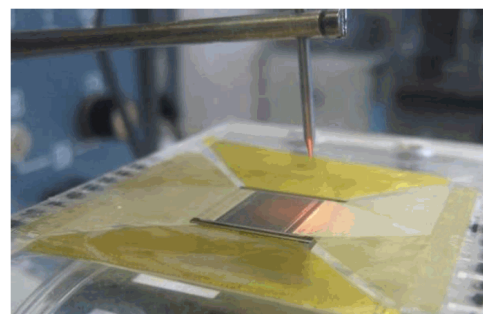


Figure 2: Ultra-sonic tab bonding of cables to the sensor. A single demonstrator comprises a total of 1600 bonds.

Test of STS demonstrator module 0-B in a 50 GeV proton beam

Yu. Murin¹, I. Ruffanov¹, A. Vorobiev², Yu. Tsyupa², D. Karmanov³, A. Leflat³, V. Volkov³,
A. Voronin³, J.M. Heuser⁴, A. Lymanets⁵, and the CBM-MPD STS Consortium

¹Joint Institute for Nuclear Research (JINR), Dubna, Russia; ²Institute of High Energy Physics (IHEP), Protvino, Russia; ³Skobeltsyn Institute of Nuclear Physics of Moscow State University (SINP MSU), Moscow, Russia; ⁴GSI Helmholtz Centre for Heavy Ion Research GmbH, Darmstadt, Germany; ⁵Frankfurt Institute for Advanced Studies (FIAS), University of Frankfurt, Germany

The CBM-MPD STS Consortium [1], established by GSI and JINR, focuses on the technical realization of an ultra-light silicon tracking detector system for the CBM experiment at FAIR and the MPD experiment at NICA. The STS demonstrator module 0-B [2] was the first to be used in the planned feasibility studies of technologies relevant to the CBM STS R&D program. The purpose of this study was a quality check of the double-sided microstrip detector prototypes *CBM01B2* attached to and read out through ultra-thin aluminum cables, a technology anticipated for wide usage within the CBM Silicon Tracking System. Two samples of the demonstrators were manufactured at SE SRTIIE, Kharkov, Ukraine, and tested electrically for short circuits and brakes of strips using probe stations at SINP MSU, Moscow. One of the demonstrators was assembled later into the test tracking station shown in Fig. 1 and characterized in the SVD-2 [3] experiment at IHEP, Protvino, Russia, as described below.



Figure 1: Tracking station with STS demonstrator 0-B (centre) and readout electronics (boards on the perimeter).

Experimental set-up

The demonstrator station S_T was placed in the beam tracker of the SVD-2 experiment that studied collisions of a 50 GeV proton beam with a liquid hydrogen target. A schematic view of the test set-up is shown in Fig. 2. The beam tracker is shown in Fig. 3. The SVD-2 experiment is tuned to trigger on events with multiplicity of secondaries

> 8 and the interaction point defined by the vertex locator telescope S3-S6 built from 50 μm pitch silicon microstrip detectors. The vertex coordinates together with the coordinates of the tracks estimated from the high precision 25 μm pitch beam-track stations S1 and S2 made possible position monitoring of the 50 GeV protons on the surface of the demonstrator with an accuracy of around 6 μm . Every particle spill delivered $\approx 10^6$ protons in 1.5 s with 10 s gap between the spills.

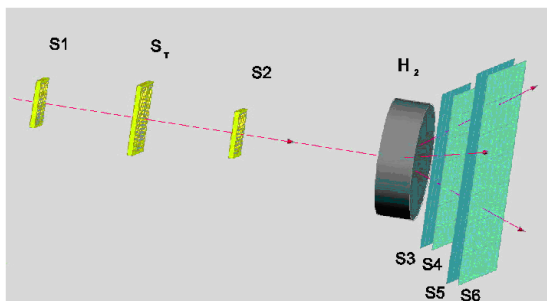


Figure 2: Beam tracker S1-S2 and vertex detector S3-S6 of the SVD-2 experiment. The test station S_T was positioned at about 1 m upstream of the H_2 target.

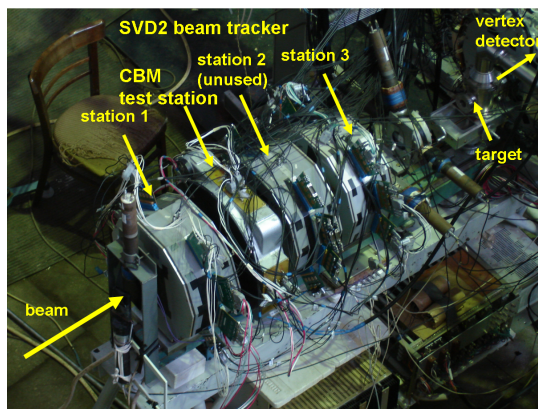


Figure 3: CBM01 test tracking station integrated in the beam tracker of the SVD-2 experiment.

Results from the off-line analysis

The goal of the experiment was to estimate the spatial resolution and the efficiency of the demonstrator. For this the initial pedestals and noise were calculated from the first 1000 of events of each pedestal calibration run. The recorded values of pedestals were subtracted from the ADC values giving signals S_i proportional to the charge collected by the i -th strip. The typical S_i/N_i value for MIP protons was about 8, where N_i is the noise RMS of the i -th strip. This depicted the moderate quality of the applied front-end electronics based on the GASSIPLEX v1.5 chips. The thresholds were adjusted such that only strips with $S_i/N_i > 3$ were qualified as fired strips. The contiguously fired strips were defined as “clusters”. For the analysis of the residuals distributions depicted in Fig. 4, a sample of 10 000 tracks was used.

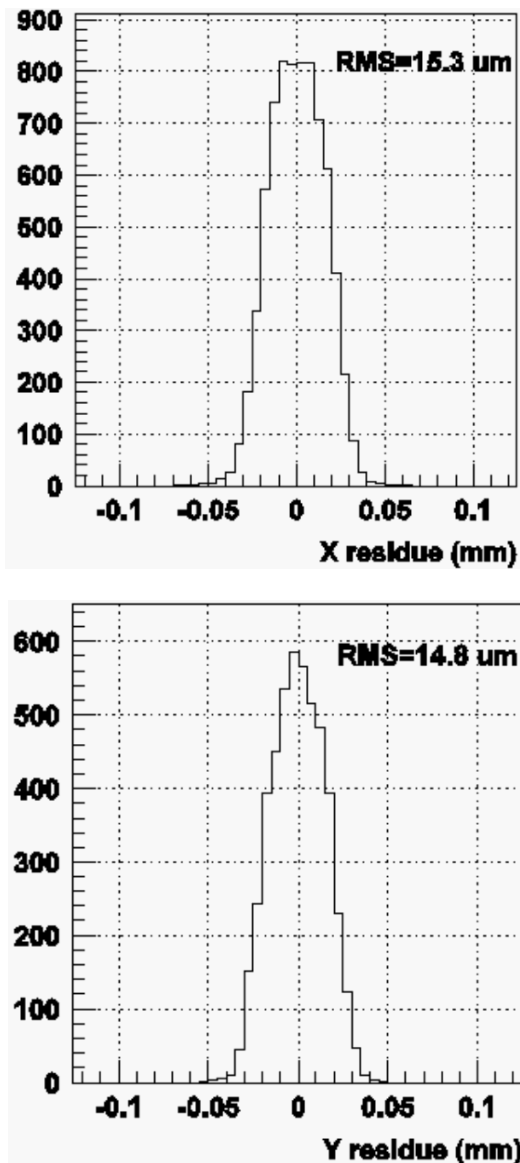


Figure 4: Track residuals measured with the demonstrator.

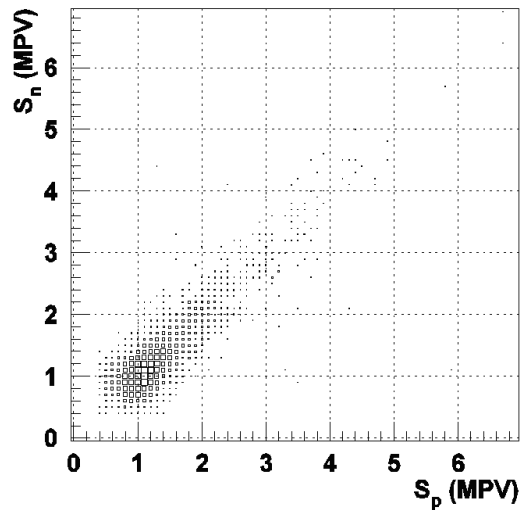


Figure 5: Correlation of cluster charge from both signal planes of the demonstrator.

The size of the clusters generated during the passage of a proton track through the demonstrator were distributed as follows: 87% one-strip, 12% two-strip, and 1% three and more strip clusters. The detection efficiency for protons was close to 100%. The position correlation between the cluster charges measured with the P- and N-sides of the silicon detector is shown in Fig. 5. The cluster charge distributions measured from each side of the tested sensor are well described with a Landau function folded with a Gaussian function with $\sigma \approx 0.2$ in units of the Most Probable Values of energy loss (MPV).

Conclusions

The high quality of the TAB-bonded ultra-thin aluminum microcables produced by SE SRTIIE, Kharkov, was experimentally confirmed. It was also demonstrated that even with moderate signal-to-noise ratios achieved in the system the resulting spatial resolution turns out to be still compatible with the CBM STS requirements provided each channel of the 50 μm strip detector is read-out. The correlation of the signal amplitudes from different sides of the double-sided sensor is evident and must be used as a pre-tracking filter for ruling out false hit combinations inevitably appearing in high multiplicity reactions to be studied with the CBM experiment.

References

- [1] http://sunse.jinr.ru/projects/sts/abstract_sts.html
- [2] see contribution V. Borshchov et al., this report
- [3] <http://www-svd.sinp.msu.ru>

Characterization of CBM01 sensors for the Silicon Tracking System

V. Pugatch¹, J. Heuser², V. Kyva¹, A. Lymanets^{1,3}, A. Melnyk¹, V. Militsiya¹, and O. Okhrimenko¹
¹KINR, Kiev; ²GSI, Darmstadt; ³now at FIAS, J. W. Goethe University, Frankfurt

First prototype detector modules for the Silicon Tracking System have been assembled at KINR comprising double-sided microstrip sensors of type *CBM01*, mounted onto carbon fiber supporting frames and connected with microcables to a discrete readout electronics. Their performance was characterized in a dedicated laboratory test setup, including the determination of the full depletion voltage, the leakage current, and the charge sharing of adjacent strips. The observations are summarized below.

Current-voltage curves for the test sensors *CBM01-B1* and *CBM01-B2* showed saturation of the leakage currents (1-2 μA) at $\sim 60\text{ V}$ and a breakdown voltage of $\sim 120\text{ V}$. There was no such saturation for the large *CBM01* sensor (leakage current $\sim 10\ \mu\text{A}$ at 60 V). The charge collection of the strips was investigated with radioactive sources (^{226}Ra - α , ^{90}Sr - β) as well as with a laser beam (640 nm, diameter $10\ \mu\text{m}$) movable in X and Y-directions. The measurements revealed an unexpected behaviour of the interstrip gap response at low (up to 40 V) voltages for all three types of sensors. The numbers near the dots in Fig. 1 indicate the coordinate of the laser spot (in μm) in the interstrip gap for two depletion voltages (0 and 40 V). One might see that a perfect linear dependence of two signals exists for the $25\ \mu\text{m}$ long region at 0 V that is reduced to a few μm at 40 V bias.

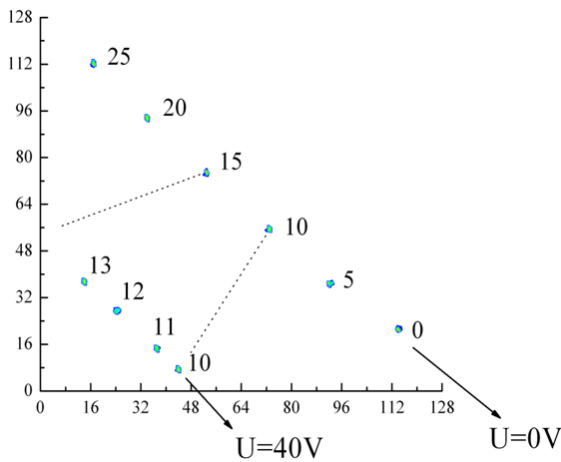


Figure 1: Irradiation with a laser beam from the p-side: ADC value of p-strip i vs ADC value of p-strip $i+1$.

Similar results were observed with an α -source (Fig. 2). After having reached full depletion at $\sim 40\text{ V}$ the signals were increasing (as one would expect), yet the energy resolution was worse than with the non-depleted sensor.

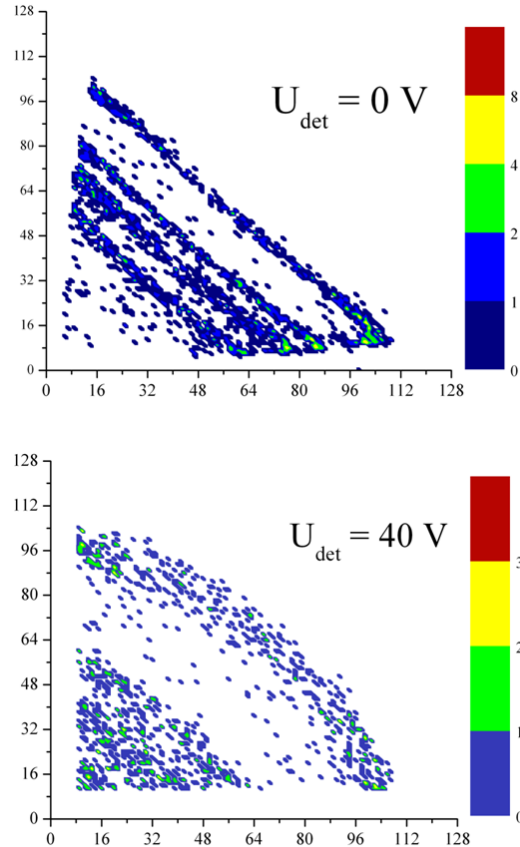


Figure 2: Irradiation with an α -source from the p-side: Coincident energy spectra (in arbitrary ADC units) for pairs of adjacent p-strips (one vs the other).

The decrease of the signal-to-noise ratio with increasing reverse bias has been observed also in measurements simulating *MIPs* with a ^{90}Sr β -source. The spectra exhibited a Landau shape at low voltages acquiring a Gaussian shape at high depletion voltage. The saturation of the *MIP* peak was observed at 40 V for the *CBM01-B2* sensor, while for the *CBM01* sensor it was in the range of 70 V . Another method has been applied to determine the full depletion voltage for the *CBM01* sensor: Measuring the response of the n-strips as a function of the depletion voltage for laser irradiation of the sensor's n-side. The full depletion voltage derived by this method was about 80 V .

For the design of forthcoming prototype detectors, particular attention should be paid on the charge collection performance from the interstrip regions.

Laser stand for testing STS silicon microstrip detector modules

V. Pugatch¹, M. Borysova¹, A. Chaus¹, J. Heuser², O. Kovalchuk¹, V. Kyva¹, A. Lymanets^{1,3},
V. Militsiya¹, O. Okhrimenko¹, and D. Storozhyk¹

¹KINR, Kiev; ²GSI, Darmstadt; ³now at FIAS, J. W. Goethe University, Frankfurt

Laser Stand - a Part of the Quality Assurance System

In the framework of the Collaboration Agreement between GSI and KINR a Laser Stand (LS) for testing STS *Si* microstrip detector modules has been designed and built at KINR. It is aimed to become a part of the quality assurance system for real detector modules to be built soon. In general, quality assurance system has to verify mechanical precision, electrical connections, cooling flow, temperature profiles ect. At the laser stand one should be able to qualify detector module channels by measuring common mode fluctuations, signal over noise performance, full depletion voltage, leakage currents as well as the long term stability of those characteristics. As an outcome, a map of operating channels of the CBM tracker should be produced, finally. Main characteristics of the laser stand (Fig. 1) built at KINR are as follows: laser beam wavelength 640 nm, diameter of the laser beam spot $\sim 10 \mu\text{m}$ (at 4 mm distance between the laser and silicon wafer), step motor travel range in X and Y $15 \times 15 \text{ cm}^2$, position resolution $10 \mu\text{m}$.



Figure 1: Laser stand inside an r/f and light shielded box.

To produce by a laser a charge in a silicon sensor equivalent to a MIP one has to apply 2 V negative pulse with $\sim 20 \text{ ns}$ width to the laser diode. The results discussed below were obtained at the LS test setup at KINR currently based on discrete readout electronics used for the CBM01 prototype sensors characterization. The pre-Prototype Detector Module components (supporting frames, sensors, microcables, cooling) and their connections were tested. Step-motors are of the ДШИИ-200-2 type (12-35 V) driven

via LPT-port by a software designed to support all operations needed for quality assurance procedures.

Fig. 2 illustrates a response of two adjacent strips of the CBM01 prototype sensor when a laser spot was moved from one strip to another ($50.7 \mu\text{m}$ pitch). The middle picture (equal amplitudes) corresponds to the laser spot fixed exactly in between strips.

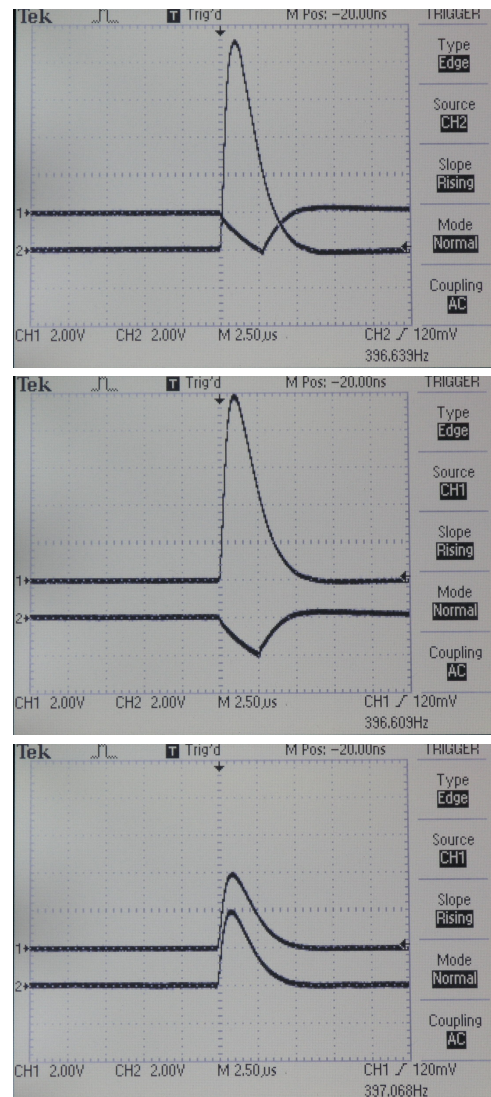


Figure 2: Laser spot moving between adjacent strips.

Supporting frame and microcable properties for the STS microstrip detector module prototype

V. Pugatch¹, M. Borysova¹, A. Chaus¹, J. Heuser², O. Kovalchuk¹, V. Kyva¹, A. Lymanets^{1,3}, V. Militsiya¹, O. Okhrimenko¹, D. Storozhyk¹, V. Zhora⁴, and A. Galinskiy⁵

¹KINR, Kiev; ²GSI, Darmstadt; ³now at FIAS, J. W. Goethe University, Frankfurt; ⁴Institute of Microdevices, Kiev; ⁵SPA AEROPLAST, Kiev

Supporting frames

Low mass support frames for the CBM01 prototype sensors have been designed and produced by AEROPLAST (Kiev). Construction material is carbon fiber with a material budget below 0.3% X_0 (see [1] for further details). Three-layer frames were used to house three types of prototype silicon sensors (Fig. 1).

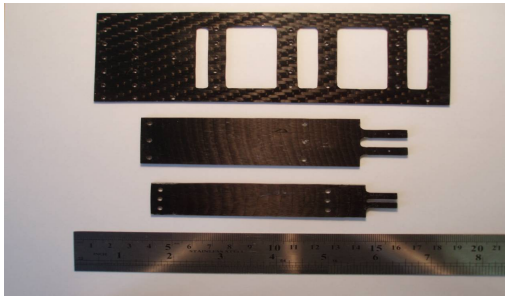


Figure 1: Supporting frames for the CBM01 prototype sensors.

Detailed studies of their mechanical and thermal conductivity properties were undertaken using a test setup with a cooling system built at KINR, also with the goal to compare the new material with a commercially available one. Cold water (4 °C) was circulated through a ZALMAN (www.zalman.co.kr) processor cooler with the frames attached to it by conductive silver glue (Fig. 2). PT100 temperature sensors were used to monitor the temperature. An example of the measured temperature evolution at a dummy silicon sensor (CBM01-B2 type) glued by silicon glue onto the supporting frame (fork shape at the sensor region) is shown in Fig. 3.

On average the temperature at the silicon sensor was stable after half an hour reaching level of 12 °C. For comparison, a commercial sample of the supporting frame gave a bit better result with ~20 minutes needed for the temperature stabilization at the level of 10 °C.

Microcables

The technology of microcable production developed at the Institute of Microdevices (IMD, Kiev) [2] has been modified to meet requirements of the STS prototype module. Low mass double-layer micro cables with 30 μm wide, 14 μm thick Al strips of $(2 \times 50.7) \mu\text{m}$ pitch

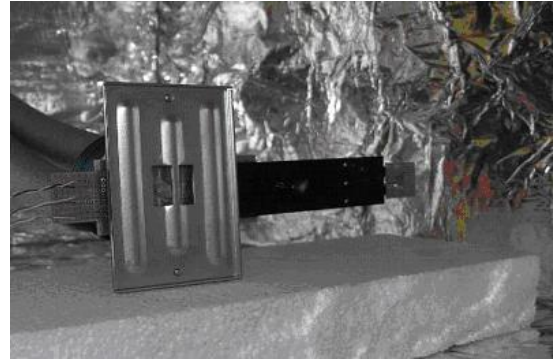


Figure 2: CBM01-B2 type sensor mounted on a corresponding frame for cooling studies.

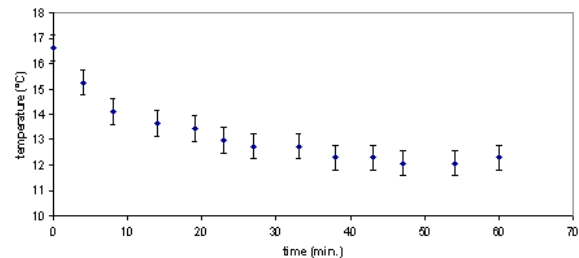


Figure 3: Temperature evolution at the silicon sensor.

on a 24 μm thick polyimide film have been produced to connect three types of CBM01 sensors to discrete read-out electronics [3]. The tests performed have shown that a reliable mono-metal (Al-Al) electric and mechanical connection (~ 10 g for break) between sensor and microcable pads was provided by ultra-sonic bonding. Test measurements of different CBM01 prototype sensors characterized by laser beam as well as radioactive sources are presented elsewhere in this volume.

References

- [1] M. Borysova et al., CBM Progress Report 2007, p 36
- [2] A. G. Sherevenya, I. A. Tuchinski, V. D. Jora. Patent 1781733 (USSR). BI, No.46, 1992
- [3] M. S. Borysova, J. M. Heuser, V. O. Kyva, A. O. Lymanets, V. M. Mylitsiya, O. S. Okhrimenko, V. M. Pugatch. Nuclear Physics and Atomic Energy, No. 3 (25), Kiev, 2008, p. 94-99.

Radiation hardness tests of silicon microstrip detectors with the KRI cyclotron

V. Jakovlev¹, S. Lashaev¹, L. Lebedev¹, L. Solin¹, D. Karmanov², M. Korolev², Yu. Murin³, J.M. Heuser⁴, and the CBM-MPD STS Consortium

¹V.G. Khlopin Radium Institute (KRI), St. Petersburg, Russia; ²Skobeltsyn Institute of Nuclear Physics of Moscow State University (SINP MSU), Moscow, Russia; ³Joint Institute for Nuclear Research (JINR), Dubna, Russia; ⁴GSI Helmholtz Centre for Heavy Ion Research GmbH, Darmstadt, Germany

At the MGC-20 cyclotron of KRI St. Petersburg, shown in Fig. 1, a neutron irradiation station has been set up for radiation hardness tests of silicon microstrip detectors (SD) under development for the CBM Silicon Tracking System.

Design and tests of neutron irradiation station

A feasibility study of conducting irradiation tests with neutrons from $^9\text{Be}(p,n)$ and $\text{D}(d,n)$ reactions was carried out with two types of irradiation systems presented in Fig. 2a and 2b, respectively.

The neutron spectra expected for the systems as prescribed by calculations [1] are presented in Fig. 3. Experimentally, the spectra and the space distribution of generated and background neutrons were studied with a neutron-activation technique based on 20 reactions with known neutron reaction cross sections. The monitoring of the neutron flux was carried out with $^{27}\text{Al}(n,p)^{27}\text{Mg}$, $^{27}\text{Al}(n,\alpha)^{24}\text{Na}$, $^{47}\text{Ti}(n,p)^{47}\text{Sc}$ and $^{48}\text{Ti}(n,p)^{48}\text{Sc}$ reactions with errors of the neutron fluence estimated as $\pm 20\%$.

The radiation hardness tests of 40 test pad diodes with a known response to neutron radiation was carried out to confirm the expected change of leakage current and depletion voltage of the sensors under test as a function of neutron dose. Irradiated samples were then tested at a dedicated probe station linked to PC which was developed and installed at the Cyclotron Laboratory of KRI to perform similar tests of the sensors produced for the CBM STS. The tests conducted showed for the $\text{Be}(p,n)$ reaction a considerable excess of radiation damage over to the expected values and the $\text{D}(d,n)$ results. Additional studies of this inconsistency revealed the presence of a large number of neutrons from $\text{Be}(p,n)$ reaction within the energy range of 1 - 6 MeV not accounted in the standard nuclear data bases and, as result, in our dose calculations for this reaction. The neutron spectra from the $\text{D}(d,n)$ is free of such admixtures and is consistent with our dose calculations. Still, to reserve the more intensive $\text{Be}(p,n)$ neutron source it was decided to define experimentally the effective ratio of Be -neutron and D -neutron spectra in a comparative study which is currently under way.

Conclusions

The development of the neutron source carried out in 2008 is close to its accomplishment, the routine testing of radiation hardness of SDs for the CBM STS. These are to start in the second quarter of 2009. The described R&D

effort was undertaken within the work plan of the ISTC [2] Project # 3540.

References

- [1] A.A. Filatenkov, S.V. Chuvaev, V.N. Aksenov, V.A. Jakovlev, *Systematic measurement of activation cross sections at neutron energies from 13.4 - 14.9 MeV*, INDC(CCP)-402, Distrib.: G, January 1997, Int. Nucl. Data Committee, IAEA, Vienna, Austria, 44 p.
- [2] www.istc.ru



Figure 1: The KRI cyclotron MGC-20.

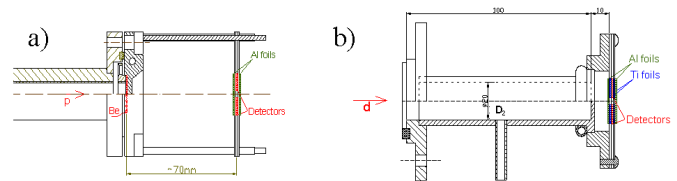


Figure 2: Beryllium (a) and D_2 -gas (b) target systems.

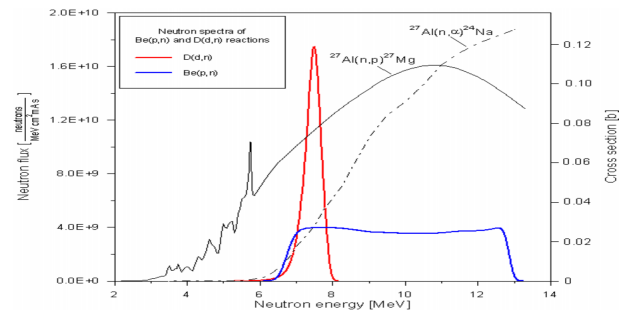


Figure 3: Neutron spectra for the Be -disk (blue line) and D_2 -gas (red line) target systems.

Ultra light-weight carbon-fiber structures for the CBM Silicon Tracking System

S. N. Igolkin¹, Yu. A. Murin², G.A. Feofilov¹, J.M. Heuser³, and the CBM-MPD STS Consortium

¹V.G. Khlopin Radium Institute (KRI), St. Petersburg, Russia; ²Joint Institute for Nuclear Research (JINR), Dubna, Russia; ³GSI Helmholtz Centre for Heavy Ion Research GmbH, Darmstadt, Germany

The Silicon Tracking System (STS) of the CBM project consists of 8 layers of silicon microstrip detectors. The detectors of each layer are combined in modules, connected to cooling channels and by cables to electronic units. To meet the requirements of the experiment, the mechanical support of the detectors should provide high precision of positioning of the detectors within the STS volume ($\approx 40 \mu\text{m}$ along the x-axis), long-term stability of position, and be accessible for maintenance and replacement of the detector modules. The experience we gained in the development of supporting-cooling structures for ALICE [1] suggests using in CBM STS high modulus (310 GPa for M55 composite) 3D three-edge 14g/m spaceframes (“ladders”) of carbon fiber shown in Fig. 1.

The carbon fiber frames are manufactured by a method we patented in 2008 [2]. The carbon fiber composite is suggested too for manufacturing other components of supporting structures such as L-shaped detector lockers (Fig. 2a) and long straw-thin plates used in assembling detector modules (Fig. 2b). The components were manufactured with the use of temporary technological equipment. Dedicated equipment will be designed and manufactured for small batch production of these components.

The main supporting frame for housing detector ladders shown in Fig. 3 is also suggested to be made of carbon fiber shapes commercially produced, specifically, of carbon fiber tubes. The precision positioning of detector frames is ensured by the precision U-shaped linear bearings with discrete supports and centering pins.

Conclusions

Using carbon-fiber for the supporting space frames of the STS brings the thermal displacement of detector modules to a minimum for temperature variations from ambient to working, i.e. within 45°C . The rigidity of carbon-fiber space frame complies with the mechanical constraints imposed by the requirements of the experiment. Large radiation length (25 cm) of the composite and low material budget (25 mg/cm^2 in the active area) result in minimal multiple scattering, which improves the accuracy of track reconstruction. The described R&D effort was undertaken within the work plan of the ISTC [3] Project # 3540.

References

- [1] G.A. Feofilov et al., *Inner Tracking System for ALICE: Conceptual Design of Mechanics, Cooling and Alignment*, CERN 94-07, pp.73-81
- [2] S.N. Igolkin et al., *An apparatus for production of intricate shape carbon-fiber articles*, Patent No. 79268 of 27.12.2008, Int. Cl. B29C53/56(206.01)
- [3] www.istc.ru

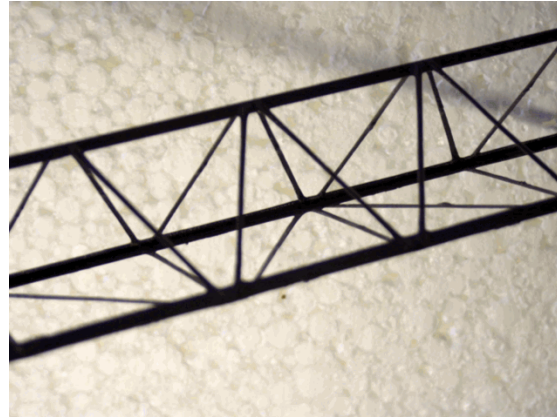


Figure 1: Carbon-fiber ladder support.



Figure 2: (a) L-shaped detector lockers. (b) Three-detector assembly with straw-thin silicon plates on a 2D support.

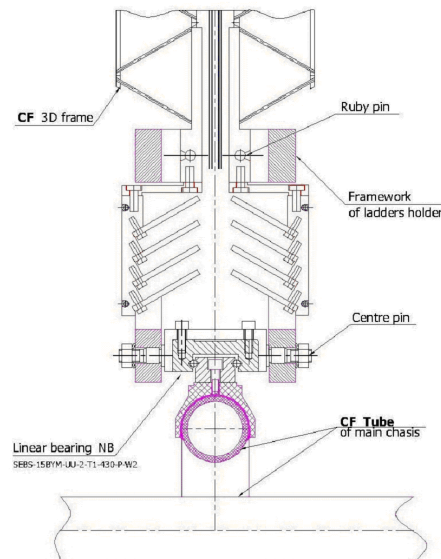


Figure 3: Detailed view of the STS detector assembly based on carbon fiber (CF) components.

Layout study of the RICH detector in the CBM experiment

S. Lebedev^{*1,2}, E. Belolaptikova³, and C. Höhne¹

¹GSI, Darmstadt, Germany; ²JINR LIT, Dubna, Russia; ³MIREA, Moscow, Russia

Progress of the CBM RICH layout was achieved in two important points. Simulation studies showed that standard glass mirrors do not deteriorate the global tracking efficiency. Second, a largely improved layout of a RICH strongly reduced in size was prepared. This layout will now be subject of further feasibility studies.

The influence of the RICH material budget to the STS, TRD and global (STS+TRD) track reconstruction performances was studied. Detailed simulations have been performed in order to obtain limitations for the material budget of the RICH mirrors. Three RICH geometries with different thicknesses of the mirrors (3 mm, 6 mm, and 10 mm) were simulated. The mirror support structure was implemented in form of a grid of aluminum tubes with a radius of 1.5 cm, wall thickness of 2 mm, and 40 cm distance between two tubes. Such a relation between radius and thickness of the tube wall is a standard for industry and can support the foreseen glass mirrors of about 40x40 cm² size.

Central UrQMD Au+Au collisions at 25 AGeV beam energy were used for the simulation. 25 primary e^+ and 25 primary e^- were embedded in each event in order to enhance statistics for electrons. The L1 STS track reconstruction algorithm was applied [1]. Two different methods were used for TRD track reconstruction: L1 [1] and LIT [2]. The observed changes in tracking efficiency do not exceed a few percent (see fig. 1). No major changes concerning ghosts and mismatches with STS tracks were found as well. These findings support the concept of a "standard" RICH mirror of 6 mm glass thickness and aluminum support, which will save money and efforts.

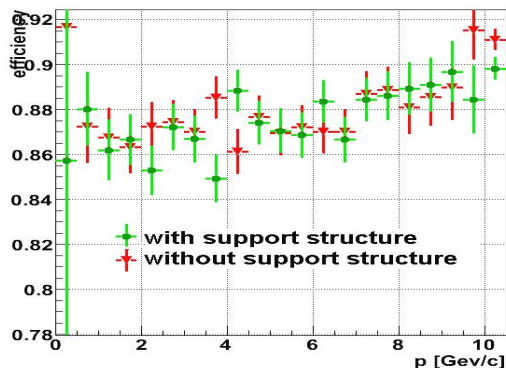


Figure 1: Efficiency of TRD track reconstruction for electrons embedded in central Au+Au collisions at 25 AGeV beam energy for a RICH with 6 mm thick glass mirror

A first step in the RICH geometry optimization with re-

*s.lebedev@gsi.de

Table 1: Comparison of layout parameters for the large and the optimized compact RICH detector

	large	compact
radiator gas	N_2	CO_2
p_{th}^π [GeV/c]	5.6	4.65
λ_{th} [nm]	<160	~ 175
radiator length [m]	2.5	1.5
full length [m]	2.9	1.8
mirror radius [m]	4.5	3
mirror size [m^2]	~ 22.8	~ 11.8
photodetector size [m^2]	~ 9	~ 2.4
No. of channels	$\sim 200k$	$\sim 55k$

spect to minimizing its dimensions was already made in the previous year [3]. In 2008, progress has been achieved in the optimization of the new "Compact" RICH layout. Table 1 compares the now established Compact with the previous "Standard" RICH geometry. This layout was optimized in particular with respect to the photodetector and mirror positions as these influence the ring parameters. Several parameters were chosen to be optimized, among them the RICH detector acceptance, which is here defined as the number of accepted electrons (more than 5 hits in RICH) divided by the number of generated electrons with parameters $\theta = (2.5^\circ, 25^\circ)$, $\phi = (0^\circ, 360^\circ)$ and $p_t = (0.1, 3)$ GeV/c. In addition, the distribution of minor (B) and major half axis (A) of the ellipse, the B/A ratio, the number of hits per electron ring, and the hit and ring density were investigated.

Different geometries were simulated and investigated in order to find the best one. As a reference point, the standard RICH layout was taken, which has a mean acceptance of 89%, $\langle A \rangle = 6.1$ cm, $A_{RMS} = 0.28$ cm, $\langle B \rangle = 5.6$ cm, $B_{RMS} = 0.22$ cm, $\langle B/A \rangle = 0.9$. The geometry with the best correlation of these parameters was chosen as the optimal one. This optimized compact RICH has a geometrical acceptance of 84%, $\langle A \rangle = 5.08$ cm, $A_{RMS} = 0.39$ cm, $\langle B \rangle = 4.61$ cm, $B_{RMS} = 0.24$ cm, and $\langle B/A \rangle = 0.91$. With this RICH geometry, a performance comparable to the standard RICH setup is achieved [4].

References

- [1] I. Kisel et al., CBM Progress Report 2007, p. 10
- [2] A. Lebedev et al., CBM Progress Report 2007, p. 15
- [3] C. Höhne, CBM Progress Report 2007, p. 17
- [4] S. Lebedev et al., *Electron identification in the CBM experiment*, this report

Development of a CBM-RICH mirror prototype – first measurements

M. Dürr¹, A. Braem², and C. Höhne³

¹University of Applied Sciences, Esslingen, Germany; ²CERN, Switzerland; ³GSI, Darmstadt, Germany

Electron identification in a ring imaging Cherenkov detector (RICH) requires efficient reflection of UV-photons by the spherical mirrors which act as imaging elements. For the CBM-RICH detector, test mirrors based on a standard float glass process were produced by FLABEG GmbH, Furth im Wald, Germany; an example of the $40 \times 40 \text{ cm}^2$ large mirrors is shown in Fig. 1. The reflecting coating consisted of an Al-layer, for protection of the Al-surface, especially to avoid formation of aluminium oxides which are strongly absorbing in the UV-region, a protection layer of MgF_2 was applied. Scanning electron microscopy (SEM) measurements yielded $d_{\text{Al}} = 55 \text{ nm}$ and $d_{\text{MgF}_2} = 120 \text{ nm}$ for the Al- and MgF_2 -layer, respectively.



Figure 1: Photograph of test mirror, the concave profile is easily observed in the reflection on the mirror surface.

The reflectivity of the mirrors as a function of wavelength down to $\lambda = 160 \text{ nm}$ was tested at CERN. The result for one of the mirrors is shown in Fig. 2. One observes high reflectivity down to approx. 300 nm with a first drop in reflectivity at 280 nm and a second, steeper drop around 180 nm . The latter is assumed to be due to the formation of aluminium oxides already during the film growth. The former can be understood in terms of interference between light reflected at the MgF_2 /vacuum interface and light reflected at the Al/ MgF_2 interface. The solid line in Fig. 2 is a simulation taking into account both effects. For the absorbing part, the absorbance of Al_2O_3 was used; with respect to interference, the measured reflectivity curve is reproduced the best if a thickness of the MgF_2 -layer of $d_{\text{MgF}_2} = 110 \text{ nm}$ was applied in the simulations, in very good agreement to the SEM measurements.

Further discrepancies between the measured and simulated curve might be due to microroughness of the mirror surface. As a measure for the surface and interface roughness, atomic force microscopy (AFM) images were taken of the mirror surface (Fig. 3). The surface was found to show a roughness below 10 nm , a similar value was obtained both for the MgF_2 -surface and the Al/ MgF_2 inter-

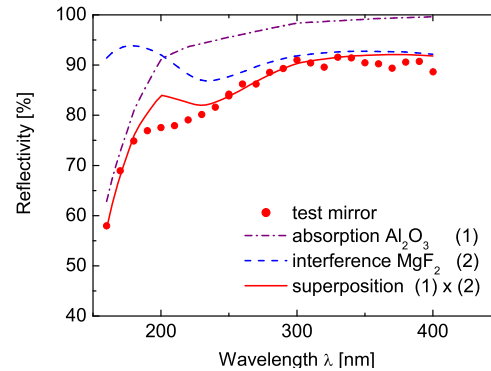


Figure 2: Measured reflectivity as a function of wavelength for one of the test mirrors (dots). The dashed line indicates the effect of interference at a 110-nm-MgF_2 -protection-layer (simulation), the dot dashed line illustrates possible contributions by the absorption of Al_2O_3 . The solid line represents the superposition of the two latter effects.

face when investigated by means of SEM. Further tests included D_0 -measurements. However, due to an uneven surface plane on the cm-scale, only a small fraction of incoming light was found to be reflected into a defined spot.

In summary, overall good reflectivity was measured and optimized growth process parameters might lead to a further improvement of the reflectivity in the short wavelength region avoiding the formation of aluminium oxides. Improvements with respect to surface homogeneity on the cm-scale are mandatory.

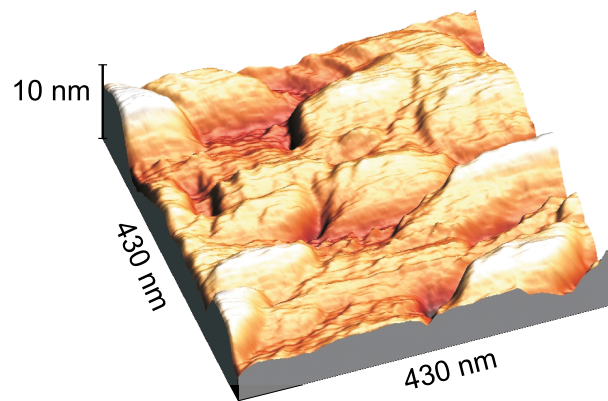


Figure 3: Pseudo-3D-plot of the surface topography as obtained by means of AFM measurements (contact mode). The measured roughness was approx. 6 nm (peak-to-peak).

Research & Development of a mini-RICH Detector with gas radiator as first step towards a CBM-RICH prototype

J.G. Yi*, C.W. Son, J.H. Kim, H.Y. Lee, and I.K. Yoo

Department of Physics, Pusan National University, Pusan, Republic of Korea

In order to optimize the physics performance of the CBM-RICH detector and to investigate different gas radiators, we developed a mini-RICH detector with gas system as a first test prototype in Pusan National University (PNU), Pusan, Korea. This mini-RICH detector was tested with the 60 MeV electron beam at the Pohang Accelerator Laboratory (PAL).

Development of a mini-RICH detector

The developed mini-RICH detector is shown schematically in Figure 1. The detector vessel is constructed as a rectangular box with 10 mm thick aluminium walls, having inner dimensions of $600 \times 400 \times 200 \text{ mm}^3$. The vessel serves as a gas container as well as a darkroom shielding the MAPMT from outside light. The electron beam enters through a Mylar window of 3 mm diameter. A 25.4 mm diameter spherical silver coated aluminium mirror with curvature $R=750 \text{ mm}$ is located at a radiator length $L=500 \text{ mm}$ and rotated by $\alpha=5^\circ$. A 64-pixel MAPMT is centered at $\alpha=10^\circ$ in the focal plane at 375 mm distance from the mirror.

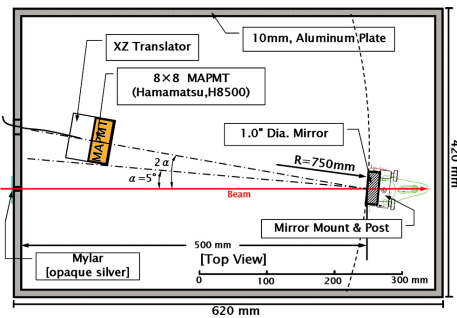


Figure 1: Schematic drawing of mini-RICH (top view).

As photodetector we used the H8500 MAPMT from Hamamatsu, proposed for the CBM-RICH [1]. This MAPMT has a $59 \times 59 \text{ mm}^2$ photocathode effective area divided into 8×8 anode pixels of $5.8 \times 5.8 \text{ mm}^2$ size.

In order to normalize different anode output signals from the same input light to the cathode, we developed a simple method for uniformity measurements using diffusers. This method is shown schematically in Figure 2. Results are shown in Figure 3 in comparison with the values from the Hamamatsu data sheet. Measured QDC values have to be corrected by this uniformity map.

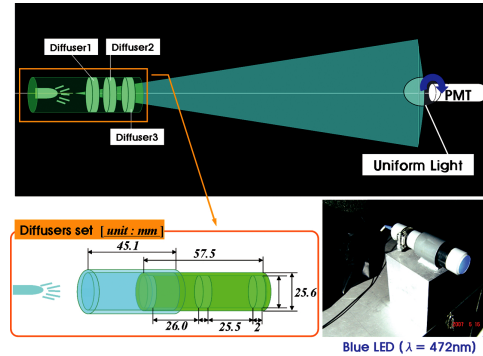


Figure 2: Setup for the uniformity measurement with diffusers at PNU.

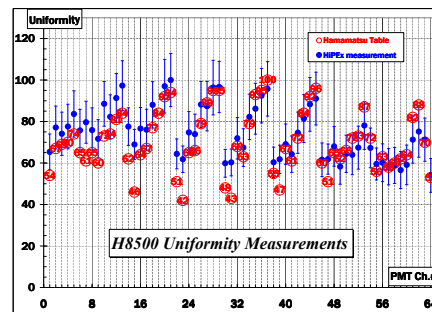


Figure 3: Comparison of the results of our uniformity measurements (blue circles) to data from Hamamatsu (open circles (numbered)).

Radiator Gas and Gas System

A gas radiator with low refractive index ($\gamma_{th} \geq 30$) is needed for an efficient and clean electron identification for $p \leq 10 \text{ GeV}/c$ with a pion suppression of order of 10^3 in the CBM-RICH detector [2]. We therefore used dry-air with $(n-1) \times 10^5 = 29.2$ and nitrogen with $(n-1) \times 10^5 = 29.8$ as probes of gas radiators. They are abundant, non-flammable and have reasonable refractive indices. The gases are provided by a small gas system consisting of an air pump, a buffer tank, an air dryer system with molecular sieve and regulators. The gas system is shown schematically in Figure 4.

In order to monitor the gases, we measured humidity, temperature and pressure. The result of a test operation of the gas system with dry-air was 26°C , 1.04 atm and 10%RH (=1458.8ppm) 100 minutes after start.

Because the humidity of dry-air was larger than several hundred ppm, we changed to a nitrogen gas radiator with lower humidity than dry-air for the mini-RICH detector at

* fireplay@pusan.ac.kr

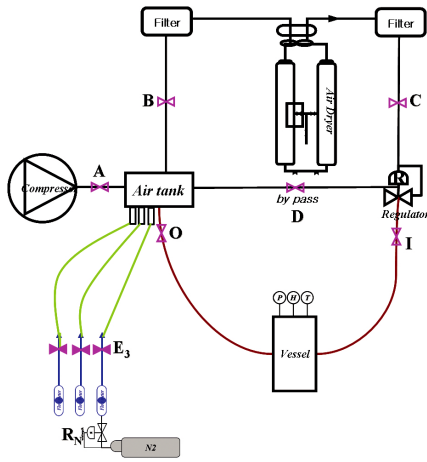


Figure 4: Schematic Diagram of the Gas System

the electron beam test.

Test experiments with the mini-RICH detector

The mini-RICH detector performance was tested with a 60 MeV electron beam at the electron test linear accelerator at the Pohang Accelerator Laboratory (Test LINAC at PAL).

We calculated the ring diameter to be 17.16 mm based on the Cherenkov relation (see table 1) with 60 MeV electron beam, nitrogen refractive index $(n-1) \times 10^5 = 29.8$ and mirror curvature $R=750\text{mm}$. The predicted ring image on the MAPMT cathode plane is shown in Figure 6(a). Due to the short length of the radiator only a few measured photons are expected per electron.

Table 1: Experimental conditions and calculated ring diameter d .

$E_e = 60\text{MeV}, R=750\text{ mm}$	
radiator	N_2
$(n-1) \cdot 10^5$	29.8
$\theta_c [^\circ]$	1.3107
$d = R \cdot \sin \theta_c [\text{mm}]$	17.16

In order to record QDC data, we used CAMAC and NIM modules, only 8 channels were available. Different pixels were grouped together in order to cover the whole surface, and groups were changed for systematic studies. The schematic diagram for the 8 channel coincidence circuit is shown in Figure 5.

Figure 6(b) shows the performance of the mini-RICH detector in the electron beam test. One clearly sees an enhancement of QDC values in the 'Ring region' in comparison with the outer regions by a factor of approximately 1.4. The ring image is smeared because of grouping 8 channels

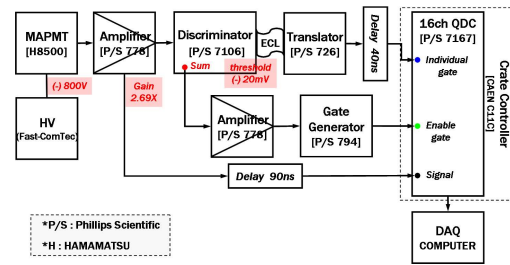
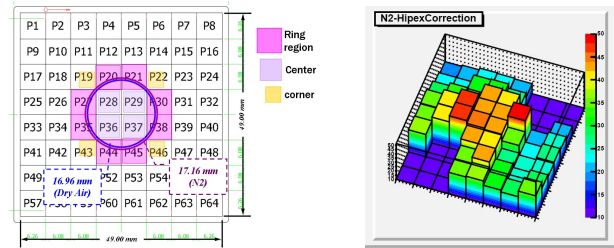


Figure 5: Diagram of the 8 channel coincidence circuit.

together and since only few photons are detected per electron. Furthermore, the electron beam at PAL was rather wide, unstable and unfocused such that the ring was not always at the same position. Work is ongoing in order to improve the beam conditions.



(a) Expected ring size on the MAPMT for a nitrogen gas radiator. (b) QDC values (a.u.) after uniformity correction (PNU).

Figure 6: Calculated and measured Cherenkov ring.

Summary and outlook

We developed and tested the performance of a mini-RICH detector with gas radiator as first step towards a CBM-RICH prototype. After these first steps for gaining experience with the operation of a gaseous RICH detector and with the electron beam at PAL a 2nd RICH prototype is currently being developed which has the same dimensions in length as the current CBM-RICH layout [1] and will have a 2×2 MAPMT photodetector plane which is sufficient to project a full ring image. Performance tests of mirror prototypes, the photodetector and different gas radiators can be made with this detector. Collected data in particular in terms of number of measured photoelectrons per ring can be used for comparison with simulations.

References

[1] C.Höhne, *CBM-RICH layout optimization*, CBM progress report 2007
 [2] C.Höhne *et al.*, Nucl. Instr. Meth. A **595** (2008) 187.

Progress in photodetector development for the CBM RICH

V. Brekhovskikh, V. Dyatchenko, Yu. Kharlov, V. Lapshin, M. Medynsky, P. Stolpovsky, V. Rykalin, and S. Sadovsky

Institute for High Energy Physics, Protvino, 142281 Russia

New design of the PMT FEU-Hive

The first design on the PMT FEU-HIVE [1], developed in 2006–2007 (Fig.1), had several disadvantages:

- lead-in contacts (Kovar rings) were located on the outer surface of the PMT case which would prevent a compact packaging of PMT's to a RICH photodetector plain,
- technology of the glass case and Kovar ring welding is very delicate and demands special equipment,
- production of the Kovar rings, preparation of the rings and glass cases for welding are neither simple nor cheap operations,
- yield of the initial PMT FEU-HIVE with the required gain of the dynode system was not sufficient for PMT mass production.

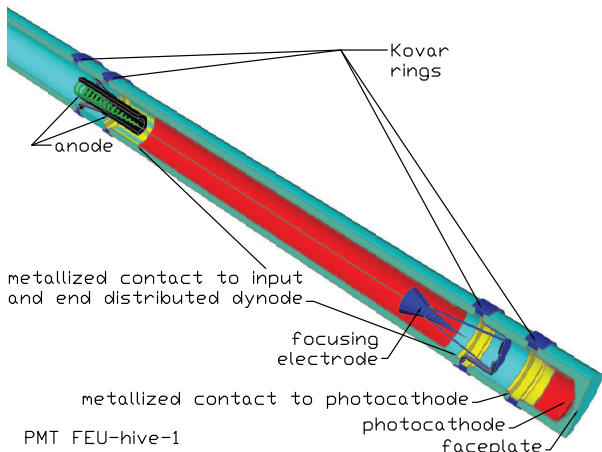


Figure 1: The first PMT FEU-HIVE concept.

These drawbacks of the former design have led to a new design of a small diameter PMT, FEU-HIVE-2, shown in Fig.2, with construction details illustrated in Fig.3. The new PMT construction does not contain any Kovar rings and therefore does not require the difficult and expensive operation of Kovar ring welding with the PMT glass cases. In 2008, first samples of FEU-HIVE-2 were produced using the new design and new production technology of the active dynode layer. The new PMTs are now under study.

Progress with WLS films for RICH

R&D with the wave-length shifter (WLS) films was also continued in 2008 to improve the photodetector sensitivity

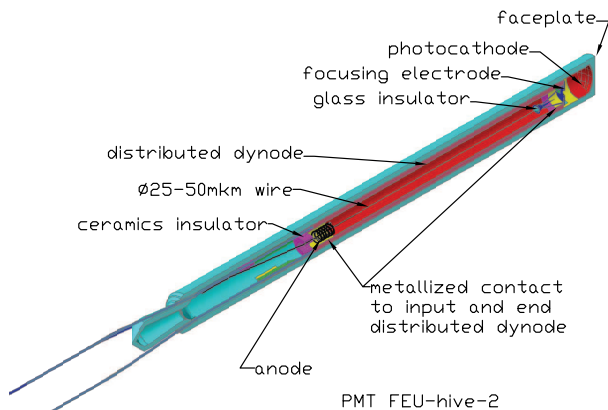


Figure 2: The new PMT FEU-HIVE-2 concept.

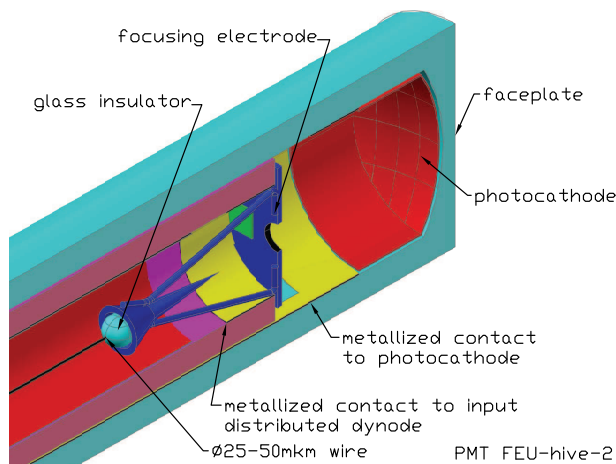


Figure 3: Construction details of the PMT FEU-HIVE-2.

in the ultraviolet light range. In particular, special measurements of WLS film efficiencies were carried out in IHEP using Cherenkov radiation from a MgF₂ crystal excited with a radioactive ⁹⁰Sr source. The film efficiency, defined as the current ratio for a PMT with a film and without, was measured for several films including pure polyethylene, teflon and mylar films as well as WLS films on the base of a teflon film covered by a thin transparent layer of scintillating agent, *p*-terphenyl (PTP) or a mixture of PTP with 1,4-Bis(4-methyl-5-phenyl-2-oxazolyl) benzene (POPOP). A technology of covering a teflon film by PTP or PTP+POPOP layers was developed at IHEP. The influence of the optical grease between film and glass win-

dow on the signal gain was studied as well. The results on the efficiency measurements are represented in Table 1, which demonstrates that the mentioned WLS films with the optical grease improve the photodetector sensitivity from 1.67 to 1.82 times compared to the case of a pure teflon or polyethylene films.

Film type	Efficiency
Mylar without optical grease	0.81 ± 0.06
Teflon without optical grease	0.91 ± 0.06
Polyethylene without optical grease	1.04 ± 0.07
Mylar with optical grease	1.01 ± 0.07
Optical grease	1.38 ± 0.10
Teflon with optical grease	1.57 ± 0.11
PTP on teflon with optical grease	1.68 ± 0.12
Polyethylene with optical grease	1.69 ± 0.12
PTP+POPOP on teflon with optical grease	1.83 ± 0.13

Table 1: Mean values of the PMT signal gains for different films without and with optical grease from the MgF_2 crystal irradiated by a ^{90}Sr source.

This result was also confirmed by direct measurements of the pulse amplitudes from a threshold Cherenkov counter filled with a mixture of air and Freon-12 at atmospheric pressure during beam tests at a 7 GeV/c pion beam of the IHEP U70 accelerator in December 2008. In Fig.4 the amplitude spectra from the Cherenkov counter with the PMT AVP56 without a WLS film (left) and with the PTP+POPOP layer on a teflon film and with optical grease on the PMT window (right) are shown. All other conditions were kept the same. It is clearly seen that the pion amplitude increased ~ 1.6 times when using the WLS film. This actually corresponds to using a quartz PMT DUVP56 without a WLS film.

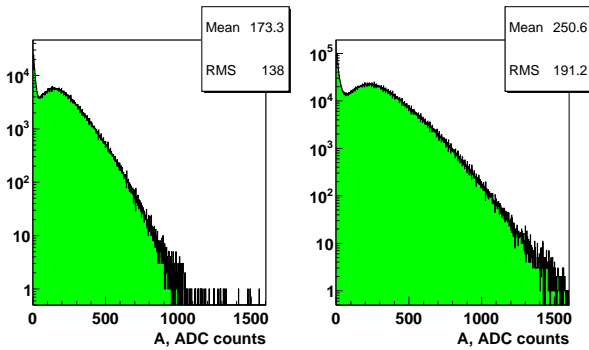


Figure 4: Amplitude spectra of the threshold Cherenkov counter in a 7 GeV/c pion beam without WLS film (left) and with the PTP+POPOP WLS film and optical grease on the photocathode window of PMT AVP56 (right).

Another R&D activity with WLS films aimed to clarify the timing characteristics of the WLS radiation. The measurements carried out in IHEP have shown that the radiation mechanism of pure polyethylene and teflon films are different from the mechanism of PTP and PTP+POPOP

based films. Particularly in the case of PTP+POPOP on a teflon film the shift and expansion of the WLS time spectra relatively to the initial hardware spectra (it is measured in the absence of WLS films) are appreciable. The spectrum time shift in this case reaches a value of 1 ns, see Fig.5. In a case of polyethylene-based films the resolution of the

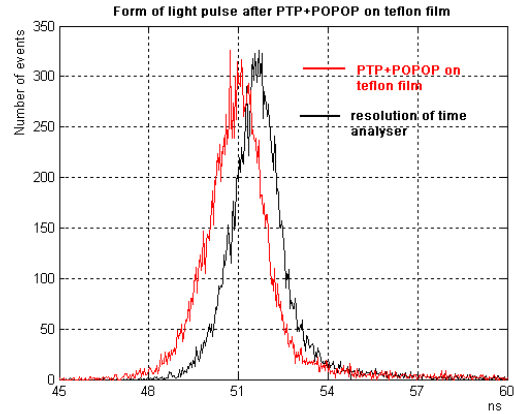


Figure 5: Timing properties of the teflon based WLS films.

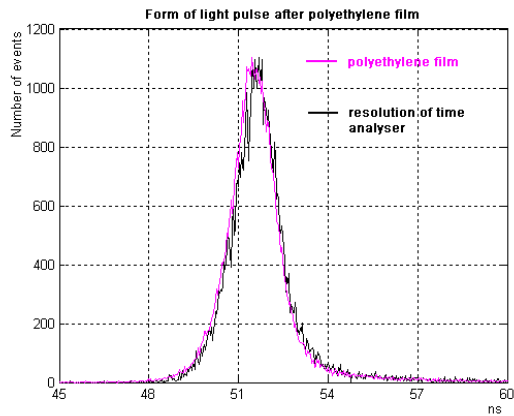


Figure 6: Timing properties of the polyethylene based WLS films.

used time analyzer does not allow to confirm any observable time shift connected with fluorescence of these films. The measured time spectra for this case are shown in Fig.6. The observed effect of increased gain for pure films is currently not explained and requires further studying.

We conclude, that the RICH photodetector option on the base of the small diameter PMT FEU-Hive in combination with WLS films on the PMT photocathode window is on a good track.

References

[1] V.Brekhovskikh et al., CBM Progress Report 2006, p.32.

Investigation of wavelength shifter properties of p-terphenyl and TPB

P. Koczoń¹, C. Höhne¹, M. van Stenis², A. Braem², and C. Joram²

¹GSI, Darmstadt, Germany; ²CERN, Geneva, Switzerland

Abstract: Wavelength shifter materials like p-Terphenyl and Tetra Phenyl Butadiene (TPB) of thicknesses between 65 and 250 $\mu\text{g}/\text{cm}^2$ have been studied in order to improve the quantum efficiency (QE) of a photomultiplier in the UV range. The best result has been obtained for p-Terphenyl of 100 $\mu\text{g}/\text{cm}^2$ thickness. In this case the quantum efficiency integrated over a broad range of photon energies up to 6.2 eV shows a gain of a factor 1.6 compared to an uncovered photomultiplier.

Introduction

The rate of photons from Cherenkov radiation per energy bin is constant ($dN/dE = \text{const}$) therefore the bulk of the photons is produced in the UV and far UV region. The quantum efficiency of standard photomultipliers with glass windows reaches only 25% around 400 nm and drops down essentially to 0% below 250 nm. The aim of this work

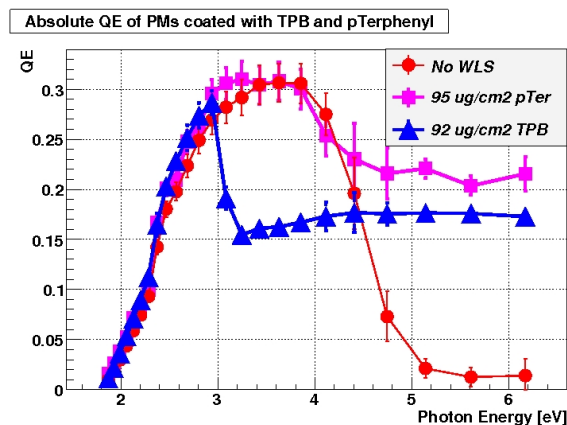


Figure 1: Quantum efficiency versus photon energy for the uncoated PMT (Photonis XP3102) and with TPB and p-Terphenyl coating.

was to reinvestigate the potential of the quantum efficiency improvement in the UV region using wavelength shifting substances on top of the glass window.

Technical details

Two of such wavelength shifter substances have been evaporated in vacuum with well controlled thickness on the entrance windows of several Photonis XP3102 photomultipliers. The quantum efficiency of those photomultipliers was measured in a wavelength range from 200 to 650 nm in a monochromator by comparison to an absolutely calibrated photodiode [1].

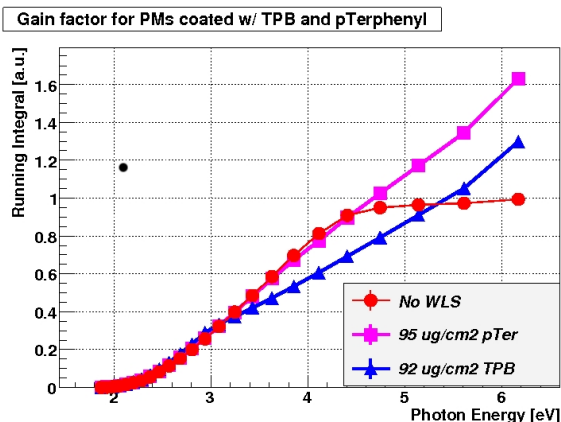


Figure 2: Gain of quantum efficiency obtained by integration of the QE curves from Fig. 1.

Results

Fig. 1 shows the improvement of the quantum efficiency as a function of photon energy for 95 $\mu\text{g}/\text{cm}^2$ p-Terphenyl and 100 $\mu\text{g}/\text{cm}^2$ TPB evaporated on the entrance window of the PMT compared to the quantum efficiency of an untreated PMT. TPB improves the efficiency for highest energies (around 5 eV=246 nm) moderately but deteriorates it in the visible region by a factor of 2. For p-Terphenyl we observe a clear improvement of QE in the UV and no change in the visible range. In order to quantify the overall QE improvement all curves have been integrated over the whole energy range. Running integrals are presented in Fig.2 and compared to the integral of the pure PMT (which is normalised to 1 at 6 eV). The value of the running integral for TPB lies below the reference PMT between 3.2 and 5.3 eV and finally reaches a gain of 30% only. The result for p-Terphenyl clearly shows a gain of 60% above the uncovered PMT. Extrapolating to the far UV one can expect still higher gain values.

In order to investigate possible ageing processes of the wavelength shifter film in the radiator gas of the future RICH detector of CBM at FAIR the photomultipliers with an evaporated p-Terphenyl layer have been stored in CO_2 atmosphere and will be remeasured to monitor their performance every 6 - 12 months.

References

- [1] A. Braem et al., NIM A 504 (2003) Pages 19-23

Optimization of the CBM muon detection system

A. Kiseleva¹, C. Höhne¹, E. Kryshen², A. Lebedev¹, and M. Ryzhinskiy³

¹GSI, Darmstadt, Germany; ²PNPI, Gatchina, Russia; ³SPbSPU, St.Petersburg, Russia

The experimental challenge for muon measurements in heavy-ion collisions at FAIR energies is to identify low-momentum muons in an environment of high particle densities. The CBM concept is to track the particles through a hadron absorber system and to perform a momentum-dependent muon identification. This concept is realized by segmenting the hadron absorber in several layers and placing triplets of tracking detector planes in the gaps between the absorber layers. The iron absorbers are located downstream from the Silicon Tracking System, which provides the momentum measurement. To reduce meson decays into muons, the absorber/detector system has to be as compact as possible.

The absorber layout was optimized in simulations performed for central Au+Au collisions at 25A GeV. The primary particles are produced with the UrQMD event generator, and the GEANT3 transport code is used to propagate the particles through the material and to create secondary particles. The hit density in the first detector layer behind an iron absorber of 10 cm thickness is about 1 hit (cm² event)⁻¹. This hit density would result in a detector pad size of 1.4×2.8 mm² if the occupancy should be kept below 5%. The particle multiplicity behind the first absorber can be reduced by increasing the thickness of the iron plate. In this case, however, small angle scattering in the absorber material is increased, and the matching efficiency between the ingoing and outgoing tracks decreases. In order to find a compromise between detector granularity and matching efficiency we have conducted a study in which the thickness of the first iron absorber has been optimized with respect to the detector granularity and the number of reconstructed background tracks.

In a first step, we studied the particle multiplicity behind the first iron absorber layer as a function of the absorber thickness. The result is shown in fig. 1 for (primary and secondary) particle multiplicities per event detected behind an iron absorber of variable thickness. The multiplicity at zero thickness corresponds to the number of particles in front of the absorber. The particle multiplicity is dominated by the yield of secondary electrons, which rises steeply up to an absorber thickness of about 5 cm and then drops with increasing material thickness.

The particle multiplicity varies also strongly with the radial distance from the beam as shown in the left panel of fig. 2 for different absorber thicknesses. This effect is important for the segmentation of the tracking chambers into pads, which may vary in size by more than one order of magnitude from the inner to the outer area of the detector.

In a second step, we investigated the influence of the thickness of the first iron absorber on the track reconstruction

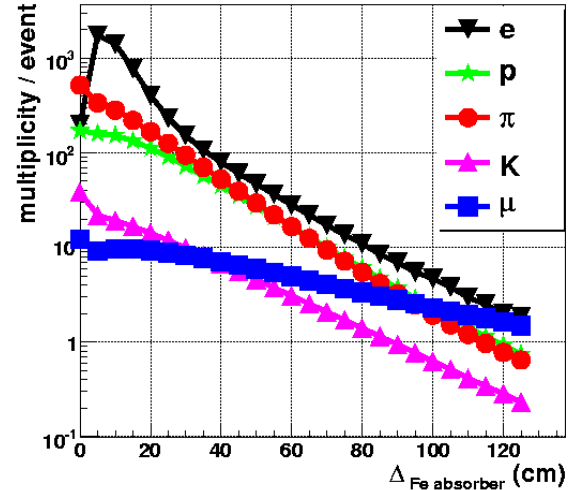


Figure 1: Particle multiplicity per event as a function of iron absorber thickness

performance. For this study, we used a complete muon detection system consisting of 5 absorber layers and 15 tracking chamber planes, grouped in triplets behind each absorber slab. The total absorber thickness is kept constant to 125 cm, whereas the thickness of the first layer is varied between 10 and 40 cm. After track reconstruction, we calculated the invariant-mass spectrum which represents the background for the dimuon measurements. The resulting spectra are shown in the right panel of fig. 2 for different thicknesses of the first absorber layer. It turns out that the background increases by almost one order of magnitude when increasing the thickness of the first absorber layer from 10 cm to 40 cm. In summary, a first iron absorber of 20 - 30 cm thickness seems to be the best compromise between hit density and background tracks.

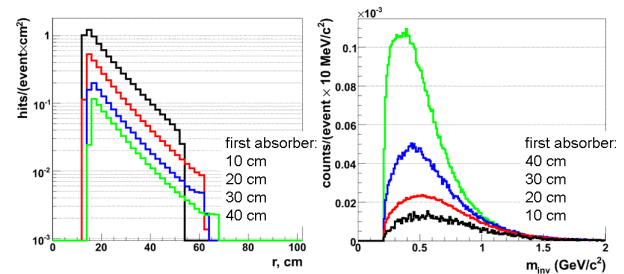


Figure 2: Number of hits per event (left) and invariant-mass spectra of reconstructed background tracks (right) for different thicknesses of the first absorber

Detailed geometry for MUCH tracker and FEE requirements*

E. Kryshen¹, V. Nikulin¹, and M. Ryzhinskiy^{1,2}

¹PNPI, Gatchina, Russia; ²SPbSPU, St-Petersburg, Russia

Tracker design

The general implementation of the MUCH tracking system in *cbmroot* has not changed a lot compared to the version of 2007: each tracking station consists of two chambers located in the gap between absorbers while the last trigger station consists of three chambers. However, the description of the tracking subsystem in the head version of *cbmroot* is much more detailed now. According to the currently foreseen design, each chamber is arranged on two support structures (left and right) made of carbon plastics, 1.5 – 2 cm thick. Detection modules are attached to the front and back sides of the supports and filled with an argon-based gas mixture (see Fig. 1). The gas volume is enveloped with noryl spacers, 0.5 cm and 5 cm wide in x and y directions, respectively. The typical size of the modules is about 30×30 cm and is mostly limited by the GEM foil production technology (up to 60×60 cm with the new machine at CERN).

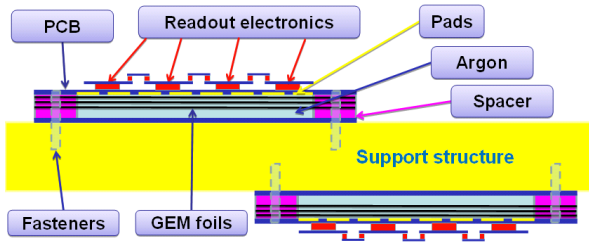


Figure 1: Schematic layout of GEM detection modules

In the head version of *cbmroot*, a flexible and convenient geometry file is provided for the description of the module design. The modules are automatically arranged in rows on both sides of each support plane keeping 2 mm overlap of sensitive volumes essential to avoid dead zones in y direction. Cables, gas tubes, PCBs and front-end electronics are neglected at the moment.

The detection module is logically split in sectors, each sector to be read-out by one 128-channel FEE card. The sector granularity is automatically tuned to keep the channel occupancy below a certain value and to provide a certain spatial resolution. The sector sizes at the first station are mostly determined by occupancy restrictions, while starting from the 3rd station they are limited by resolution requirements. The default chamber segmentation at the first station is shown in Fig. 2. In the case of micromegas technology, the smallest pad size of 2.3 mm (resolution of

$\sim 680 \mu\text{m}$) corresponds to $\sim 5\%$ occupancy in the most dense region around the pipe. Somewhat higher occupancies are expected for the triple GEM detectors.

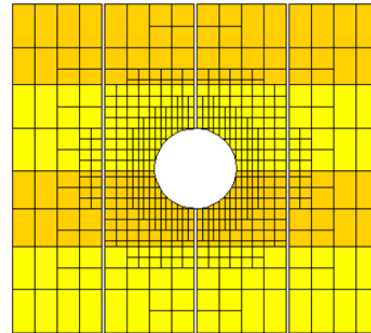


Figure 2: Segmentation at the 1st station: yellow and orange rectangles represent sectors on the front and back sides, respectively.

FEE requirements

In order to evaluate the FEE requirements, the charge induced on pads has been simulated with the MUCH hit producer, assuming a FEE threshold of $4\sigma_{\text{noise}} \sim 6000 - 8000$ electrons and a threshold variation of the order of ± 700 electrons. The efficiency requirement of 99% signals above the FEE threshold allows to estimate the **minimum gas gain**: 5000-10000 for argon-based gas mixtures and more than 10000 for helium-based gases.

In order to preserve multi-hit cluster deconvolution efficiency and good spatial resolution, ADC overflows should be minimized to the level of about 3%. This results in the requirement of **maximal digitized charge** about $2 - 4 \times 10^6$ electrons, where possible gas gain variation over the surface of the detector module has been taken into account. Preliminary estimates indicate that non-linear amplifiers with the **8 bit charge measurement precision** (256 channels) are required for the efficient cluster deconvolution.

The required granularity (pad size of about 4 mm^2 at most dense zone) results in the maximum limit for the **FEE card size** under 4 cm^2 . However, the FEE cards could be partly placed on horizontal spacers, so the card could be about 20 – 30% larger. The total height of the card including all the connectors and the connecting cables is estimated on the level of 15 mm. The card should also contain **spark protection circuits** at the input of the FEE chip.

*Work supported by INTAS contract No. 05-103-7484.

Segmentation study of the CBM Muon Detector *

D. Dutta †, A. Kiseleva, and C. Höhne

GSI, Darmstadt, Germany

This contribution pursues a first step towards a full detector design study for the CBM Muon Chamber(MUCH) detector. For a realistic detector design and optimization of the detector layout with respect to the physics signals, a simple description of the segmentation of the detector is required allowing for more flexibility. The present study demonstrates a new “Flexible Segmentation Scheme” (FSS) with multidimensional flexibility which needed to develop a detailed detector layout.

The aim of the present segmentation study is to get a realistic description of the MUCH detector. In order to take into account the variation of the hit density with the distance from the beam axis, the MUCH stations are segmented in different annular regions with appropriate pad size (rectangular in this case) required to achieve the desired hit occupancy. Nine different regions are defined sequentially doubling the pad area. A segmentation scheme was achieved already earlier[1] based on 5% hit occupancy, where the radius of each ring-like region was chosen such that the mean hit density got reduced by a factor of 2 in adjacent regions and correspondingly the pad area was doubled. However, for a realistic detector design, the pad sizes and detector layout should be developed in close connection to the detector R&D. It is essential to have a maximum coverage within the detector acceptance. The present study implements a “Flexible Segmentation Scheme”(FSS) which is essential for the optimization of the detector layout. The following flexibility is achieved in the present scheme:

- Flexible number of regions with different pad sizes in each detector.
- Flexible radial size of each ring region.
- Flexible number of channels.
- Flexible pad size.

The first step of the optimization of the detector layout is to study the hit reconstruction efficiency. In the present study, a CBM Muon Chamber (MUCH) geometry is used which consists of 15 tracking stations made up of GEM detectors, sandwiched between 5 iron absorber layers of variable thickness (125cm in total) with an additional shielding near the beam pipe. Events are generated using the UrQMD event generator for central Au+Au collisions at 25A GeV and transported through the detector setup using a transport code based on GEANT3 in the CBMROOT simulation framework. Hits are generated from the pad centre of the GEANT Monte Carlo(MC) points.

Figure 1 shows the hit efficiency in % (No. of Hits/No. of MC Points) from the “Flexible Segmentation Scheme”

* Work supported by EU/RP7, JCT-WP6 No. 50706.

† D.Dutta@gsi.de

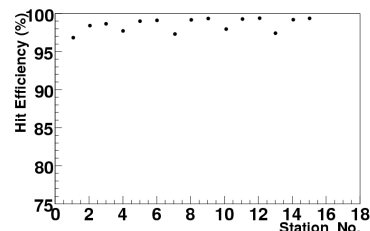


Figure 1: Hit efficiency in % from the “Flexible Segmentation Scheme” for different stations of MUCH.

for different stations. The segmentation of detector stations is optimized with respect to the hit efficiency in the FSS. The regions and pad dimensions used in FSS for different stations are described in Table 1. The minimum pad dimension is 2.77mm×5.54mm which is well suited for GEM detectors. Figure 1 shows average hit efficiency $\approx 98\%$ which reflects a good match of the reconstructed hits with the MC points in the present FSS scheme throughout all the stations. Hit efficiency loss by 3% in the first station of each triplet is due to multiple hits in the presence of secondary electrons from the absorber.

Table 1: Ring regions and pad dimensions in different stations used for estimating the hit efficiency with FSS

Stations	Region No.	Radius (cm)	Pad size (cm × cm)
1,2,3	3	13.7 -25.0	0.277 × 0.554
	4	25.0 -45.0	0.554 × 0.554
	5	45.0 -62.3	0.554 × 1.108
4,5,6	4	17.4 -32.0	0.554 × 0.554
	5	32.0 -48.0	0.554 × 1.108
	6	48.0 -81.4	1.108 × 1.108
7,8,9	5	21.4 -40.0	0.554 × 1.108
	6	40.0 -56.0	1.108 × 1.108
	7	56.0 -100.5	1.108 × 2.217
10,11,12	5	26.2 -40.0	0.554 × 1.108
	8	40.0 -124.5	2.217 × 2.217
13,14,15	6	31.5 -50.0	1.108 × 1.108
	9	50.0 -151.0	2.217 × 4.434

The present segmentation scheme shows a good coverage of the detector acceptance with pads and a good hit efficiency with negligible loss due to multiple hits for a simple detector layout. The final layout of the detector will be optimized by studying the physics signals. Next step is a realistic description of detector signals using routines for producing real charge distributions.

References

- [1] E. Kryshen et al. *Digitization and hit finding in the CBM muon detector*, CBM Progress Report 2007.

Preliminary simulation results of THGEM geometry and detector gas for CBM muon detector

P. Garg, A. Prakash, V. Singh, C. P. Singh, and B.K. Singh*
 Banaras Hindu University, Varanasi-05, India

The CBM muon detector for the detection of dimuon pairs of J/ψ and light vector meson decays as possible probes for chiral symmetry restoration and deconfinement has been proposed by Indian collaboration. The muon detector located after STS consists of 16 detector layers with $100 \mu\text{m}$ position resolution. For first few layers of detectors thick gas electron multiplier (THGEM) is one of the suitable choices. It is an augmented version of GEM detector based on gas multiplication in small sub-millimeter to millimeter diameter holes in standered double-face Cu clad printed circuit board.

As a first step, we have started to study about THGEM geometry which combines the concept of hole drilling in polimide with chemical eaching of the rim around each hole with Cu as is shown in figure 1(a) with Maxwell [1]. The equipotential contours read by Garfield [2] are shown in figure 2(a). Electric field surface in y - z viewing plane for $\Delta V= 600 \text{ V}$ is computed in figure 2(b) with the help of Garfield. Here vertical axes shows the electric field in V/cm . The spikes are due to the corners in the THGEM geometry as shown in figure 1(a) and electric field strength near the center of the hole is about 6 kV/cm shown in figure 1(b). So the electrons deposited by ionizing radiation are focused into the THGEM hole by strong electric field. The field strength can be tuned by changing the hole diameter.

To study the gaseous detector performance drift velocity for spatial resolution, diffusion coefficient for radial spread, townsend attachment for secondary ionization, dissociation coefficient, ionization and excitation rates play the crucial role. The variation of some of these parameters with electric field is shown in figure 3 for 70% argon and 30% carbon dioxide gas mixture at 300K temprature and 1 atm pressure with the help of magboltz [3].

Further investigations are to be done to optimize these parameters according to the shape and size of THGEM geometry. Also different gas mixtures at different conditions may also affect the detector functioning and need to be optimized accordingly.

References

- [1] MAXWELL-SV, Ansoft Co.USA.
- [2] GARFIELD; simulation program for gaseous detectors written by R.Veenhof, CERN Version 7.02.
- [3] Magboltz2; written by Stephen Biagi, University of Liverpool, UK.

* bksingh@bhu.ac.in

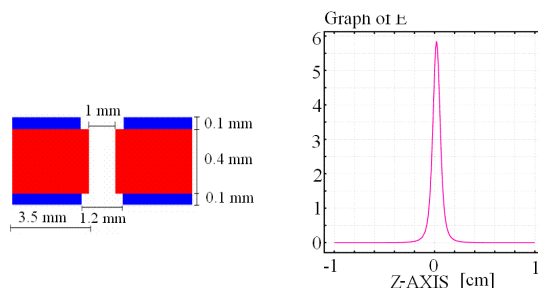


Figure 1: (a) Model used for Maxwell-2d (b) Graph of electric field inside the THGEM hole.

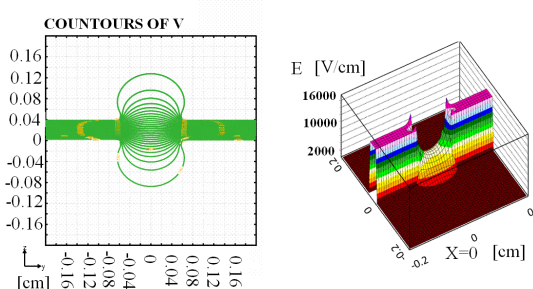


Figure 2: (a) Contour plots (y - z plane) (b) Electric field surface by Garfield.

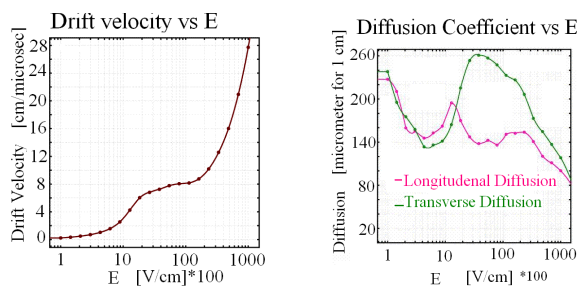


Figure 3: Drift velocity and diffusion coefficient Vs Electric field graphs by Magboltz at normal temp. and pressure for 70% Ar and 30% CO_2 .

R&D of Micromegas, GEM, TGEM and GEM/Micromegas based detectors for the CBM muon detection system

E. Chernyshova, V. Ivanov, A. Khazadeev, B. Komkov, L. Kudin,
G. Rybakov, E. Rostchin, S. Volkov¹

¹PNPI, 188350, Gatchina, Russia

The current detector R&D concentrates on the design of fast and highly granular gaseous detectors, based on Micromegas, GEM and TGEM technologies, for the muon detection system. Prototypes of all three types of detectors of all three types were designed, assembled and tested (Fig. 1a). For the first tests we used an Ar/CO₂ (90/10) gas mixture as working gas.

In the **Micromegas** prototype the rolled stainless steel woven mesh (wire 32 μm in diameter, cell size 64 μm) of Russian production was used. The mesh was placed on pillars of 75 μm height which were prepared with standard technology from photo-resistant layer on readout anode by chemical etching (distances between pillars 4 mm and they were 300 μm in diameter each). Fig. 1b shows an example amplitude spectrum for Fe⁵⁵. The energy resolution of about 15% is close to the literature numbers [1]. The pulse width of the signal, mainly defined by collection of ions in mesh-anode gap, is ~ 180 ns (FWHM). A gas gain of $\sim 3 \cdot 10^4$ is easily reached at a voltage of 500 V.

GEM foils of CERN production were used in the GEM prototype. Fig. 1c shows an example of the amplitude spectrum for Fe⁵⁵. The energy resolution of $\sim 12\%$ is comparable with literature data [2]. A gas gain of $\sim 1.2 \cdot 10^3$ was reached at 500 V applied to the GEM.

The **TGEM** prototype was based on a TGEM technology developed at PNPI. A record precision of 2-3 μm for the position of the rims relative to the holes was achieved. Fig. 1d shows an example of the amplitude spectrum (Fe⁵⁵) for one of the produced TGEMs (this TGEM was done from 1 mm FR4, had holes of 0.4 mm in diameter and rims of 20 μm). The reachable gas gain in case of TGEM was of about 10 times higher than for the GEM case.

We repeated tests of all prototypes with a **He/CO₂ (90/10)** gas mixture. This mixture showed the same reachable gas gains under the same high voltage regimes. There are two reasons to use this gas. At first, collection of ions from avalanche is faster in He than in Ar. This is especially important for Micromegas, where the pulse width of a signal was reduced to ~ 90 ns (FWHM). Second, He is 4-5 times less sensitive to photons than Ar and has lower probability of discharge.

Next, a prototype with two stages of gas amplification (**GEM+Micromegas**) was assembled and tested using **He/CO₂ (90/10)** gas mixture. Main reason to investigate GEM+Micromegas combination [3] is to have a detector with soft high voltage regime to make discharge probability and discharge energy as low as possible. The current design of front-end electronics for muon chambers supposes gas gains not higher than $2 \cdot 10^4$. This value of gas gain

in GEM+Micromegas prototype was reached under equal, rather low, voltages of 400V applied to the GEM and to the Micromegas (visible discharge problems occurred after voltage value of ~ 480 V applied). Fig. 2 (a,b) present first results on estimation of efficiency and discharge probability obtained with β -source (Sr⁹⁰).

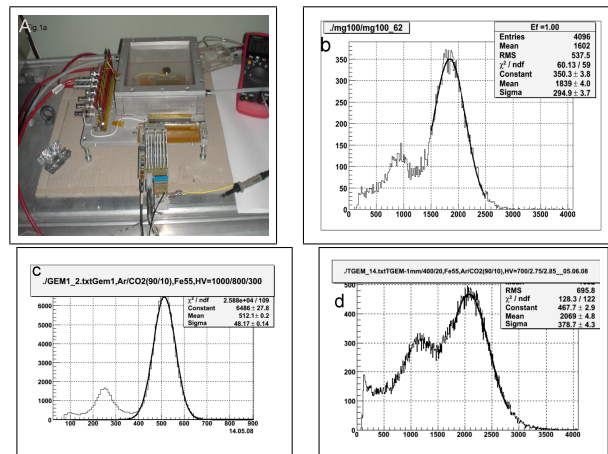


Figure 1: Prototype (a) for assembling Micromegas, GEM and TGEM structures. Amplitude spectra (Fe⁵⁵, Ar/CO₂ (90/10) mixture) measured with Micromegas (b), GEM (c) and TGEM (d) prototypes.

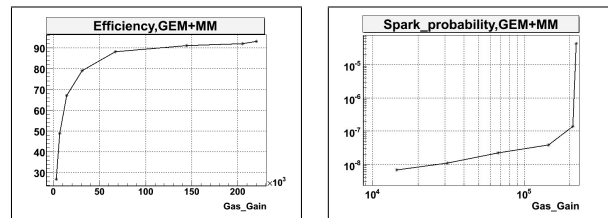


Figure 2: Efficiency (a) and discharge probability (b) measured with Micromegas+GEM prototype (Sr⁹⁰ source, He/CO₂ (90/10) mixture).

References

- [1] F. Sauli, Nucl. Instr. and Meth. A386 (1997) 531
- [2] A. Delbart, Micro-pattern Gaseous Detectors Workshop (09/10-2007, CERN)
- [3] A. Delbart et al. Nucl. Instr. And Meth. A478:205-209, 2002

Multi-GEM prototypes for muon detection in CBM experiment

A. K. Dubey, M. S. Ganti, S. Chattopadhyay, R. N. Singaraju, J. Saini, and M. R. Dutta Majumdar
 Variable Energy Cyclotron Centre, Kolkata, India

Double GEM [1] and triple GEM chambers were assembled at VECC for tests with radioactive sources in lab and with proton beams. The GEM foils which were procured from CERN, had an active area of 10 cm × 10 cm. The stacked assembly was biased via a resistive chain network in a symmetric configuration thereby keeping all the GEMs at the same voltage gradient across their surfaces. The initial tests with radioactive sources in lab were carried out using a single 1 cm × 1 cm pad for signal readout. The data were acquired via standard NIM electronics coupled to an MCA.

Fig. 1 shows an ⁵⁵Fe spectrum from a double GEM chamber. The two ⁵⁵Fe peaks are clearly visible, with the one at higher channel corresponding to 5.9 keV X-rays. The variation of signal amplitude or this peak pulse height with different values of ΔV_{gem} is shown in Fig. 2. The corresponding variation of gain is shown in Fig. 3. It varies exponentially with the voltages across the GEMs in the range of voltages studied. Gains of the order of 10⁴ and an energy resolution of 25% have been achieved using a double GEM combination. The typical drift fields, transfer and inductive fields are about 2 kV/cm, 3 kV/cm and 4 kV/cm, respectively.

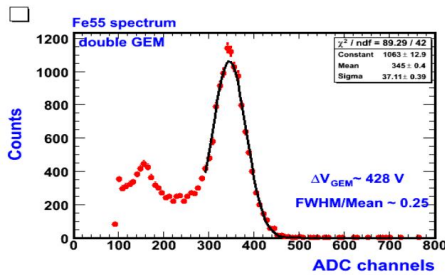


Figure 1: Pulse height from ⁵⁵Fe source for a double GEM chamber

Multi GEM prototypes having a 256 pad readout were fabricated at VECC for test with proton beams at GSI during Sep-2008. Each pad is of 3.5 mm x 8 mm in size and arranged in form of a staggered layout as shown in Fig. 4. The pads were connected to 68 pin ERNI connectors, from where it was coupled to an n-XYTER [2] readout board. Only one half of the detector(128 channels) was connected at any moment as indicated by the marked zone in the picture. A 10 Ω resistor was soldered close to every pad to protect the electronics against any foreseeable sparks. It was also for the first time that the GEM detector was being tested with n-XYTER readout chip which is currently used for several CBM detector prototypes.

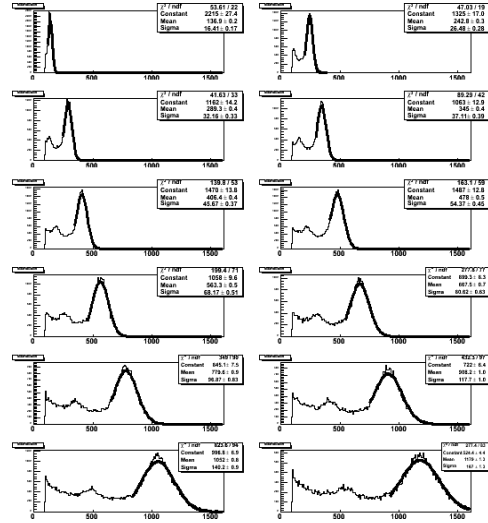


Figure 2: Pulse height spectra for a double GEM chamber using ⁵⁵Fe source at varying voltages

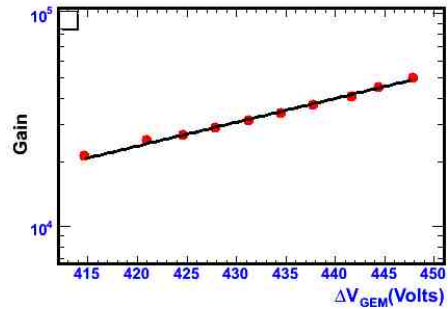


Figure 3: Variation of gain with ΔV_{gem} for double GEM chamber

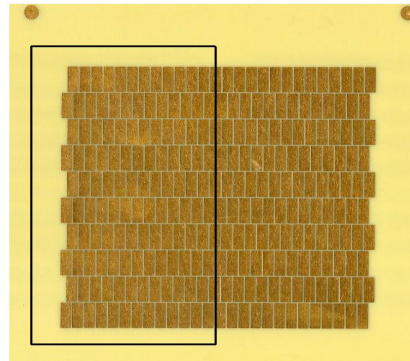


Figure 4: readout board consisting of 256 pads (each having a size of 3.5 × 8mm²) arranged in a staggered manner.

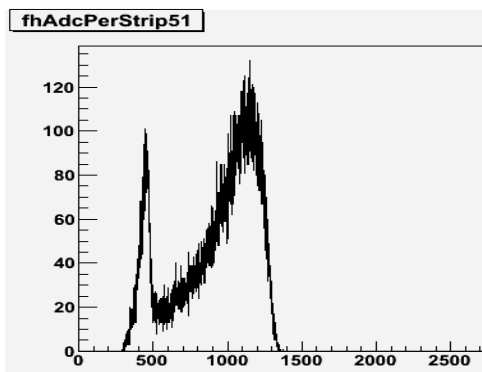


Figure 5: Signal from triple GEM chamber using ⁹⁰Sr and n-XYTER readout. The highest signal appears at lowest ADC channel and vice versa. The peak at the lower channel thus denotes the saturation point of the signal.

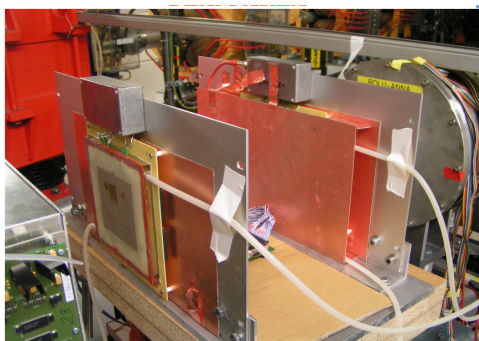


Figure 6: GEM chambers as mounted in the SIS-18 test beam area

Fig 5 shows the ADC raw data spectra from a triple GEM assembly using ⁹⁰Sr source. The highest signal correspond to lowest ADC values. Thus the shape of the spectrum is reversed and the peak at lower channel denotes the saturation point.

Fig 6 shows the double and triple GEM prototypes as mounted in the SIS-18 beamline for tests with protons. Fig. 7 shows the pulse height spectrum for a triple GEM chamber corresponding to protons of 2.3 GeV. The distribution is fitted with a Landau showing a good MIP like shape. A 2D picture of the hit pads accumulated from a large number of events is shown in Fig 8, indicating the beam spot. Since only the alternate channels were bonded in the n-XYTER board, the picture shows a chequered pattern.

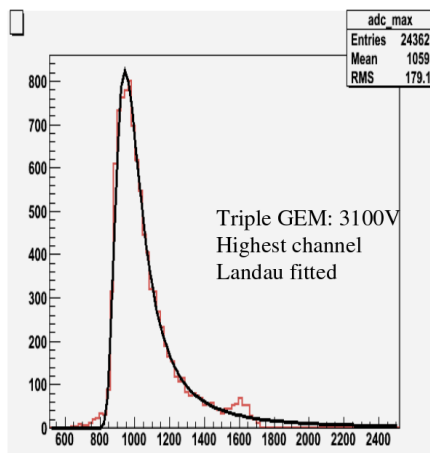


Figure 7: pulse height spectra from a 2.3 GeV proton beam (after reversing the n-XYTER ADC channels offline for the ease of Landau fitting)

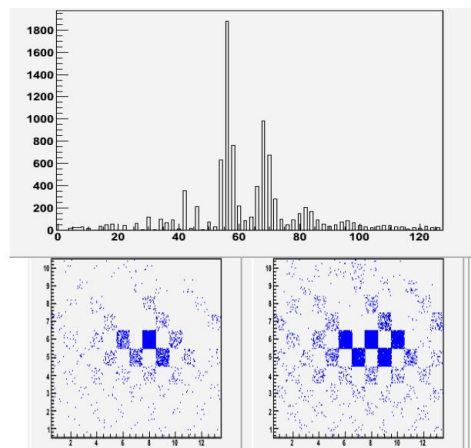


Figure 8: The upper panel shows the hit distribution of the pads while the lower panel shows the 2D picture in x and y.

References

[1] F. Sauli, Nucl. Instrum. Methods A386(1997) 531. (1997) 56.
 [2] NIM A, 568 (2006) 301-308; CBM progress report 2006, p-49.

Feasibility evaluation of the straw tube detector option for the CBM muon system

A. Zinchenko¹, D. Peshekhonov¹, V. Peshekhonov¹, and L. Naumann²

¹JINR, Dubna, Russia; ²FZ Dresden-Rossendorf, Germany

The emission of lepton pairs out of the hot and dense collision zone of heavy ion reactions is a promising probe to study the electromagnetic structure of hadrons under extreme conditions. The reconstruction of vector mesons ($\rho, \omega, \phi, J/\psi, \psi'$) is one of the prime tasks of the CBM experiment. To perform such a study using the dimuon decay mode, a muon system consisting of a set of absorbers and detector stations will be built.

Since the muon absorber should efficiently suppress the particle flux, the downstream detector stations can be made using detector technologies different from those in the first stations. The straw tube option looks quite promising because of the good coordinate resolution of such detectors ($\sim 200 \mu\text{m}$ in the drift direction) and the fact that they have been widely used for more than a decade, and this detector technology has shown to be rather simple and reliable [1].

A possible muon system configuration is shown in Fig. 1, where the last 3 detector stations (behind absorbers 4-6) are built from the straw tubes. Each station consists of 3 double layers (doublets) rotated around the beam axis to create stereo views. Three doublets of the same station, separated in z by some distance, can be used to create track vectors necessary for efficient suppression of the background.

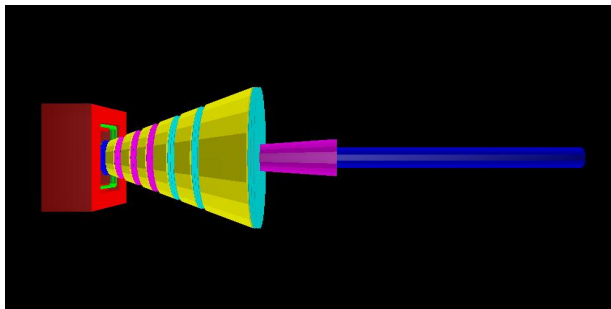


Figure 1: CBM muon system configuration with the three last detector stations (behind absorbers 4-6) built from straw tubes

To check the ability of the straw detectors to work in the CBM experimental conditions, the simulation and reconstruction software has been modified to properly handle the new detector type. The Monte Carlo simulation has shown that the detector occupancy (the most limiting factor of the tubes) can stay within acceptable limits even with the maximum tube lengths covering the entire absorber diameter (Fig. 2). In addition, it is possible to further reduce the occupancy by segmenting the anode wires [2, 3].

It is planned to further proceed in the direction of eval-

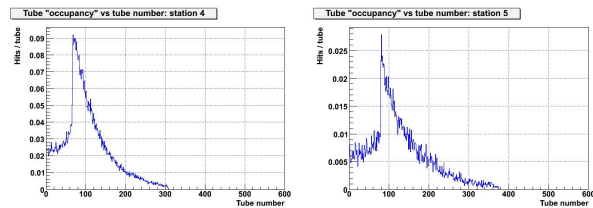


Figure 2: Occupancy (average number of hits per event per tube) versus tube number in muon stations 4 and 5 for Au+Au collisions at 25.4 GeV. The straw tube diameter is 4 mm.

uating the muon system performance with straw tube stations and optimizing the detector geometry (in particular, tube diameter and stereo angle).

The foreseen software changes aim at the possibility to use the same Monte Carlo event samples for different detector options by simulating detector specific features at the digitization level.

References

- [1] G. D. Kekelidze and V. D. Peshekhonov, Phys. Part. Nucl. 33 (2002) 343, Fiz. Elem. Chast. Atom. Yadra 33 (2002) 669
- [2] V. D. Peshekhonov, *Development of a large segmented double layer straw prototype*, 12th CBM Collaboration Meeting, Dubna, 2008, http://cbm2008-oct.jinr.ru/files/15_MUCH_15-00_Peshekhonov.pdf
- [3] K. Davkov et al., Nucl. Instrum. Meth. Phys. Res. A 584 (2008) 285

Segmented straw tubes for CBM-MuCH *

V. Peshekhonov¹, S. Bazylev¹, K. Davkov¹, V. Davkov¹, V. Karabov¹, G. Kekelidze¹, V. Lutcenko¹, J. Marzec², V. Myalkovskiy¹, L. Naumann³, A. Pilar¹, A. Savenkov¹, A. Shutov¹, I. Slepnev¹, V. Slepnev¹, P. Wintz⁴, K. Zaremba², and I. Zhukov¹

¹JINR Dubna, Russia; ²University of Technology, Warsaw, Poland; ³FZ Dresden-Rossendorf, Germany; ⁴FZ Jülich, Germany

A new development of multiple anode straw tube detectors for CBM has been reported in [1, 2, 3]. A large prototype was prepared to study the technological problems of highly segmented straw arrays and to develop the necessary technology for mass production. Each layer of the prototype contains 48 straws of 40 cm length and 4 mm diameter. The anode wires of the two outer straws are not segmented for calibration purposes. The anodes of all embedded straws are divided into four 10 cm long segments. The granularity of the 10 cm long segments amounts to 4 cm². The inefficient area between two neighbouring anodes in a straw is less than 0.35 cm². The full detector array consists of two layers with 96 straws, divided into 360 anodes. A test of all channels in this straw tube array has been done with collimated γ (⁵⁵Fe). The straws are supplied with Ar/CO₂ (80/20). Transmission lines of 50 cm length have been manufactured for HV supply and signal read-out. Each line is used for two adjacent straws. The HV is distributed by motherboards via resistors to the anodes. The detector signals are coupled by capacitors into preamplifiers. In a first measurement we fixed the gas gain. The gas amplification for unsegmented straws increases from 10³ up to 10⁵ in the HV range from 1.1 to 1.5 kV. The readout is placed near to one end of the straw array and its signal wire density amounts to 1 channel/mm. The signal transmission quality assessment for all 360 anodes has been measured at a gas gain of 10⁴ (1.3 kV) in the middle of the plateau in Fig. 2. The anode signals have been preamplified in the module MSD-25240 with a high gain of 35 mV/ μ A, a fast risetime of 3 ns, an input impedance of 120 Ω and a bandwidth of 35 MHz. An assessment of the functionality of the signal transmission lines shows the distribution of the signal amplitudes in Fig 1. The signals for 94% of the channels are satisfactorily ($\sigma \approx \pm 7\%$). An improvement of the transmission line technology is demanded because 6% of the channels fail. After signal amplification and shaping the LVDS signals are fed in a new Multichannel-TDC with 64 channels, a 100 ps time-stamping module and a PCI-express interface. The MTDC handle multiple-pulses in each channel. The double-pulse resolution amounts to 5 ns. There is a dedicated channel for start-stop mode measurements. The MTDC contains the following trigger modes: external, internal and logic OR on all inputs. In external trigger mode the device measures the pulses that have an arrival time in a defined range relative to the trigger signal.

In internal trigger mode any input pulse starts the measurement. The memory of the MTDC allows the registration of signals which are delayed by 100 μ s to the trigger pulse. This time range is programmable in steps of 25 ns. The internal test mode was used for counting rate measurements in dependence on HV for the straw tubes. The obtained working characteristics is shown in Fig. 2. The pronounced broad and flat plateau demonstrate the perfect behaviour of the straws.

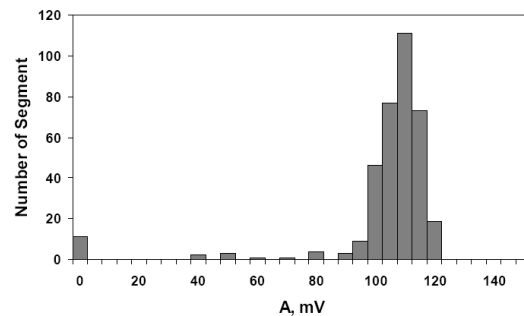


Figure 1: For quality assessment signal amplitudes of all 360 connection lines have been measured. 22 cables deliver no or to small signals.

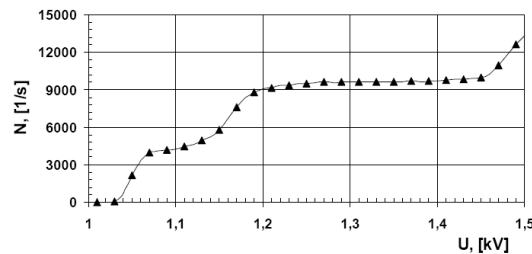


Figure 2: Dependence of the counting rate on the applied HV.

References

- [1] K. Davkov et al., Nucl. Instr. and Meth. A584 (2008) 285
- [2] K. Davkov et al., CBM Progress Report 2007, (2008) 42
- [3] S. E. Vasilyev et al., Instr. and Exp. Techniq., V. 51, No. 6 (2008) 820

* Work supported by EU, INTAS 06-100012-8729.

Layout study of the TRD in the CBM experiment

V. Ivanov¹, A. Lebedev^{1,2}, S. Lebedev^{*1,2}, and G. Ososkov¹

¹JINR LIT, Dubna, Russia; ²GSI, Darmstadt, Germany

First results of a TRD layout study with respect to track reconstruction efficiency, electron identification, and pion suppression performance are presented.

Several new TRD geometries were proposed for the study. The standard TRD geometry in CBM consists of 12 layers grouped in 3 stations (4-4-4 geometry). This layout was compared with geometries with a reduced number of layers: a) excluding one and two layers in each station (3-3-3 and 2-2-2 geometries), b) excluding one and two layers in the second and the third stations (4-3-3 and 4-2-2 geometries).

The LIT track reconstruction algorithm [1] was used for the track reconstruction in the TRD. It uses either tracks reconstructed in the STS as initial seeds (STS based approach) or a standalone approach, using only TRD information. In the STS, the L1 CA track reconstruction algorithm was applied [2].

The track reconstruction efficiencies for central UrQMD Au+Au collisions at 25 AGeV beam energy using the STS-based TRD tracking are given in Table 1. We conclude that the track reconstruction efficiency is almost the same for all considered TRD geometries.

Table 1: TRD track finding efficiency for different TRD geometries in % (STS based approach): All - tracks which pass through all TRD layers; Vertex - tracks from the primary vertex; Ghosts - wrongly found tracks

Geometry	2-2-2	3-3-3	4-4-4	4-2-2	4-3-3
All	95.7	95.2	95.5	95.5	95.5
Vertex	95.9	95.4	95.6	95.7	95.7
Ghost	5.8	5.2	3.7	4.1	3.2

Only three variants of the TRD geometry using the standalone track finder were tested, because it requires at least 4 hits in the first TRD station. The results are presented in Table 2. Again, this algorithm provides comparable efficiencies for all tested geometries.

Table 2: TRD track finding efficiency in % for different TRD geometries using the standalone TRD tracking

Geometry	4-4-4	4-2-2	4-3-3
All	89.1	88.8	88.9
Vertex	94.3	94.6	94.3
Ghost	6.2	7.1	5.9

*s.lebedev@gsi.de

In order to choose the optimal TRD geometry, it is also necessary to investigate the electron identification efficiency and the pion suppression level. The results presented in this report were obtained for electrons and pions from the primary vertex with an initial momentum of 1.5 GeV/c. Moreover, in order to suppress secondary electrons, only particles with momenta larger than 0.5 GeV/c in the first TRD layer were selected. The investigated TRD detector geometry is based on single gas gaps of 6 mm thickness with a 80% Xe and 20% CO₂ gas mixture.

An algorithm based on an artificial neural network (ANN) was used for the electron identification in TRD [3]. The multilayer perceptron (MLP) from the ROOT package was used as ANN. The MLP architecture consists of 3 layers: n input neurons (corresponding to the number of TRD layers), $2n$ neurons in the hidden layer, and one output neuron.

Cuts on the output value of the trained ANN were chosen to provide a 90% electron identification efficiency. Results of the pion suppression in dependence on the number of TRD layers are shown in Table 3. The pion suppression is defined here as the number of pions identified as electrons in the TRD divided by the number of pions in the TRD acceptance. A satisfactory pion suppression level (about 100) can be reached already with 9 TRD layers.

Table 3: Pion suppression for different number of layers in the TRD assuming 90% electron identification efficiency

No. layers	12	11	10	9	8	7	6
Pion suppr.	318	250	148	94	57	34	23

Taking into account the track reconstruction efficiency and the pion suppression level, we conclude that the optimized geometry consists of 4 layers in the first station and 3 layers in the following stations (4-3-3). However, in a next step the detector inefficiency has to be included, and a safety factor of at least 2 should be kept. For these conditions, the minimal number of TRD layers is more likely to be 11.

References

- [1] A. Lebedev, G. Ososkov, *Event Reconstruction in the CBM TRD*, CBM-SOFT-note 2008-001, Darmstadt, 2008
- [2] I. Kisel, Nucl. Instr. Meth. Phys. Res. A 566 (2006) 85
- [3] E. Akishina et al., *Electron/pion identification in the CBM TRD using a multilayer perceptron*, JINR Communications, E10-2007-17, Dubna, 2007

The rate challenges of the CBM-TRD

D. Gonzalez-Diaz¹, A. Andronic¹, A. Battiato¹, C. Garabatos¹, A. Kalweit¹, and F. Uhlig¹
¹GSI, Darmstadt, Germany

J/Ψ and Ψ' trigger and detection in the di-electron decay channel with the CBM experiment requires a π suppression of 100 and a position resolution better than $300 \mu\text{m}$ at particle fluxes of 100 kHz/cm^2 . A TR detector based on MWPCs with Xe/CO₂ gas appears to be suited for the task, as it was proved in a series of works [1], [2], [3]. Through a complementary effort consisting of an analytical study substantiated by a series of systematic measurements, we have looked into the practical limits of the MWPC technology for TR detection, regarding both the maximum operating gain and particle flux (details in [4], [5], [6]).

A maximum working gain of $m_o = 3 \times 10^5$ was determined for Xe/CO₂ mixtures both in chambers with $s = 3$ and 4 mm anode wire pitch, being independent from the fraction of quencher. This behaviour is suggestive of a major role of electron feed-back from ion collisions with the cathodes. At the above-mentioned gain, operation was halted due to a form of self-sustained discharge, being the chamber performances recovered after a power cycle. Since gains $m_o = 5 \times 10^3 - 10^4$ have been proved to be sufficient for high efficiency and energy resolution [3], a safety factor of 30-60 in the initial charge (for dealing with nuclear fragments or highly ionizing secondaries) is assured.

Another aspect that was scrutinized in detail due to the existence of analytical methods was the rate capability of the device under different conditions, of which we focus on the Xenon mixtures. To start with, the Mathieson model [7] together with the Blanc's law for ion mobilities was used. A correction due to finite beam effects is important (up to a factor 10 in the estimated rate capability) when the beam and the chamber typical dimensions are comparable. So, this effect was studied in detail and indeed a remarkable agreement with the analytical behaviour of the correction factor d_m [8] was found for a series of measurements at different beam sizes. In order to extrapolate the measurements to the behaviour under minimum ionizing particles (mips) irradiation we took as reference the measured values for the energy loss in Xe/CO₂ mixtures [9]. By defining the rate capability at 10% gain drop and $m_o = 10^4$ as the figure of merit of a MWPC, we found a convenient representation by plotting it as a function of the fraction of quencher and chamber pitch, shown in Fig. 1. The lines correspond to the Mathieson model when the existing values for the mobility of CO₂⁺ in the primary gas components are used (no free parameter). The absorption probability for characteristic TR photons is also depicted on the right y-axis. In particular, previous measurements from [3] can be accurately described by the same model [6].

Under reasonable assumptions (see [6]) the most critical dependence of the rate capability with the chamber gap ($\propto 1/h^3$) can be shown in a single picture (Fig. 2), where

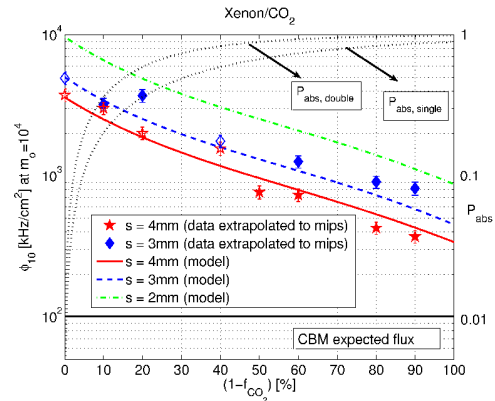


Figure 1: Rate capability (data and model) for mips at 10% gain drop (ϕ_{10}) and $m_o = 10^4$.

the shadowed area indicates the region of gap sizes where a MWPC could fulfill the CBM requirements in terms of rate capability and X-ray absorption probability. This study confirms that the value chosen for the prototypes ($h = 3$ mm) is indeed a very good choice.

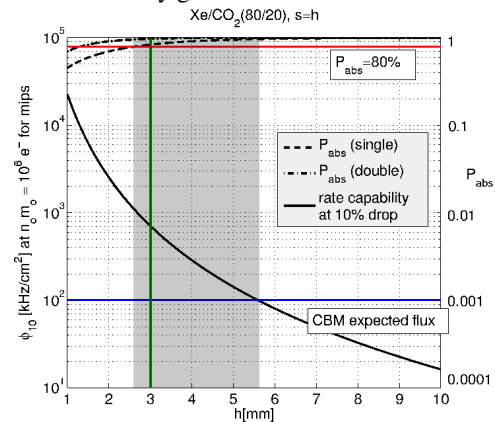


Figure 2: Rate capability and TR absorption probability vs the chamber gap h . The shadowed area is the region where a chamber would be well suited for the TRD of CBM.

References

- [1] A. Andronic NIM A, 563(2006)349.
- [2] M. Klein-Bosing et al., NIM A, 585(2008)83.
- [3] M. Petris et al., NIM A, 581(2007)406.
- [4] C. Garabatos et al., GSI report(2006), INSTR-METH-41
- [5] D. Gonzalez-Diaz, GSI report(2007), FAIR-EXP-21.
- [6] D. Gonzalez-Diaz et al., to be submitted to NIM A.
- [7] E. Mathieson, NIM A, 249(1986)413.
- [8] G.C.Smith, E. Mathieson, IEEE, TNS 34-1(1987)411.
- [9] A. Andronic et al., NIMA A, 525(2004)447.

Research and development of fast gas detectors for CBM experiment

S. Chernenko, G. Cheremukhina, S. Chepurinov, D. Donetz, S. Razin, Yu. Zanevsky, and V. Zryuev
JINR, Dubna, Russia

R&D for several types of fast gas position sensitive detectors for CBM experiment is being performed at JINR to study rate capability, spatial resolution and operational stability.

a) The R&D on MWPCs for fast a TRD was carried out by a collaboration of GSI, JINR, NIPNE and Münster University. A rate capability of 400 kHz/cm^2 was obtained for a chamber of $10 \times 10 \text{ cm}^2$, 6 mm thickness, $20 \mu\text{m}$ anode wires, 2 mm pitch with pad readout [1]. One of the main advantages of this detector is the high reliability. The TRD detector based on this MWPC combined with a RICH can provide the required pion suppression of $\sim 10^{-4}$ [2] for CBM.

b) Two-stage GEM detector with a sensitive area of $10 \times 10 \text{ cm}^2$ has been design and tested. The test of the detector with one dimensional readout board (pitch of strips were 1.0 mm, 0.6 mm and 0.35 mm) was performed in laboratory conditions with X-ray tube (copper cathode). The drift and induction gaps of detector are 10 mm and 2 mm, respectively. It was operated with an Ar/CO_2 (85/15) gas mixture and an amplification factor of $\sim 2 \times 10^3$ [3]. The best spatial resolution of $60 \mu\text{m}$ was obtained with strips of 0.35 mm (fig.1).

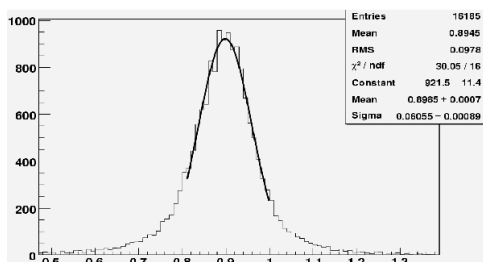


Figure 1: Spatial resolution of $60 \mu\text{m}$ obtained for 2-stage GEM detector with fine collimated X-ray beam.

c) The THGEM of $10 \times 10 \text{ cm}^2$ was manufactured by standard PCB technique of precise drilling in G-10, 0.4 mm thickness, hole diameter 0.3 mm, distance between the holes 0.7 mm and rims 0.1 mm. On the base of this THGEM of $10 \times 10 \text{ cm}^2$ a gaseous detector was constructed and tested with the same conditions as the 2-stage GEM detector. The gas amplification factor was $\sim 2 \times 10^3$ (the maximal gas amplification factor was $\sim 5 \times 10^3$). A spatial resolution of $\sim 250 \mu\text{m}$ was obtained. One of the main problems for THGEM is sparking. A spark takes place in holes with a “poor”, displaced rim, see fig.2.

All mentioned above detectors were tested with FEE based on the 16-channel ASIC preamplifier/shaper (PASA) designed in $0.25 \mu\text{m}$ CMOS technology [4]. We have also

designed a card for strip/pad readout consisting of 16-channel PASA, sampling ADC (MAXIM 1434/50MSPS) and Spartan-3 FPGA. Data output transfer is arranged via USB interface.

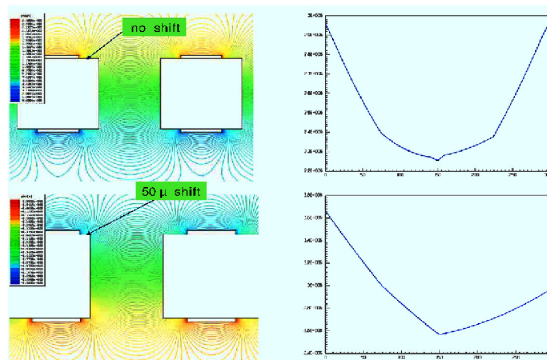


Figure 2: Electrical field map at THGEM calculated by MAXWELL for “0” shift (hole is good centered) and $50 \mu\text{m}$ shift.

d) Additionally a 3-stage GEM detector of $10 \times 10 \text{ cm}^2$ with two dimensional readout board (fig.3) is under construction at JINR. Pitch of this 2D readout board is $800 \mu\text{m}$ (X and Y). Readout electronics will be designed on the base of CBM-XYTER chip in collaboration with GSI.

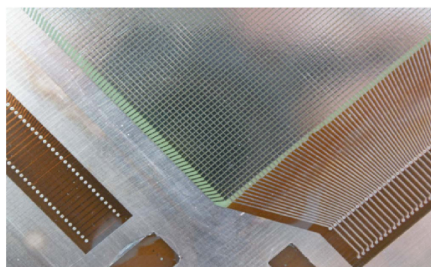


Figure 3: 2D readout board.

References

- [1] A. Andronic et al., “Electron/pion identification with fast TRD prototypes”, GSI Annual Report, 2006.
- [2] V. Friese, “The CBM Experiment at FAIR”, Report on the CPOD Workshop, GSI, 13 July 2007.
- [3] S. Chernenko et al., “Research and Development of fast readout chamber based on GEM structures”, CBM Progress Report 2007, 38.
- [4] H.K. Soltveit et al., “Fast TRD Pre-Amplifier Sahper for the CBM experiment”, GSI Annual Report 2005, 72.

Low resistivity materials for the low polar angle of the CBM-TOF wall

L.A. Diaz¹, J. A. Garzon², D. Gonzalez-Diaz³, L.Lopes⁴, M. Morales², and C. Pecharroman⁵

¹CINN-CSIC, Oviedo, Spain; ²USC, Santiago, Spain; ³GSI, Darmstadt, Germany; ⁴LIP, Coimbra, Portugal; ⁵ICMM-CSIC, Madrid, Spain

Avalanches in timing RPCs release an average charge $\bar{q} \simeq 1.5 - 3$ pC per gap, slightly depending on the geometry, gas and field [1]. An RPC must be therefore able to evacuate the charge from the system at a rate $1/\tau$ comparable to the avalanche rate r (τ is the relaxation time of the resistive material). The dependence with r can be evaluated after the initial transitory phase by resorting to the Ohm law in electrostatic equilibrium (DC situation):

$$V_{gap} = V - IR = V - \bar{q}rR = V - \bar{q}\phi\rho d \quad (1)$$

with ϕ being the avalanche flux and d the resistive plate thickness per gap. For 1 mm thin float glass tRPCs ($\rho_{20} \simeq 6000$ G Ω cm [2] with one order of magnitude decrease in 25 K [3]) a voltage drop of nearly 1-2 volts/Hz/cm² can be inferred at ambient T. This is the reason why float glass tRPCs work only up to some 100's Hz/cm². In practice, operation up to almost 500 Hz/cm² was proved with a defocused beam in stationary (DC) conditions [4] and even up to 1000 Hz/cm² but in the transitory region [5] (short spills). Eq. 1 can be re-expressed as a function of the relevant time scales and the ratio of the nominal voltage to the voltage drop created by each individual avalanche V_{aval} :

$$r\tau \ll \frac{V}{V_{aval}} \quad (2)$$

and a simple derivation based on eq. 1 shows that in first order the rate capability of an RPC can be expressed as [6]:

$$\phi_{max} \propto \frac{\bar{q}}{\rho d} \quad (3)$$

so one can linearly increase the rate capability of the chamber by decreasing ρ and/or d . The 20 kHz/cm² at the low polar angle region of the CBM-TOF wall therefore impose a 20/40-fold decrease with respect to float glass for any of these variables, of which ρ is the more natural candidate.

Modelling the material as a simple RC circuit, the transitory regime prior to the aforementioned DC situation can be characterized by a transient time t_{eq} given by [7]:

$$t_{eq} \simeq \frac{\tau}{d\bar{q}/dV\phi\rho d} \ln(1 + d\bar{q}/dV\phi\rho d) \quad (4)$$

Nonetheless, a realistic description requires to implement via MC the material response function $\Psi(t)$. Fig. 1 shows the accuracy of such an approach at describing the transients in \bar{q} ($I \propto \bar{q}$) arising from X-ray illumination [2].

The high CBM rates pose new questions regarding ageing. Taking a working time equivalent to 5 years operation at 50% duty cycle, a density of total transported charge $Q/A \simeq 1.5-3$ C/cm² must be furnished. While low ageing for $Q/A = 20$ mC/cm² has been proved for glass tRPCs over 2 years operation [8], the almost 100-fold increase for

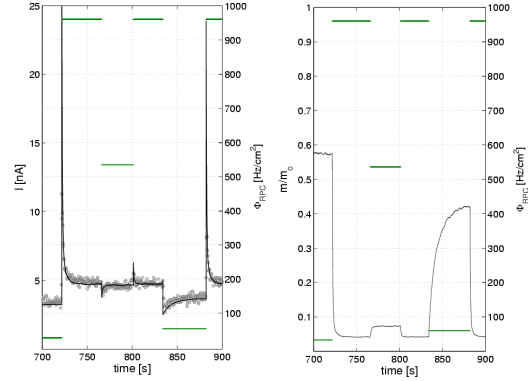


Figure 1: Left: Transients in the measured current (the flux steps are indicated on the right axis). Right: behaviour of \bar{q} in adimensional units as obtained from the model.

CBM requires of similar studies yet. In particular, the material itself should keep the integrity of its electrical properties for such a high Q/A and total dose.

Through a collaboration USC/CSIC/GSI we recently started an effort to produce low resistive materials able to withstand the required amount of transported charge. Four samples of a ceramic-metal composite were produced via the novel SPS technique for different metal concentration f close to the percolation limit f_c , where the electrical properties of the composite roughly scale like:

$$\rho = \rho_{cer}(f_c - f)^p \quad \epsilon = \epsilon_o(f_c - f)^{-q} \quad (5)$$

In particular, the 88/12 (ceramic/metal) sample, with 2 cm diameter and 3 mm thickness, showed $\rho_{20} = 25$ G Ω cm and $\epsilon_{r,\infty} = 32$, with a breakdown field higher than 3 kV/cm and just a small degradation of the resistivity for $Q/A = 20$ mC/cm² (attributed to the experimental setup). We plan to build chambers with the different samples soon in order to explore the typical CBM rates and higher.

References

- [1] P. Fonte, V. Peskov, NIM A, 477(2002)17.
- [2] D. Gonzalez-Diaz et al., doi:10.1016/j.nima.2008.12.097.
- [3] D. Gonzalez-Diaz et al., NIM A. 555(2005)72.
- [4] H. Alvarez-Pol et al., NIM A. 535(2004)277.
- [5] A. Akindinov et al., NIM A. 533(2004)74.
- [6] D. Gonzalez-Diaz et al., GSI Report(2007), FAIR-EXP-09.
- [7] D. Gonzalez-Diaz et al., Nucl. Phys. B(Proc. Suppl.), 158(2006)111.
- [8] S. Gramacho et al., doi:10.1016/j.nima.2008.12.133.
- [9] A. L. Efron et al., Phys. Status Solidi B 76(1976)475.

Cross-talk studies oriented to stripped tRPCs at high multiplicities

A. Berezutskiy¹, M. Ciobanu², D. Gonzalez-Diaz², I. Deppner³, and A. Gil⁴

¹SPbSTU, St Petersburg, Russia; ²GSI, Darmstadt, Germany; ³PI, Heidelberg, Germany; ⁴IFIC-CSIC, Valencia, Spain

The presence of large cross-talk in meter-long stripped timing RPCs was recognized experimentally time ago [1]. Understanding its practical importance is, however, far from easy. To start with the origin of cross-talk is capacitive, so no net charge is transported when integrating over a time span sufficiently long. Because of that, in low-multiplicity environments even in the case where cross-talk would travel throughout the whole detector making several strips firing at once, such events could be discarded off-line on the basis of having null charge [2]. A different effect, to be distinguished, will be called 'charge sharing' in the following and arises from the induction onto several strips during the avalanche formation ([3], for instance). However, as long as the transverse dimension of the strip is much bigger than the avalanche size, and the inter-strip gap is large, this process will have generally less impact than cross-talk, and will be omitted here for shortness.

On the other hand, cross-talk is 'a priori' a concern for any stripped tRPC aimed at operating at high multiplicities. The practical influence on the detector performances will depend on the time distribution of the impinging particles, the inter-strip capacitance C_i , the impedance of the line Z_o (that rules the time duration of the cross-talk and the signal itself) and very critically on the detector length L , signal rise-time t_{rise} and FEE threshold v_{th} . A simplified picture can be drawn under some assumptions [4] where the contribution to the resolution due to baseline oscillations originated from cross-talk (rms_{ct}) can be sketched as:

$$rms_{ct} \simeq \frac{\bar{v}}{v_{th}} \left(\frac{rms_v}{\bar{v}} \right) \frac{t_{rise}}{\ln 9} F(L, C_i, t_{rise}) \quad (1)$$

being \bar{v} the average signal amplitude and F the fraction of cross-talk that depends on L , C_i and t_{rise} . Taking usual values ($\frac{\bar{v}}{v_{th}} \simeq 5-10$, $\frac{rms_v}{\bar{v}} \simeq 1$, $t_{rise} \simeq 200ps$), the jitter arising from 10% cross-talk from an adjacent cell would be $\sim 100ps$, that would add quadratically to the resolution of the interesting event (of the same order, in tRPCs).

The detector design task is much simplified if analytical or numerical tools are available, so that the very broad phase-space can be explored without need to build an exhaustive amount of prototypes. The main difficulty in HF simulation arises from non-perfect grounds, impedance steps at connectors and non-perfect soldering points. So, we built an 'electrically equivalent' of an RPC (without glass, for simplicity) and with an impedance close to $Z_o = 50\Omega$ trying to minimize those effects. The 'RPC' consisted of 3 equal electrode planes with air in between and segmented into 2.2cm strips (with 0.3cm separation) placed inside a metallic box (see [4] for details). The outer electrodes were joined and all ports terminated by 50Ω resistors, emulating a pseudo-differential read-out. For the elec-

trical simulation we used the APLAC software. Simulation was checked for signals with t_{rise} 10ns, 1ns and 0.36ns of which here the 1 ns are shown (Fig. 1), illustrating the good agreement. The induction after injection in (i) the central electrode (left-up) is shown for (ii) the outer one (right-up), (iii) the central one of the adjacent strip (left-down) and (iv) the corresponding outer one (right-down).

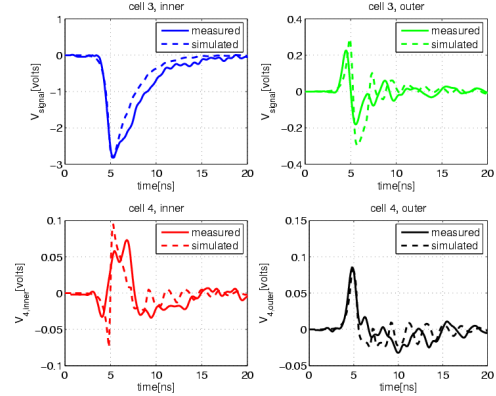


Figure 1: Induction in different strips when signal is injected in the central electrode (up-left).

The general propagation behaviour is presented in Fig. 2 when 200ps rise-time differential signals were simulated in a typical 8-gap glass-tRPC with 2.2cm strip width and 0.3cm gap. Clearly, if a cross-talk above 10% is to be avoided, the detector length must be considered critically. A comprehensive description of all the available data is in progress and will be subject of an internal CBM note.

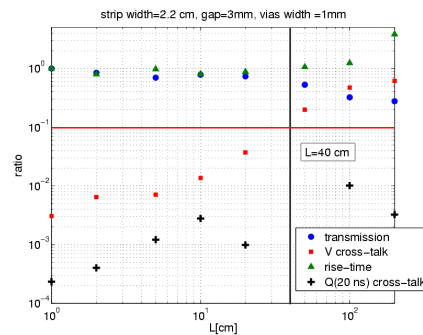


Figure 2: Transmission coefficient, cross-talk fraction, t_{rise} deterioration and cross-talk charge in 20ns as a function of the detector length L for signals with $t_{rise}=200$ ps.

References

- [1] A. Blanco et al., NIM A 485(2002)328.
- [2] D. Belver et al., doi:10.1016/j.nima.2008.12.090.
- [3] N. Majumdar et al., NIM A 595(2008)346.
- [4] D. Gonzalez-Diaz, talk at XII CBM coll. meeting (2008).

Progress for high rate glass tRPCs with pads

V. Ammosov¹, V. Gapienko¹, A. Golovin¹, F. Guber², A. Semak¹, Yu. Sviridov¹, E. Usenko², and V. Zaets¹

¹IHEP, Protvino, Russia; ²INR, Moscow, Russia

The Time-of-Flight (TOF) system of the CBM experiment is proposed to be based on timing Resistive Plate Chambers (tRPC). The TOF system should have a time resolution of about 80 ps with almost 100% detection efficiency. For the inner part of the TOF wall a rate capability of up to 20 kHz/cm² is needed and the cell size should be not larger than 4 cm² to keep a low occupancy (< 5%).

The tRPCs are usually multi-gap chambers with glass as resistive plates operated in the saturated avalanche mode. At present, detectors using conventional glass plates with $\sim 10^{12}$ Ohm-cm bulk resistivity and 0.5-1 mm thickness have a limited rate capability of about several hundred Hz/cm². It is expected that the tRPC rate capability can be increased by decreasing the bulk resistivity of glass plates or/and decreasing its thickness.

Previously, development of semi-conductive glass production to obtain glass samples with a resistivity in the range $10^8 - 10^{11}$ Ohm-cm for phosphate and silicate compositions was done. Prototypes of four gap tRPCs with phosphate and silicate glass plates of 2 mm thickness were tested with beams, efficiency beyond 95% and roughly constant time resolution of 100 ps were found at flux densities of up to 20 kHz/cm² [1]. However the prototypes did not show long-term stability - some increase of dark current through the chambers was observed after first irradiations. Furthermore, the production of special glasses is semi-industrial, glass properties are not stable enough and the cost is too high.

Therefore an attempt has been made to increase the tRPC rate capability by decreasing glass plate thickness. Three chambers were constructed and tested with beam at the IHEP U-70 accelerator. Two chambers had single a 0.3 mm gap with 0.17 and 0.85 mm thick glass plates. A third chamber produced from 0.17 mm glass plates had 6×0.3 mm gaps. Lateral sizes of glasses were 24×24 mm² with outer read out pads of 18×18 mm². The 0.17 mm glass plates were usual microscope cover slips, the 0.85 mm glass was from Glaverbel firm. Both types of glass have a bulk resistivity of about 10^{12} Ohm-cm. During beam tests the counting rate for the chambers was provided by irradiation with a ⁹⁰Sr source.

Figures 1 and 2 show efficiency and time resolution for the chambers as a function of counting rate. The efficiency of the 0.85 mm single gap tRPC drops after 200 Hz/cm², but for the 0.17 mm single gap chamber efficiency stays constant up to 2 kHz/cm². The six gap tRPC with 0.17 mm glass has a constant efficiency up to 6 kHz/cm².

The time resolution for both 0.17 mm tRPCs becomes worse at a rate of ~ 2 kHz/cm². This rate value is by one order of magnitude higher than for the 0.85 mm single gap

tRPC at constant level of time resolution. This first experimental observation confirms the expectation. It is surprising that we did not observe the improvement of time resolution for the six gap chamber compared with single gap one even at low rates. Noise was not higher than a few Hz/cm² and dark current was less than 1 μ A for all chambers.

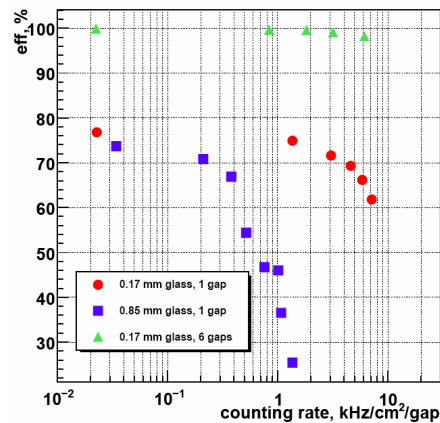


Figure 1: Efficiency of tRPCs as a function of counting rate at HV=3 kV/gap.

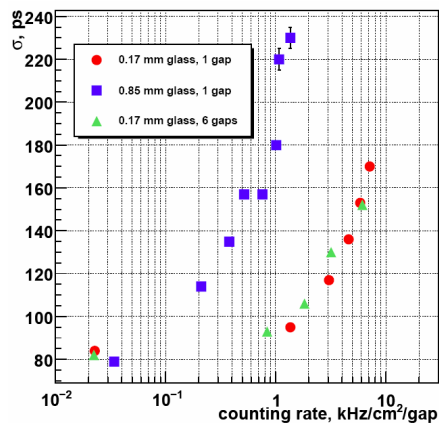


Figure 2: Time resolution of tRPCs as a function of counting rate at HV=3 kV/gap.

It can be concluded that decreasing of glass plate thickness indeed increases the high rate capability of tRPCs. We plan to use thinner glass plates for tRPCs to reach constant time resolution up to higher rates. This work was supported partially by INTAS 06-1000012-8810 project.

References

- [1] V.Ammosov et al., Nucl.Instr.Meth. A576(2007)331

In-beam test results of the Pestov Glass Resistive Plate Counter prototypes *

D. Bartos¹, G. Caragheorghopol¹, F. Dohrmann², K.D. Hildenbrand³, B. Kaempfer², R. Kotte², L. Naumann², M. Petriş¹, M. Petrovici¹, V. Simion¹, D. Stach², C. Williams⁴, and J. Wuestenfeld²

¹NIPNE, Bucharest, Romania; ²FZ Dresden - Rossendorf, Dresden, Germany; ³GSI, Darmstadt, Germany; ⁴CERN, Geneva, Switzerland

The Compressed Baryonic Matter (CBM) experiment foresees a time-of-flight (TOF) wall equipped with resistive plate chambers (RPC) 10 m downstream from the target. The inner part of the TOF covers 50-100 mrad around the beam axis with an estimated flux densities of charged particles up to 20 kHz/cm². The rate capability of the present RPC based on commercial float glass ($\sim 10^{12}\Omega\cdot\text{cm}$) as electrodes is limited at about 1 kHz/cm².

We designed and built two new prototypes of multi-gap, multi-strip RPCs based on Pestov glass of $10^{10}\Omega\cdot\text{cm}$ bulk resistivity: one with standard readout - single-ended and the other one with differential readout.

The experiment has been performed at the electron linac ELBE at the Forschungszentrum Dresden-Rossendorf following the procedure described in [1]. Results of the in-beam tests of these two prototypes are presented below.

In the first part of the measurements a standard multistrip - multigap RPC architecture [2, 3], based on Pestov glass [4], was used. The counter was operated at 5.8 kV using standard gas mixture (85% C₂H₂F₄+5% iso-C₄H₁₀+10% SF₆). The signals of four strips read-out at both sides have been recorded. For the signal amplification we used the first generation of a fast amplifier/discriminator (called FEE1) developed for FOPI RPCs at GSI [5] providing both timing and charge information for each channel. The time of flight distribution, for each measured strip, was obtained as the mean of the time information at both ends ($t_{\text{left}} + t_{\text{right}}/2$). The obtained time resolutions, after walk correc-

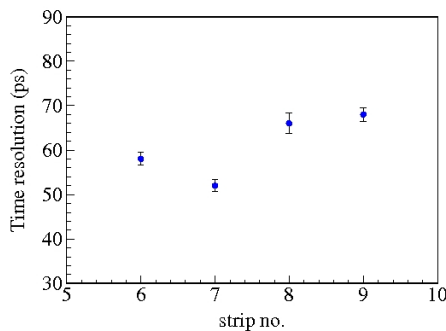


Figure 1: Time resolution of four neighbouring strips.

tion and selection of the events with the maximum charge on the analyzed strip, for the four measured strips, can be followed in Fig. 1. The observed variation of the time resolution for different strips quite probable is due to different

intrinsic resolution of the corresponding electronic channels.

It should be stressed that these results have been obtained under a uniform illumination of the counter at a particle flux density of 1 kHz/cm² in contrast with tests performed with collimated MIP hadron beams when only a small part of the active area is exposed.

A second prototype that was tested is the four gaps Pestov glass RPC with a differential readout architecture. The applied voltage was 5.45 kV for all the performed measurements. An 8-channel differential amplifier/discriminator based on NINO ASIC chip, developed within the ALICE Collaboration [6], provided the timing information and the time over threshold as a measure of the input charge for slewing correction. Due to the limitation of the available electronic channels of the DAQ system, the signals of only two strips, readout at both ends, were recorded. The results obtained for time resolution at

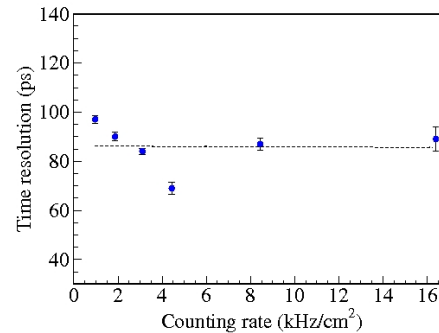


Figure 2: Time resolution as a function of counting rate.

different counting rate can be followed in Fig.2. Hardly any degradation of the time resolution up to about 16 kHz/cm² was observed. The larger value of the time resolution obtained for lowest rates can be due to some temperature instabilities during longer acquisition times needed at lower rates.

References

- [1] R. Kotte et al. Nucl. Instr. and Meth. A 564(2006), 155.
- [2] M. Petrovici et al., Nucl. Instr. And Meth. A 487(2002), 337.
- [3] M. Petrovici et al., Nucl. Instr. And Meth. A 508(2003), 75.
- [4] M. Petrovici et al., CBM Progress Report 2006, 43
- [5] M. Ciobanu et al., IEEE Trans. on Nucl. Science, Vol.54, Issue 4 (2007), 1201.
- [6] F. Anghinolfi et al., Nucl. Instr. And Meth. A 533(2004), 183

* Work supported by EU-FP6 (see annex) and CORINT/EU-RO contract no.58 financed by Romanian NASR and BMBF contract 06 DR 135.

Characterisation of FOPI narrow strip RPCs

I. Deppner¹, N. Herrmann¹, R. Averbeck², C. Ciobanu^{1,2}, K.D. Hildenbrand², T.I. Kang², M. Kiš², Y. Leifels², K. Piasecki¹, A. Schüttauf², D. Gonzalez Diaz², and the FOPI Collaboration²

¹Physikalisches Institut, Uni Heidelberg, Germany; ²GSI, Darmstadt, Germany

Multi-gap Multi-strip Resistive Plate Counters (MMRPCs) are one of the key components of the CBM-TOF System. To learn about characteristic features and performance of this type of new detector, data are analyzed that were obtained with the FOPI narrow strip MMRPC in a data taking run studying the reaction Ni + Ni at an incident energy of 1.91 AGeV at the SIS 18 accelerator.

The FOPI MMRPC system consists of 30 super modules, each housing 5 RPCs. The counters have a 16-strip anode with a strip width of 1.64 mm and length of 90 cm. The gap between the strips is about 0.9 mm. For a review on the construction principles see [1,2,3]. The MMRPCs were operated at a high voltage of 9.6 kV and a gas mixture of R-134a/SF₆/iso-butan (80:15:5). An overall system time resolution below 95 ps has been achieved for the data set discussed here [4].

Figure 1 shows the charge distribution of the individual clusters as a function of $\beta\gamma$ within the range $0.5 < \beta\gamma < 5$. We observe a correlation of the mean charge of the detected RPC-hit with the energy deposition of the particle that depend only on $\beta\gamma$ (Bethe-Bloch).

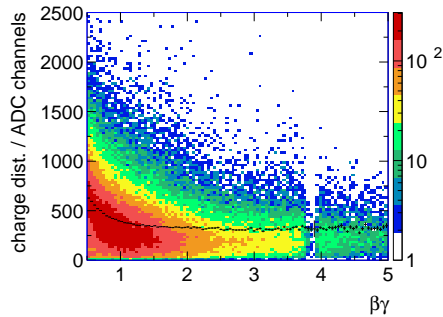


Figure 1: cluster charge distribution vs. $\beta\gamma$

The distribution of the mean charge of a cluster over all 16 strips of the RPC can be seen in Fig. 2. The data which are represented by the stars were obtained within the range mentioned above, while the cross like data were obtained with minimum ionizing particles ($\beta\gamma > 2$). In both cases the measured charge drops on the side strips. This is consistent with the fact, that the average size of a cluster is about 4.2 strips in middle of the counter and about 2.1 on the edge, pointing to the fact, that edge effects diminish the electrical field to the extension of about 2 - 3 strips, i.e. 5 - 7 mm, that has to be compared with an anode-cathode distance of 4.5 mm.

Another feature of interest is the intrinsic time spread of a single cluster (Fig. 3). In the center of the counter a

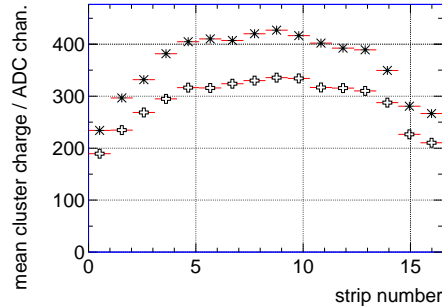


Figure 2: mean cluster charge vs. strip number

RMS value of the contributing timing signals of ≈ 28 ps is observed which correspond approximately to the electronic resolution of the system [1,5]. The degradation towards the sides can be understood by the decreasing signal-to-noise ratio caused by the dropping pulse height as shown in Fig. 2.

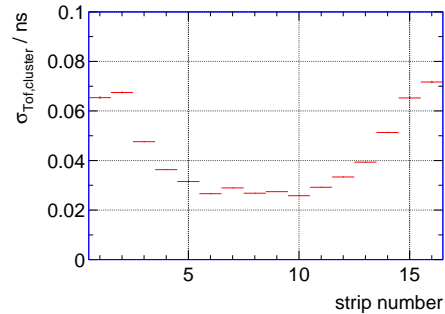


Figure 3: time resolution of single clusters for individual strips

Summarizing first positive experience was gained with the long term operation of a RPC-ToF-barrel. The characteristics measured during the run delivers important data for the planning, construction and operation of RPCs in CBM. Further investigation especially on the multi-hit performance of narrow strip MMRPCs is ongoing.

References

- [1] A. Schuettauf et al., NIM A 533(2004) 65
- [2] A. Schuettauf et al., Nucl. Phys. B 158(2006) 52
- [3] M. Kiš et al, GSI-Report 2007-1.
- [4] T.I. Kang et al, GSI-Report 2008.
- [5] M. Ciobanu et al, IEEE Trans Nucl. Sci. 54(2007) 1201.

Reconstruction of photons and reoptimization of the CBM calorimeter system

S. Belogurov, Yu. Zaitsev, I. Korolko, and M. Prokudin

ITEP, Moscow

Introduction

In 2008, the ITEP calorimeter group has concentrated on two issues:

1. Development of a realistic photon (electron) reconstruction procedure which is efficient in the high-multiplicity environment of the CBM spectrometer.
2. New round of the calorimeter system optimization caused by realistic cost estimation and funding limitations.

Photon reconstruction

The main objective of the CBM calorimeter system is to reconstruct photons, π^0 , and η mesons. This task is rather complicated taking into account the huge multiplicity of particles produced in ion-ion collisions. Rather often, photon-induced clusters in the ECAL are diluted with energy contributions from neighbor particles. At the same time, realistic and efficient reconstruction algorithms are required at early stages of the calorimeter system development for optimization studies. We have developed photon (electron) reconstruction algorithms based on a dedicated 2D fitting of calorimeter clusters with a MC-generated electromagnetic shower library. The procedure starts from determination of all 3×3 clusters (with the hottest central cell) in the ECAL not matched with reconstructed charged tracks. For reconstruction, we select the 2×2 cell matrix with the highest energy deposition and one additional cell (from 5 remaining) with the lowest energy deposition. Photon (electron) energy and impact point are then defined from a fit of the selected 5 calorimeter cells with the shower library by minimization of χ^2 :

$$\chi^2 = \sum_{i=1}^5 \frac{\left(E_i^{meas} - \sum E_i^{pred}(E_\gamma, X_\gamma, Y_\gamma)\right)^2}{\sigma_i^2}, \quad (1)$$

where E_i^{meas} is the energy deposition measured in the i -th cell and $\sum E_i^{pred}(E_\gamma, X_\gamma, Y_\gamma)$ the predicted energy deposition in the i -th cell as a function of energies and impact points of all photons participating in the fit. The error of the cell energy σ_i^2 is defined as

$$\sigma_i^2 = c_2 \times (E_i^{meas}(1 - E_i^{meas}/E^{cluster}) + c_0 + c_1 E^{cluster} \times E^{cluster}), \quad (2)$$

where $E^{cluster}$ is the total cluster energy and E_i^{meas} the energy measured in the i -th cell. This formula allows to

take into account the correlations of the energy depositions in neighboring cells. The independence of χ^2 of the incoming photon energy is guaranteed by the proper choice of the parameters c_0 and c_1 ($c_0, c_1 \ll 1$).

The quality of the reconstruction procedure is demonstrated in Fig. 1, where the ratio of reconstructed ($\chi^2 < 3$) and MC truth photon energy is plotted. The right tail of the distribution is explained by remaining cluster dilution with energy deposition from neighbor tracks (mostly hadrons).

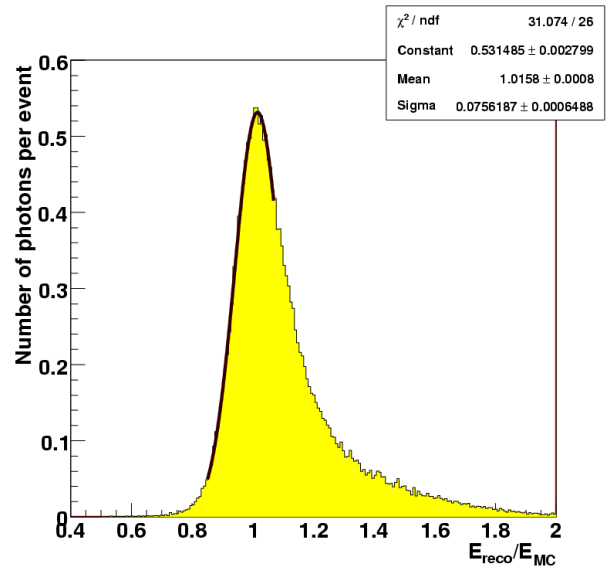


Figure 1: Ratio of reconstructed and MC truth photon energy

Calorimeter system optimization

During the last two years, it became clear that a calorimeter system covering the full CBM acceptance is too expensive and does not fit in the current collaboration budget. Therefore, we performed dedicated optimization studies to understand the optimal way of reducing the detector price while keeping maximal efficiency and θ and p_T coverage for the reconstruction of photons, π^0 and η mesons. We compared three different options for a reduced calorimeter system.

1. “One sector”: A single calorimeter section (up or down) of trapezoidal form.

2. “Two sectors”: Two symmetric calorimeter sections (up and down) of trapezoidal form.
3. “Two blocks”: Two symmetric calorimeter sections (up and down) of rectangular form.

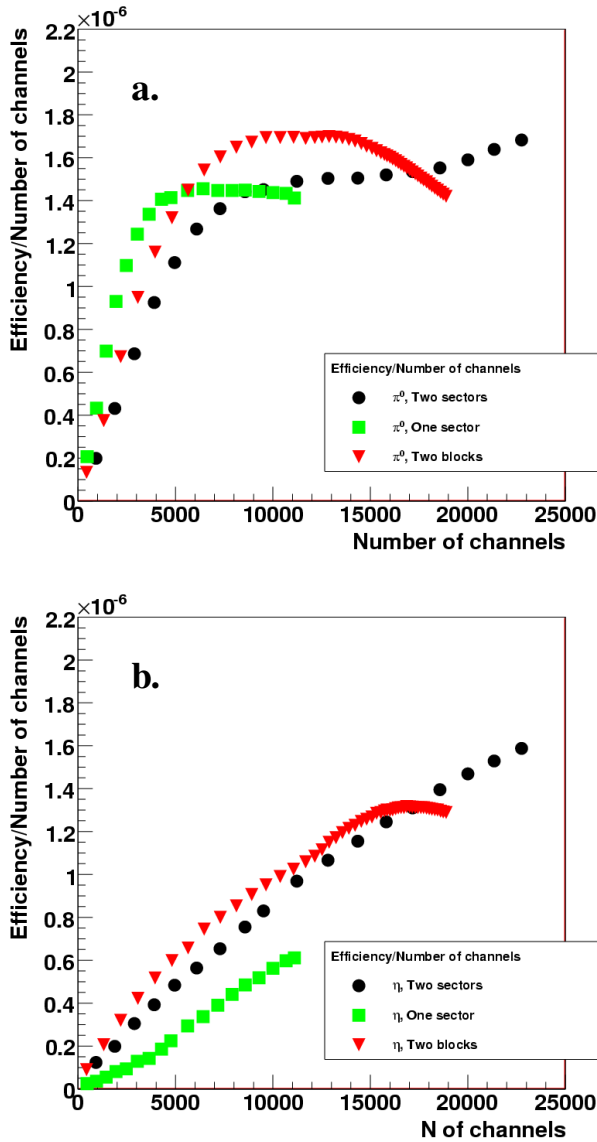


Figure 2: Reconstruction efficiency normalized to the number of calorimeter channels for (a) π^0 mesons and (b) η mesons

The behavior of the efficiency of photon reconstruction is rather trivial — it increases with the calorimeter acceptance. So, we studied the dependence of reconstruction efficiency normalized to the number of ECAL channels for π^0 s and for η mesons as shown in Fig. 2a and Fig. 2b, respectively. The opening angle of photon pairs from π^0 decays is rather small; therefore, the “one sector” solution is better for a very small (less than 5K channels) calorimeter, which is not the case for the massive η mesons. The same

logic explains the advantage of the “two block” calorimeter for π^0 reconstruction. The “usefulness” of each calorimeter cell for π^0 s reaches a maximum for the calorimeter system consisting of ~ 14 K channels. Such a calorimeter was chosen as the new baseline option for the CBM spectrometer (Fig. 3). The support construction allows to move the whole calorimeter right and left for physics studies at larger angles and helping other CBM subsystems to tune the electron identification.

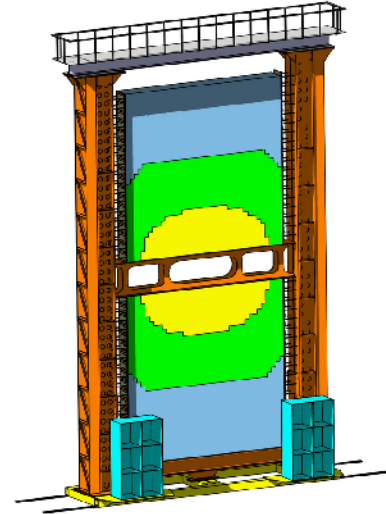


Figure 3: Engineering design of the calorimeter wall

Particle identification in ECAL with longitudinal segmentation

A. Artamonov and Yu. Kharlov

Institute for High Energy Physics, Protvino, 142281 Russia

The performance of the CBM electromagnetic calorimeter (ECAL) with respect to photon identification was studied with the use of longitudinal segmentation of ECAL modules. The longitudinal profile of the electromagnetic shower developed in the ECAL by photons and electrons is well defined, while the ECAL has a relatively small nuclear absorption length ($\lambda/\lambda_I \approx 1$), and thus, hadronic showers have very different longitudinal profiles with large fluctuations. The most simple longitudinal segmentation of ECAL modules consists of two segments with independent measurement of energies deposited in these segments. The optimal division of ECAL modules to two segments is defined through maximizing the signal/background ratio. The photon identification with the 2-segmented calorimeter is compared to that of a calorimeter without longitudinal segmentation.

The Monte-Carlo study of the ECAL was developed within the standard CBM framework for simulation and reconstruction, CBMROOT. The model of the ECAL module consisted of 160 layers of a plastic scintillator of 1.0 mm thickness and a lead absorber of 0.7 mm. The total radiation length of such a calorimeter is $20.4 X_0$; the energy resolution is $\sigma_E/E = 0.066/\sqrt{E} \oplus 0.012$. The module was segmented into 20 equal sections along the z axis, such that the energy deposited in each section was measured separately. Thus, the radiation length of each longitudinal section was about $1X_0$. This fine segmentation allowed to study ECAL modules with 2 longitudinal segments with a step of $1X_0$ by combining energies deposited in the first n sections into the energy E_1 and the energies deposited in the last $20 - n$ sections into the energy E_2 . The optimal segmentation of the 2-segmented module was then found by varying n from 1 to 19.

To do so, single particles such as γ , π^\pm , K_L^0 , p , \bar{p} , n , \bar{n} with momenta from 1 to 25 GeV/c were generated to hit the ECAL module perpendicularly to its front side in the Monte-Carlo simulation.

We define the probability of a hadron h with momentum p to be identified as a photon of the energy E_γ by $w^{(h|\gamma)}(p, E_\gamma)$. To obtain the probability that a hadron in a real event is identified as a photon of the energy E_γ , this probability has to be folded with the hadron momentum distribution dN_h/dp using the convolution integral

$$P^{(h|\gamma)}(E_\gamma) = \int_{p_{\min}}^{\infty} w^{(h|\gamma)}(p, E_\gamma) \frac{1}{N_{\text{all}}} \frac{dN_h}{dp} dp. \quad (1)$$

The single-particle contamination of the photon spectrum by hadrons is illustrated by Fig. 1, which shows the

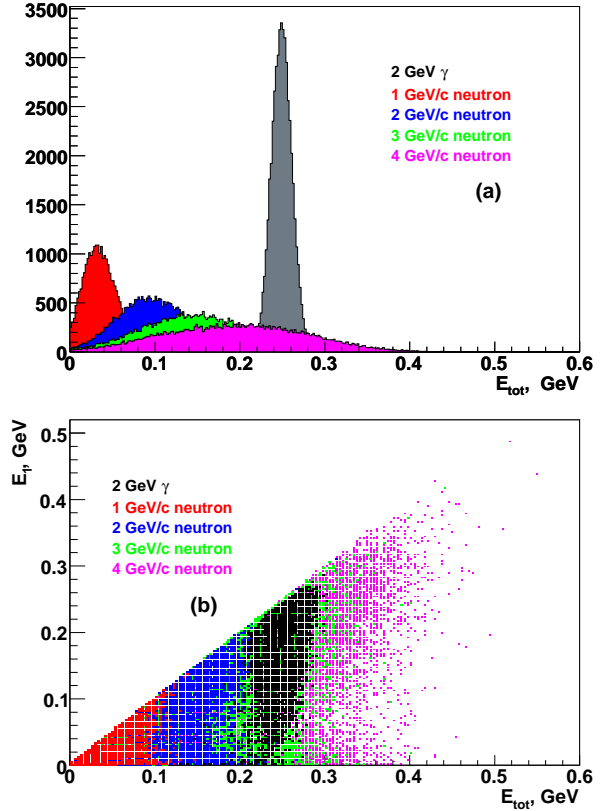


Figure 1: (a) Non-segmented module: energy deposited in the whole ECAL module caused by 2 GeV photons and 1, 2, 3, 4 GeV/c neutrons. (b) 2-segmented module with longitudinal segmentation $10X_0 + 10X_0$: energy deposited in the first segment versus the total energy deposition.

energy deposited by 2-GeV photons and by neutrons of momenta from 1 to 4 GeV/c for non-segmented ECAL modules (a) and the 2-dimensional plot of the energy deposited in the first segment E_1 versus the total deposited energy E_{tot} for modules with 2 longitudinal segments of lengths $10X_0 + 10X_0$ (b). Note that these plots show the energy deposited in the active medium, i. e. the scintillator. For non-segmented modules, photon identification is determined by the range in E_{tot} where 94% of photons reside, while for 2-segmented modules, it is defined by a contour in the (E_1, E_{tot}) space which covers 94% of all photons. For hadrons with momentum p , the contamination probability $w^{(h|\gamma)}(p, E_\gamma)$ is found by the fraction of hadrons falling into a range or a contour which identifies

photons of energy E_γ . As an example, the contamination probability for single neutrons $w^{(n|\gamma)}(p, E_\gamma)$ is shown in Fig. 2 for the non-segmented ECAL module (upper plot) and for the 2-segmented module with the longitudinal segmentation $15X_0 + 5X_0$ (bottom plot). Similar plots were obtained for other hadrons (π^\pm , p , \bar{p} , \bar{n} , K_L^0).

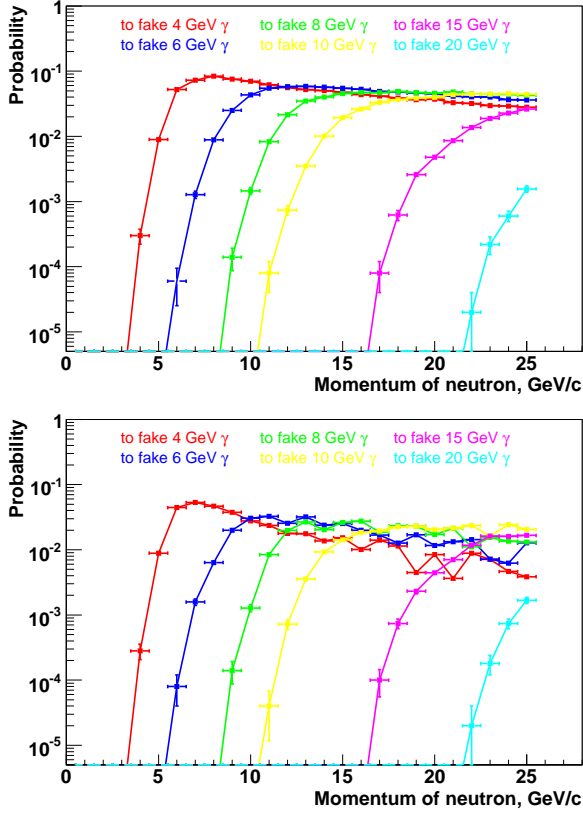


Figure 2: Probabilities for a neutron with different momenta to fake a 4, 6, 8, 10, 15 and 20 GeV photon. The upper plot shows the case of non-segmented ECAL module. The bottom plot is for the case of 2-segmented ECAL modules with longitudinal segmentation $15X_0+5X_0$.

Spectra of hadrons in central Au+Au collisions at a beam momentum of 35 GeV/c per nucleon were obtained with the UrQMD event generator (Fig. 3). The convolution of the single-hadron contamination probability with the particle spectrum according to Eq. (1) results in the contamination probability of hadrons to be identified as a photon in realistic events. This contamination probability for neutrons is shown in Fig. 4 (a) for non-segmented modules and for 2-segmented modules with longitudinal segmentation $15X_0+5X_0$. The ratio of these contamination probabilities is shown in Fig. 4 (b). Similar contamination probabilities were obtained for other hadrons.

Our study showed that the longitudinal segmentation with $15X_0$ in the first segment and $5X_0$ in the second segment provides the best separation of photons from hadrons. ECAL modules with this optimal longitudinal segmentation provide 2.5 times better γ -hadron separation

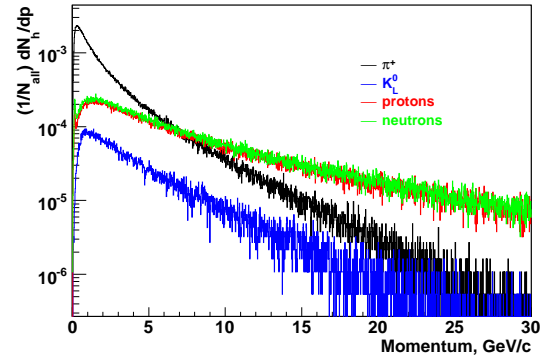


Figure 3: Momentum distributions for various particle types (pion, kaon, proton and neutron), generated by the UrQMD event generator

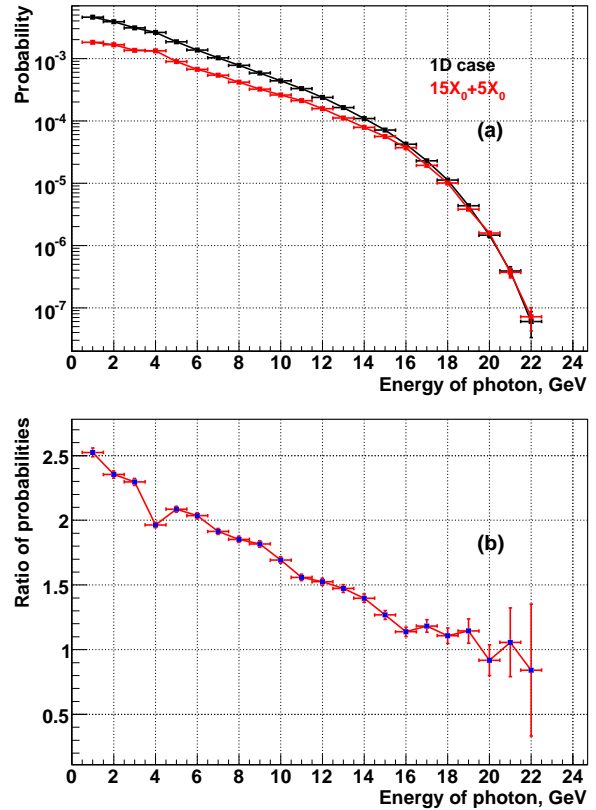


Figure 4: (a) Probabilities of misidentification of a neutron as a photon in the case of non-segmented ECAL modules (black curve) and for 2-segmented ECAL modules ($15X_0+5X_0$, red curve). (b) Ratio of the probabilities (non-segmented to segmented case).

at 2 GeV/c momentum than non-segmented ECAL modules. The hadron contamination to the photon spectrum is at the level of 2 – 5% at $E_\gamma = 2$ GeV and drops to $10^{-8} - 10^{-7}$ at $E_\gamma = 20$ GeV.

Progress on the prototypes of muon system and preshower counters

A. Akindinov, Yu. Grishuk, D. Malkevich, A. Nedosekin, M. Ryabinin, and K. Voloshin
ITEP, Moscow, Russia

In 2008, the R&D at ITEP on scintillating counters based on MRS APD readout for the muon system (MUCH) and the preshower detector of the electro-magnetic calorimeter (ECAL) was focused on the following activities:

- choice of the best optical glue to enhance the amount of light collected by fibers
- choice of the optimal groove diameter to improve the surface response uniformity
- development of a new version of a single-channel electronic board.

The glue selection was performed by means of three identical scintillation tiles sized $100 \times 100 \times 10 \text{ mm}^3$. Ring-shaped grooves, 80 mm in diameter, were used to accommodate two turns of 1 mm-thick wave-length-shifting fiber Kuraray Y11. The free end of the fiber was optically coupled to MRS APD. Uniformity of the fiber pieces was checked during its insertion into one of the tiles. Light collection differed for less than 5%, this value being compatible with the precision of measurements. The light yield from cosmic muons was measured before and after pasting of fibers into tiles, which was performed with three types of glue:

- mono-component glue, polymerizing under UV irradiation,
- double-component optical epoxy cement produced by Bicon,
- double-component epoxy produced by EPO-TEK.

The results are presented in Table 1. Reflective indices of all the glues were approximately the same. Apparently, maximum gain of the light yield, obtained with the EPO-TEK glue, may be explained by the extra transparency enhancement of rough groove walls due to their ‘melting’ under the impact of acid component of epoxies.

glue type	light yield
none	1.00
Mono-component optical glue	1.41
Bicon optical cement	1.58
Epo-Tek 301	1.68

Table 1: Comparison of light yields achieved with different types of glue.

To optimize the diameter of the groove milled in the $100 \times 100 \times 10 \text{ mm}^3$ sized tiles, five tiles with grooves of 50, 60, 70, 80 and 90 mm diameter were produced. Both ends of pasted fibers were coupled to MRS APDs positioned in optical connectors inside the tiles. Each tile was equipped with an electronic board [1]. The surface response was

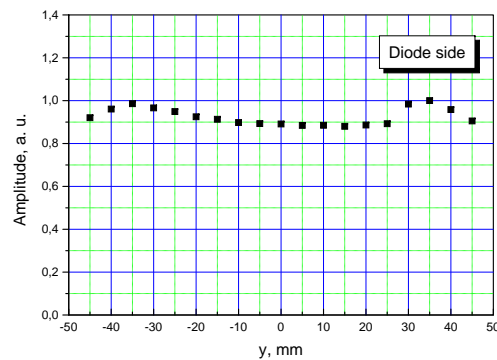
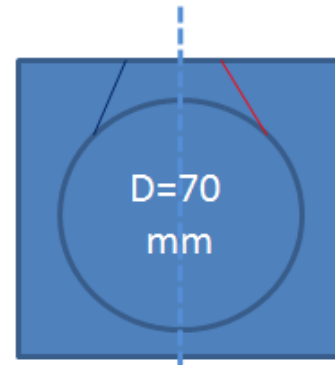


Figure 1: Drawing of a tile with a 70 mm-diameter groove (top) and its amplitude response scanned along its surface (bottom).

scanned with a β -source put into a collimator with a 2 mm port. β -particles were triggered with coincidences of signals from one of the two MRS APDs and a scintillation counter placed after the tested tile. The most probable amplitude from the second MRS APD was measured with a 5 mm increment in both dimensions (361 measurements for each tile). Fig. 1 shows a typical distribution, normalized to the mean amplitude measured at the center of the tile. Root mean squares of amplitude responses for all 5 cases are summarized in Table 2.

D [mm]	50	60	70	80	90
R.M.S. [%]	10.1	8.7	6.6	4.5	5.1

Table 2: Estimation of the response uniformity (r.m.s.) for different values of the groove diameter.

The best result (4.5%) was obtained with a groove diameter of 80 mm. The presented data includes heterogeneity due to MRS APD positioning inside the tiles (0.5%) and

is not corrected for the variation of the extrusion thickness along the tile surfaces (2%). As shown in the previous report [1], a new MRS APD version provides higher signal amplitudes, which allows for usage of only one photodiode per tile keeping the registration efficiency at 100% and the noise rate below 10^{-2} Hz.

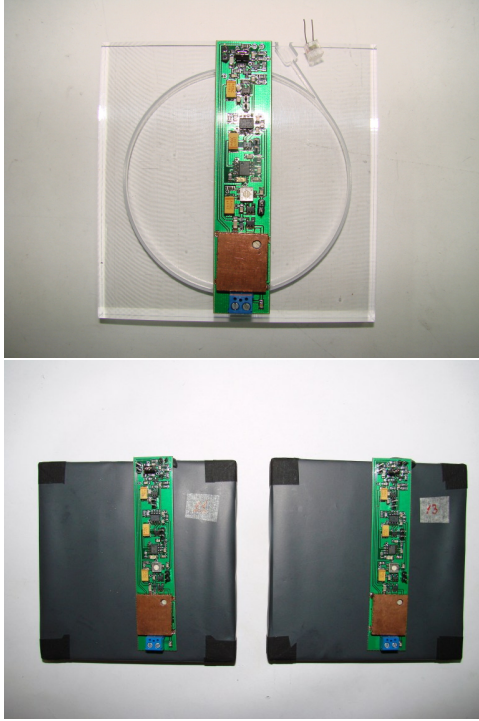


Figure 2: Final version of the scintillation tile: detector components (left) and assembled detectors (right).

Fig. 2 shows the final prototype for MUCH and the preshower detector of ECAL represented by a tile sized $100 \times 100 \times 10 \text{ mm}^3$ with a groove diameter of 80 mm.

Using only one MRS APD required the electronic board to be modified. The new, single-channel version, has inherited all the components of the previous version (power unit, amplifier, discriminator) with the exception of the coincidence circuit (powered with 5–15 V and consuming 115 mW).

Two detectors of the new type were assembled and tested with cosmic particles. Fig. 3 (top) shows their count rate measured in self-triggering mode. The noise input from MRS APD is approximated with a line. Charge spectra, represented in Fig. 3, were measured in self-triggering mode at the discriminating threshold of 140 mV (middle) and with an external trigger (bottom). One can see that above a threshold of 100 mV, the noise from MRS APD is below 10^{-2} Hz, and the count rate is determined exclusively by cosmics. At a threshold of 140 mV, the efficiency of MIP registration exceeds 99%.

Reflective coating of free fiber ends will provide a 1.5–1.7-fold increase of the collected light. This makes further thinning of the plastic plates possible. However, this may

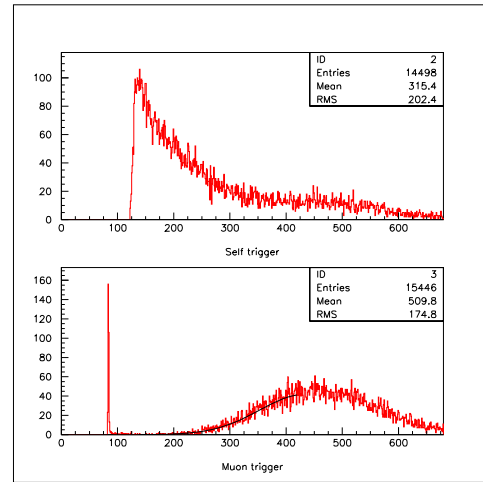
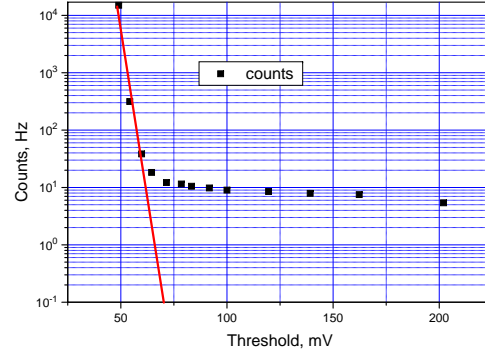


Figure 3: Count rates (top) and charge spectra (bottom) of the final detector version.

lead to the loss of light yield in the groove region. Besides, in this case additional tests of the light yield homogeneity may be needed.

References

[1] ITEP group, **Prototypes of muon system and preshower counters**, CBM Progress Report 2007, p. 47a.

SC dipole magnet for CBM

E.A. Matyushevskiy, P.G. Akishin, A.V. Alfeev, V.S. Alfeev, V.V. Borisov, V.V. Ivanov,
E.I. Litvinenko, and A.I. Malakhov

JINR, Dubna, Russia

Introduction

The dipole magnet is an essential constituent of the planned CBM experiment [1]. The magnet should host the target, the Micro-Vertex Detector (MVD), and the Silicon Tracking System (STS). It is located in the immediate proximity to the RICH detector. A magnetic field in area of the RICH detector should be no more than 250 G. A field integral of 1.0-1.2 Tm over a distance of about 1 m is required. The angular acceptance of the magnet should cover 50° in vertical and 60° in horizontal direction. The magnet gap must be large enough to permit installation and maintenance of the STS (not less than $1.2 \times 1.2 \text{ m}^2$).

The conceptual project SC magnet

A conceptual design of the dipole magnet is presented in Fig. 1. The magnet is supplied with a yoke of magnetically soft steel with low carbon content and superconducting (SC) excitation coils.

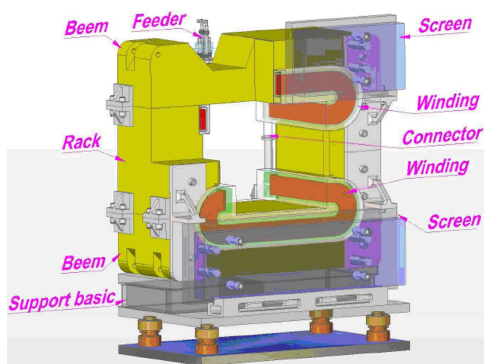


Figure 1: Superconducting dipole magnet.

The upper and bottom beams form the poles of the magnet. The cryostats of the excitation coils are fixed on the magnet yoke.

The coils are supplied with a SC cable of $3 \times 2 \text{ mm}^2$ (without isolation). The cross-section ratio of superconductor material to copper is 1:6. The enhanced copper content in the SC cable allows overheating the cable up to 30 K in case of a quench.

The winding of the magnet consist of two coils connected by adapters (see Fig. 1). The form of the coil "the Cossack saddle" allows to create a magnet with a minimal size along a beam. The coils on the magnet exit are covered by a magnetic screen that reduces the field in the area of the RICH photodetectors.

The cryostat of the excitation coils includes a helium vessel, a nitric screen, and a vacuum casing.

The helium vessel is made of stainless steel and cooled by pipes with liquid helium circulating in them. The helium vessel is held in the vacuum casing by supports made out of fibrous material. Thermal flow through the supports amounts to 1.8 W, the thermal losses through radiation to 0.22 W.

The nitric screen is made of copper. The coolant pipes are soldered to the vessel and cool the screen down to a temperature of less than 80 K. The supports of the nitric screen are placed on the vacuum casing of the cryostat. An inspection plate and hatches on the vacuum casing provide access to the equipment inside. The thermal losses by radiation are 35 W. Pump-down of the casing is provided by oil-free vacuum pumps.

The upper and lower cryostats are coupled by two connectors which hold current conductors, helium and nitrogen tubes, and elements of service and monitoring systems.

The upper cryostat is equipped with a feeder and has two current leads (1.5 kA each) for input-output of the excitation current. The feeder has ports for incoming and outgoing liquid and gaseous helium. The pipelines and the elements of communications going from the feeder to the helium vessel create thermal losses at the level of 3.5 W.

Calculation of the field with the computer codes RADIA, ANSYS and TOSCA has shown that a current of 1.2 kA creates a field of 1.15 T. The field distribution along the Z-axis is presented in Fig. 2 (data from RADIA). The field does not exceed 250 G in photodetectors' plane of the RICH [2].

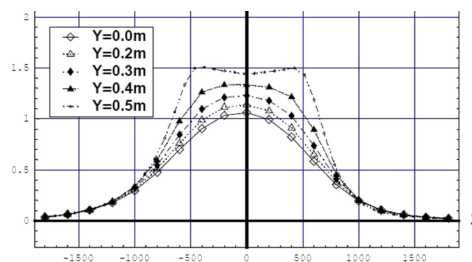


Figure 2: Distribution $|B|$ along the Z -axis at different levels of the magnet gap.

References

- [1] <http://www.gsi.de/documents/DOC-2006-Feb-108.html>
- [2] <http://www.gsi.de/documents/DOC-2008-Oct-173.html>

Test results of n-XYter silicon strip readout chip

K. Kasinski¹, A. Czermak², and R. Szczygiel¹

¹AGH University of Science and Technology, Krakow, Poland; ²Institute of Nuclear Physics PAS, Krakow, Poland

Abstract: The n-XYter integrated circuit (ASIC) was designed in a CMOS 0.35 μm technology, as a 128-channel, data-driven silicon detector readout chip and became a prototype readout chip for several experiments at the FAIR [1]. This report presents a summary of the tests results on discriminator threshold spread and its correction, analogue front-end gain measurements and calibration of the time-stamp circuitry. The details of the test are presented in [2].

Test environment

The test setup is based on a Sucima Imager data acquisition board [3] interconnected to a PCB hosting two n-XYter ASICs, one of which is bonded to a 100 μm pitch, 1 cm long, AC-coupled silicon strip detector. The measurements were performed using on-chip test pulses.

Front-end gain

The front-end parameters were measured by applying the constant amplitude pulses to the inputs of the channels with the average frequency of 175 Hz. Plotting the number

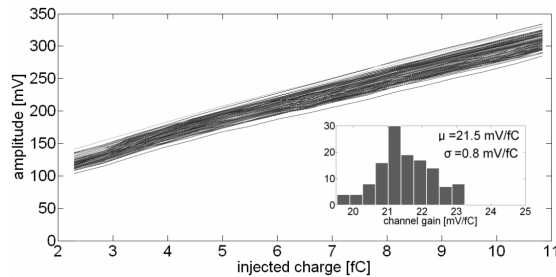


Figure 1: Gain characteristics of 128 channels.

of registered events versus the comparator threshold setting gives an “s-curve”, which allows to estimate the main analogue parameters of the ASIC. The position of the s-curves’ midpoints allows to measure the front-end gain. The gain measurements were performed for the input charge of 2-11 fC (Fig. 1). The average obtained gain was 21.5 mV/fC with the sigma of 0.8 mV/fC.

Effective discriminator threshold spread

The effective discriminator threshold spread was measured for all the channels with 11 fC input pulses. The spread was minimized using internal 5-bit correction DACs located in each ASIC channel. The correction procedure

limited the effective discriminator threshold spread from 2.29 (sigma, threshold DAC LSB units) to 0.42 (Fig. 2).

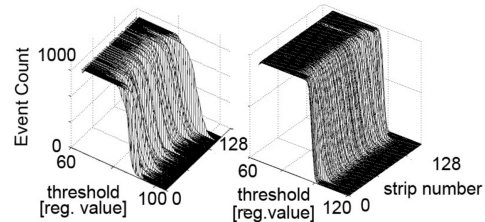


Figure 2: S-curves for 128 n-XYter channels before (left) and after (right) the correction procedure.

Time-stamp calibration

The ASIC allows precise incidence time measurements provided that the time-stamp circuitry is precisely calibrated before. The calibration procedure is based on measuring the selected time-stamp counter pattern probability for random input pulses. An example of such measurement result is presented in Fig. 3. Internal ASIC delay registers

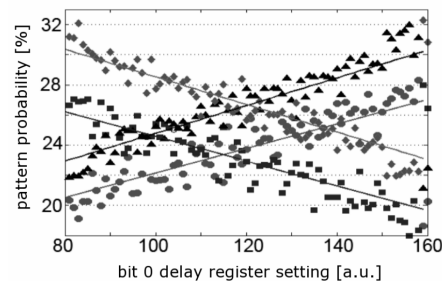


Figure 3: Probability of four selected time-stamp counter patterns.

should be programmed to provide the same probability for all the patterns.

References

- [1] A. Brogna et al., “N-XYTER, a CMOS read-out ASIC for high resolution time and amplitude measurements on high rate multi-channel counting mode neutron detectors” Nucl. Instr. And Meth. A 568 (2006) 301.
- [2] K. Kasinski, A. Czermak, R. Szczygiel, “Test results of a self-triggering silicon strip detector readout chip”, Nucl. Instr. And Meth., 2009, in print.
- [3] A. Czermak et al., “Data Acquisition System SUCIMA Imager”, Proc. 8th. ICATPP, Como, Italy, 6-10 Oct., 2003.

Radiation studies on the UMC 180 nm CMOS process

S. Löchner*

GSI, Darmstadt, Germany

Introduction

Radiation damages to electronic components are an important issue for future FAIR experiments. One of the preferred technology for ASIC developments at GSI is the 180 nm UMC CMOS process. In this regard the ASIC design group of the GSI Experiment Electronic department has been launched a research project in 2007, including the development of an ASIC called *GRISU*. The main goal is the characterisation of Single Event Effects as well as Total Ionising Dose effects on the 180 nm UMC process.

Single Event Effect Studies

Single Event Effect (SEE) is the main generic term for effects in semiconductor devices triggered by the impact of ionising particles. Within the SEE there are more detailed types of effects. Of great interest are the so-called Single Event Upset (SEU) and Single Event Transient (SET) effects.

A good choice to test these effects is the irradiation of the semiconductor devices with heavy ions. Therefore the *GRISU* test chip has been particular designed to monitor these effects during irradiation. For a complete characterisation it is also necessary to measure the impact of ionising particles at different Linear Energy Transfer (LET) levels.

The irradiation tests of the *GRISU* were performed at the GSI linear accelerator (UNILAC) in cave X6. The coverage of the large LET range was obtained with different heavy ions and energy absorption in air. An overview of the in 2008 available ions and the resulting energy and LET parameters are given in Table 1.

Heavy ion	Energy [MeV/AMU]	Energy [MeV]	LET [MeV cm ² /mg]
C-12	0...10.4	0...125	1...5
Ar-40	0...8.8	0...352	7...19
Ni-58	0...7.7	0...447	15...32
Xe-132	0...7.2	0...950	30...60

Table 1: Energy and LET range for available heavy ions radiation tests in 2008.

Exemplarily the overall cross section test results versus LET is shown in Figure 1 for a minimum sized inverter. The critical Linear Energy Transfer (LET_{crit}) as well as the maximum cross section ratio are extracted from the test results for each test structures. Furthermore the sensitivity against SEU for different types of flip-flop and memory cells have been tested.

*s.loechner@gsi.de

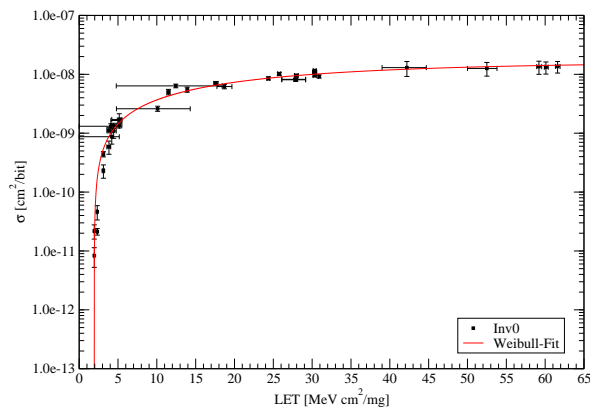


Figure 1: Weibull fit of the SET cross section of a minimum sized inverter.

Total Ionising Dose Studies

In July 2008 a Total Ionising Dose (TID) test was performed at the X-ray irradiation facility of the IEKP [1] / FZK [2]. In total 8 *GRISU* test chips have been irradiated. Table 2 summarises the different dose rates and accumulated doses.

The transient and output characteristics of discrete MOSFET transistors as well as threshold voltage and leakage currents were measured for different accumulated dose levels. Immediately after irradiation the annealing of the chips were measured. Finally, all chips showed a very good annealing performance. After four weeks leakage current has settled back to the initial value.

Number of chips	Dose rate [krad(SiO ₂)/h]	Accumulated dose [krad (SiO ₂)]
1	50	800
2	100	1000... 1200
4	200	1600... 2400
1	490	1500

Table 2: Summary of irradiated *GRISU* chips, dose rates and accumulated doses of the TID test.

References

- [1] Institute of Experimental nuclear Physics (IEKP), University of Karlsruhe (TH)
<http://www-ekp.physik.uni-karlsruhe.de>
- [2] Forschungszentrum Karlsruhe (FZK)
<http://www.fzk.de>

Front-end electronics for CBM

T. Armbruster¹, P. Fischer*¹, and C. Kreidl¹

¹University of Heidelberg, Germany

Abstract

Several sub-detectors of the CBM experiment will require front end amplifier chips optimized for their particular requirements. The FEE group is collecting the various needs and will provide one or more suited chips. During the ongoing preparatory phase, prototypes of important building blocks are studied by the various groups. One main activity in Heidelberg was the design of a preamplifier / shaper / discriminator test chip with varying front end characteristics, scaled on-chip load capacitors for detector emulation and a versatile injection circuit.

CBM FEE Goals

The CBM FEE group is developing self-triggered multi channel charge amplifiers with integrated time stamping, which is required due to the asynchronous operation of the experiment. The requirements of the various interested CBM sub-detectors (STS, TRD, MUCH, RICH) as well as from PANDA (MVD, GEM, TPC) may require more than one design because key parameters like the number of channels, the allowable power, input capacitance, input signal amplitude and distribution and the required amplitude resolution differ significantly. Two architectures are presently pursued: A low power, multi channel system with a moderate amplitude resolution and a chip with less channels, integrated ADC and more sophisticated amplitude processing. Both designs will require a charge amplifier so that a prototype test chip has been developed.

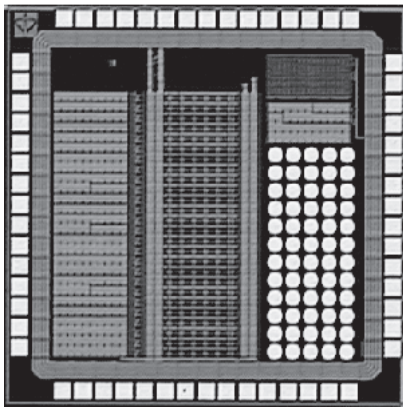


Figure 1: Photograph of the charge amplifier test chip.

Charge Amplifier Test Chip

After an initial design in 2007, a second test chip with 11 channels has been designed, submitted and tested. Each channel contains a charge amplifier with dc feedback, a second order shaper with 80 ns shaping time, a versatile injection circuitry and a discriminator with local threshold trim. All bias currents are generated with on-chip DACs. As it is visible on the chip micro-photograph in fig. 1, the channels (in the middle) are connected to a large amount of capacitors (on the left) to emulate varying detector capacitances. An array of bump bond (on the right) will be used for bumping tests. The chip also contains capacitance measurement circuits (upper right) to determine the exact values of the injection and the load capacitors.

Testing of the chip has started end of the year. All blocks operate as expected. As an example result, fig. 2 shows how the noise for ≈ 10 pF input load decreases when more and more preamplifier unit instances are connected in parallel, so that effectively the amplifier current is increased without change in bias conditions. The behavior is as expected in simulation, albeit at a slightly higher level. The origin of this extra noise (bad calibration, noise injection through ground line,...) still needs to be determined.

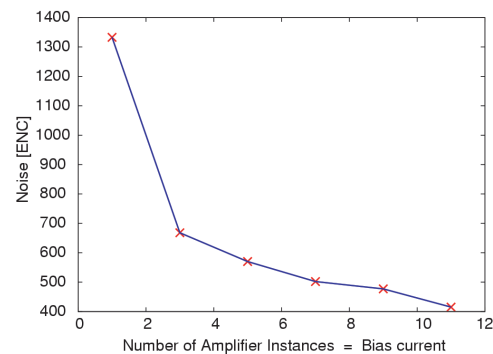


Figure 2: Preliminary ENC for varying input bias currents.

Further Work

In the same framework, bump bonding tests have been carried out, chips in the UMC 0.18 μm technology have been irradiated and work on a radiation hard library has been continued. Work on other building blocks, in particular a low power ADC, has been started.

*peter.fischer@ziti.uni-heidelberg.de

PADI2-3, the second iteration of FEE for CBM time-of-flight measurements

M. Ciobanu^{1,2}, I. Deppner², D. Gonzalez-Diaz¹, N. Herrmann², K.D. Hildenbrand¹, M. Kiš^{2,3}, and A. Schüttauf¹

¹GSI, Darmstadt, Germany; ²Physikalisches Institut, Heidelberg, Germany; ³RBI, Zagreb, Croatia

From the in-beam tests of the PADI1 prototype [1] we have recognized that the minimization of the crosstalk between channels has a priority for further developments. In the new design we have changed the biasing type from voltage biasing to current biasing. The bias block used in the PADI2-3 ASIC is a constant-transconductance bias circuit having wide swing cascode current mirrors similar to the one described in [2]. It gives two currents for each channel and at the channel level all needed biasing voltages are created locally. For the bias block we have used a special layout routing technique in order to realize a good matching of the eight output currents. The layout was designed in a few successive optimization steps involving the simulation with parasitic elements extracted. Finally the eight currents are within a few percent of to the medium value. According to simulations, the increase of cross talk rejection ratio (CTRR) at chip level relative to PADI1 will be of minimum 20 dB. We have increased the number of channels to four

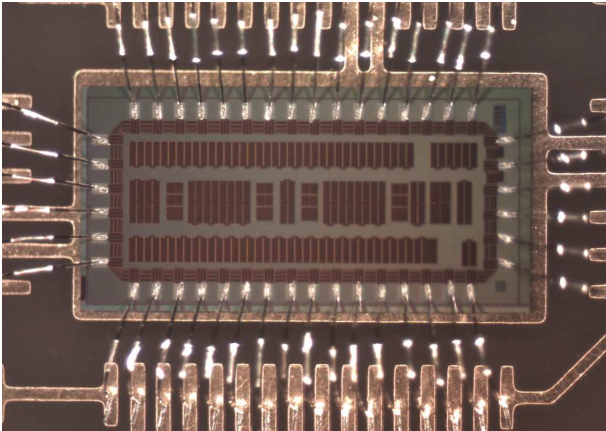


Figure 1: PADI2 (1.5 mm x 3.2 mm) bonded on test PCB.

and we have added an OR feature which allows to daisy-chain chips for trigger purposes. The PADI2-3 chip will be connected to the TDC chip which is currently being developed at GSI [3, 4]. The inputs of this chip accept LVDS signals. We have designed two variants PADI2 and PADI3 which differ in the time output signal levels: ± 100 mV (fixed value, with the common mode dc voltage fixed at the optimum point of the LVDS receiver, e.g., $2/3 \cdot V_{DD}$) and ± 350 mV (programmable value by an external resistor) on 100Ω differential load.

In the new design, all the resistors involved in the main amplification path in preamplifier and in discriminator are implemented by the dynamic impedance of MOS transistors in diode configuration. All differential amplifiers

use the same type the wide swing cascode current mirrors (used already in bias block) and scaled for the needed current. Together with the new biasing, which stabilizes the g_m , the new design has less dispersion of parameters in technological corners related to PADI1. The preamplifier should have a gain $G_{PA} \sim 86$ at an increased bandwidth $f_H \sim 300$ MHz. The external threshold voltage range is extended to ± 300 mV. In the tests of PADI1 we have not used the hysteresis facility and hence it is removed in the new design. Furthermore, in tests with the diamond detectors for counting applications, we have shown that in the ideal case, the discriminator should work with a threshold level within 3-6 times of the noise level. Hence, the discriminator designed for PADI2-3 has an increased gain enabling operation at very low threshold.

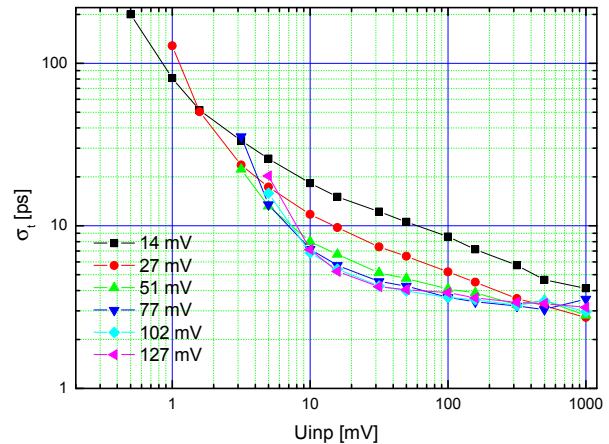


Figure 2: The PADI2 time resolution dependence to input signal amplitude for different threshold voltages.

We have designed a test PCB, for direct bonding of the ASIC (Fig. 1) and the first tests shows that the PADI2 prototypes are fully operational. In the Fig. 2 we present first measured result, an intrinsic time resolution as a function of input signal amplitude for different threshold voltages (preliminary result).

References

- [1] M. Ciobanu et al., IEEE NSS Conf. Rec., N30-18 (2008) 2018 - 2024
- [2] D. Johns and K. Martin, "Analog integrated circuit design", John Wiley & Sons, Inc., p.259, 1997.
- [3] H. Flemming and H. Deppe, IEEE NSS Conf. Rec., N15-25 (2007) 322 - 325
- [4] contribution by Flemming et al. in this report

The GSI event-driven TDC with 4 channels GET4

H. Flemming¹ and H. Deppe¹

¹GSI, Darmstadt, Germany

Introduction

The GSI Event-driven TDC GET4 is the first prototype of a high resolution low power event driven TDC for the CBM ToF detector readout. The design specifications according to the CBM ToF requirements are

- very high time resolution of better than 25 ps
- double hit resolution of better than 5 ns
- event rate up to 50 kHz per channel
- capability to measure time over threshold
- low power consumption less than 30 mW/chan

Table 1: Requirements for the ToF readout electronics

Functional Description

Main part of the time measurement system is the time core with a 128 stage Delay Locked Loop and the timestamp counter. Each of the four channels has a 128 bit clock driven hit register which gets timing signals from the DLL, four data encoders (Figure 1) and two derandomization units shown in Figure 2. The readout of the data is done by a token ring based readout logic.

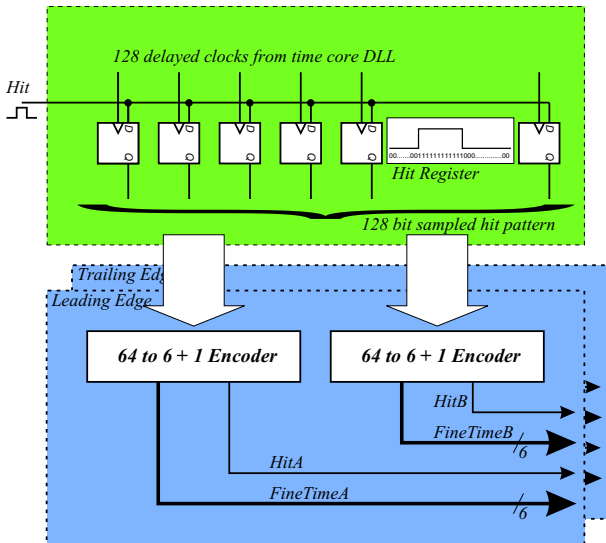


Figure 1: Block diagram of the hit register and encoders

For the time core a 156.25 MHz system clock will be used so that in the lock state of the DLL, when the total delay is equal to one clock cycle time, the delay of a single delay element is $\tau = T_{cyc}/128 = 50$ ps.

The 12 bit timestamp counter which is also clocked with the 156.25 MHz system clock delivers an additional time interval of a counter epoche $t_{epoche} = 26.2144 \mu s$. For synchronisation of the timestamp counter of different GET4 ASICs in a larger system a synchronisation input is available.

To reduce output connections the internal parallel data bus is serialized to an asynchronous data format. Data transmission starts with a low level start bit followed by 24 data bits beginning with the most significant bit. The termination of data transmission is done with a high level stop bit. The serial data clock can be applied over an additional serial clock input. For a mean event rate of 50 kHz/channel a serial data clock rate of at least 10.5 MHz is necessary.

The system clock and Hit signals are fed into the GET4 ASIC via standard LVDS inputs with internal 100 Ω termination resistors. The requirements on the system clock are extremely demanding. As clock jitter has a direct effect on time resolution it must be as small as possible. An acceptable clock jitter is $\sigma_{Clk} \leq 5$ ps. The duty cycle must be 50 ± 5 %.

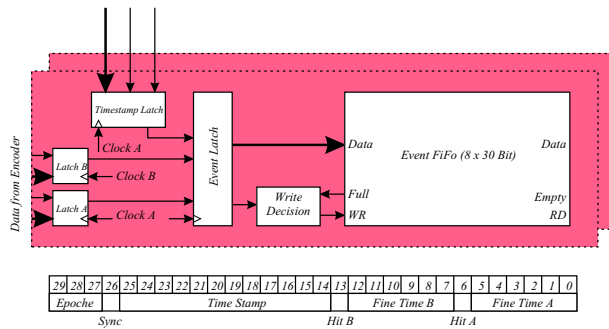


Figure 2: Derandomisation

The GET4 ASIC was submitted in October 2008 on an UMC 180nm Multi-Project-Wafer run und is still under measurements at the EE-Lab GSI. First results will be presented in March 2009.

References

- [1] H.Deppe, H.Flemming: Development of High Resolution TDC ASICs for CBM-ToF, GSI Scientific Report 2007, p. 250

Software development for CBM readout controller board

N. Abel¹, J. Adamczewski-Musch², H.G. Essel², U. Kebschull¹, S. Linev², and S. Müller-Klieser¹

¹KIP, Heidelberg, Germany; ²GSI, Darmstadt, Germany

Readout controller

The readout controller (ROC) is an FPGA-based board, developed at the Kirchhoff Institute for Physics (KIP), University of Heidelberg, for configuration and reading out data from nXYTER chips [1]. Basic readout features of ROC are implemented in VHDL. For high-level functionality (configuration, control, data transport to host PC) a hard-core PowerPC available on the Virtex-4 FX FPGA is used. Communication with host PC is performed via a 100 Mbit Ethernet link.

PowerPC program

The PowerPC program is written in plain C. It runs standalone, without any operating system. Therefore all tasks are handled in a common application loop: data taking from FPGA; storing data into a ring buffer; sending data from ring buffer to the PC; serving control requests from the PC. The main loop is designed such that each task runs not more than few ms at once. Otherwise small FPGA queues would run out of memory and data would be thrown away. The big size of the ring buffer (~110 MB) allows to decouple two major tasks - data taking and data sending. So, the PowerPC can fill the buffer during several seconds without sending data immediately to host PC.

Data transport protocol

The reliable transport of data from ROC to the PC is very important. Due to performance reasons UDP/IP as transport layer is used. It is very simple and does not consume many CPU resources. On the other hand, UDP does not guarantee the delivery of packets and one should implement a retransmission logic.

The designed protocol is fully based on a request-reply scheme - the ROC never sends data without request from host PC. This allows to implement a back pressure logic easily: if the host PC is not able to process data in time, it will not request new data from ROC.

The host PC is protocol master and takes care that no more than 30-40 UDP packets (~1.5 KB size) are requested at once, otherwise the Linux socket buffer would overflow and some of the packets would be lost. To check for a packet loss each packet has a unique id. So the host PC can easily detect missing packets and can request their retransmission.

ROClib library

The C++ based ROClib library provides an API to configure and monitor ROC states via reading/writing

(peek/poke logic) of virtual registers on the ROC. It also implements the transport protocol and offers blocking and non-blocking methods to readout data from ROC in user application. The current ROClib implementation achieves data transfer rate up to 12.3 MByte/s with very low CPU usage.

The ROClib also provides a ROOT [2] dictionary for all classes. Therefore one can use the ROClib within CINT scripts and easily develop controlling and configuration scripts for ROC.

Integration with DABC

The Data Acquisition Backbone Core (DABC) [3] is a general purpose data acquisition framework which allows to integrate experiment specific front-end components. Special device and transport classes were implemented to integrate ROClib functionality into DABC. This allows to configure ROC and take its data directly into DABC modules. To perform ROC-specific data transformations and analysis, two special module classes were written: a combiner of data from several ROCs into one event, and a module for time calibration.

All these components were used in a CBM test beam time in September 2008 to read and store data from 3 ROCs. Special DABC application class was introduced to configure and run all necessary components during beam time. Monitoring of the running DAQ was possible with a Go4 analysis, connected to DABC via socket channel.

Status and outlook

The developed software allows to configure and control ROC from any Linux PC. Data taking with DABC is implemented and was used during September 2008 beamtime. With latest improvements ~7 MB/s sustained rate of data taking is achieved. Further developments are required to reach the possible maximum of 12 MB/s. Implementation of a data transport via optical channel is planned. Information and latest news on <http://cbm-wiki.gsi.de>

References

- [1] A.S. Brogna et al., "N-XYTER, a CMOS read-out ASIC for high resolution time and amplitude measurements on high rate multi-channel counting mode neutron detectors", Nucl. Instrum. Methods A 568 (2006), pp. 301-308
- [2] ROOT - object oriented analysis framework, <http://root.cern.ch>
- [3] J. Adamczewski, H.G. Essel, N. Kurz, S. Linev, "Data Acquisition Backbone Core DABC", IEEE Trans.on Nucl. Science, Vol.55, No.1, February 2008, pp. 251-255

A generic link protocol for the CBM DAQ system

F. Lemke, U. Brüning¹

¹University of Heidelberg, Mannheim, Germany

Introduction

The availability, reliability and the cost-effectiveness of high speed serial optical links increase the demand for using such links to connect the front end electronics (FEE) of a detector to the back end processing farm. This requires developing efficient protocols for such links, which fulfill the requirements of a detector control and data transport system. The developed generic link protocol (GLP) combines all functions for a detector control and data transport system including the time synchronization into one transmission link by using virtual channels in order to provide quality of service for the various tasks. The GLP can be used to interconnect modules providing high speed serializer/deserializer (SERDES) functions. It is a point-to-point interconnect function using one SERDES lane and an internal 16+2 bit interface. The various features of this protocol will be described.

The GLP features and message types

The goal of the GLP [1] is to fusion all required functions of the detector network into one link protocol, as there are the time synchronization, the data read out and the detector control. Different traffic classes are provided in order to fit the requirements of the specific message types. Every traffic class is supported by a virtual channel to make these classes independent of each other. Moreover the classes have different priorities to access the physical link. The following traffic classes are supported:

- Deterministic Latency Messages (DLM)
- Data Transport Messages (DTM)
- Detector Control Messages (DCM)

The link layer has a speciality build in for the time synchronization of large networks, the Deterministic Latency Messages (DLM). This type of message is of fixed length with a packet size of only (16+2) bit. They are more a special control character than a message because they carry no real payload. The 16 special coded variants can be inserted at any time into the message stream and are received in the DLM channel. This allows synchronizing the time with a deterministic latency. The resolution of the time synchronization is related to the bit clock of the link, e.g. below 400ps for a 2.5Gbit/s link speed. If there are intermediate switch level required, the DLM is forwarded by a special switch layer with deterministic latency. Data Transport Messages (DTM) are used to read out data from the FEE with high data rate. A variable payload of 8 Bytes to 64 Bytes is supported. The link allows bidirectional data



Figure 1: Data Combiner Board

transfers although the data stream is mainly unidirectional. Each data packet carries a CRC for link error detection.

Detector Control Messages (DCM) use its own virtual channel with CRC check and automatic hardware retransmission and an acknowledge message to provide a secure transport channel. The payload is defined by the user and can be used to access external register files in the FEE by using PUT GET semantics.

When the system is started an automatic sophisticated link initialization is performed. After the initialization is done, the network can be used by the GLP to send messages. In case of a synchronization loss, the network links automatically reinitialize. The initialization, the packaging, the CRC checking and the handling of special network functions is done in the Link Port Module, which is provided as a synthesizable HDL module with an easy to use interface [2].

The GLP uses bidirectional point-to-point connections, therefore it works without routing on this level. Routing information can be easily added later in the next layer, if it is needed to forward the messages into larger networks.

The GLP eases the task of constructing DAQ systems and will be verified with a test environment and the existing Xilinx V4 Data Combiner Board (DCB) shown in figure 1.

References

- [1] F. Lemke, GLP Design Document, Computer Architecture Group, University of Heidelberg, (2008).
- [2] F. Lemke, CBM Network Interface, Computer Architecture Group, University of Heidelberg, (2008).

Improved Active Buffer Board of CBM

W. Gao^{*1}, A. Kugel¹, A. Wurz¹, R. Männer¹, G. Marcus¹, and N. Abel²

¹Chair for Computer Science V, ZITI, University of Heidelberg, Mannheim, Germany; ²KIP, University of Heidelberg, Heidelberg, Germany

Abstract: The current PCIe interface of the Active Buffer Board of CBM was enhanced to enable run-time modifications of the functionality using dynamic partial reconfiguration of the FPGA. The DMA logic was ported to the newest FPGA technology which provides a 64 bit PCIe module in contrast to the previous 32 bit version. The DMA engine works well without changing the software environment. A dual-ported event buffer mechanism was developed, using external SDRAM instead of the FPGA internal memory.

Introduction

The Active Buffer Board (ABB) receives CBM events, performs local buffering and formatting and forwards them to the host PC. The present ABB prototype is based on a 4-lane PCI Express (PCIe) card with one XILINX Virtex-4FX60 FPGA, a 2.5Gbit/s optical interface, 32MB of DDR memory and expansion connectors.

The basic PCIe interface uses a commercial IP core with a user-logic interface operating at the transaction layer. To achieve acceptable bandwidth (several 100MB/s) a custom data-flow controller – the DMA engine – is required which links the transaction layer interface with the memory subsystem.

32 bit PCIe DMA design ported to 64 bit

So far the DMA engine uses a PCIe interface module with a soft core in the Virtex4 FX20 FPGA [1]. The design took over 95% of the FPGA resources already for a 32 bit version. Since the new Virtex5 LX110T development board offers better performance and more logic resources, we ported the existing test environment to it. To keep the software including driver and test program unchanged, the 32 bit DMA logic and the simulation environment were ported to 64 bit because the PCIe core in Virtex5 is a 64 bit version only. This required to modify state machines and other logic in the DMA engine.

PIO and DMA tests are no problem on the Virtex5 development board with the block RAM as the target memory. The Virtex5 test in the existing Virtex4 software environment was successful. The DMA performance is about the same as that of the Virtex4 board.

Dynamic Partial Reconfiguration on Virtex4

Operating systems require that certain peripheral devices must be permanently operational from boot time. This con-

flicts with the need to modify functionality, which is typical for re-configurable peripherals like the ABB, as a re-configuration disconnects the PCIe interface until a subsequent reboot. One solution is dynamic partial reconfiguration (DPR) which allows to modify part of the FPGA, while another part remains unchanged and operational. In our design the PCIe interface is static and keeps running, while the DMA engines are dynamic and reconfigured, without computer reboot. Such an approach is very efficient, but it requires careful partitioning of the FPGA logic. The boundary between the static and the dynamic part requires the use of special interconnect elements that introduce one extra cycle of delay so that the original design has to be modified accordingly.

The DPR mechanism was implemented and tested on the ABB [1], by using 2 DMA engines as dynamic modules. To meet the timing constraint of 250 MHz for the global clock, synchronous busmacros are essential and hence, logic rewrite and reverify were done to preserve the original logic behaviour. The DMA performance tests show less than 1% penalty due to the busmacros, because the DMA channels are well pipelined [2].

Event buffer using paired SDRAM modules

The present memory interface of the DMA engine uses dual-ported memories available within the FPGA of a few 10 kB size only [1]. To allow larger dual-port buffers, a mezzanine for the Virtex-5 board has been designed. By interleaving the address areas of two SDRAM modules and providing both address and control buses independently to the FPGA, an almost perfect dual-port emulation can be obtained for the dominant access pattern of short bursts. In this way the memory size can be enlarged to several 10 MB or even GB. This fulfills the concurrent requirement of the Event Buffer, delivers the expected performance, and can be generalized for similar high performance concurrent memory design. Logic design and verification for this buffer are done, and tests are in preparation.

References

- [1] J. Adamczewski, et al. Data Communication Tests on Active Buffer Board. GSI Scientific Report 2007. July 2008.
- [2] W. Gao, et al. DPR in CBM: an Application for High Energy Physics. DATE'09 (accepted).

* wenxue.gao@ziti.uni-heidelberg.de

Data Acquisition Backbone Core DABC v1.0

J. Adamczewski-Musch¹, H.G. Essel¹, N. Kurz¹, and S. Linev¹

¹GSI, Darmstadt, Germany

DABC purpose The DABC [1] addresses requirements of FAIR experiments like CBM [2] for detector and data acquisition test beds. As it is implemented it also provides a general purpose DAQ framework for experiments in production. DABC is able to handle any kind of front-end systems and provides event building over fast networks using commodity hard- and software. Especially a mixture of commonly used MBS (daq.gsi.de) based front-ends and time stamped data streams is supported.

The DABC software written in C++ is developed on Linux. Arbitrary front-end systems (FES) can be connected to standard PCs (by hardware or network). Application specific software plug-ins for handling the front-ends have to be provided by the application programmers.

DABC components The DABC consists of a core system providing the data flow and processing, and a control environment providing state machines, task controls, monitoring and setup/configure mechanisms. The controls environment uses DIM servers (dim.web.cern.ch) and a generic Java written GUI for control and monitoring. Fig.1 shows the main components of the core. *Modules* (application

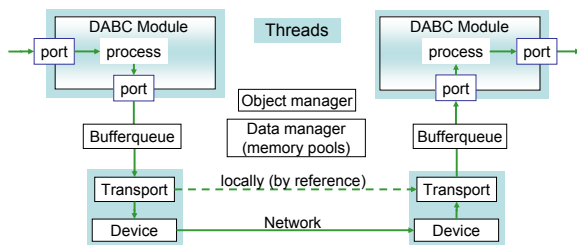


Figure 1: Data flow model with software components.

plug-ins) process the data which is kept in buffers of smart memory pools. *Transport* and *Device* classes handle data sources, networking, data storage, or data servers. *Transports* connect *Modules* via buffered *Ports*, either locally or remotely. The components may run in separate threads to utilize multi core PCs. Central managers organize all objects.

DABC applications Some applications implemented:

1. MBS event builder. MBS front-end systems are connected via TCP to DABC nodes for event building. The MBS DIM servers provide control and monitoring by the DABC GUI, also in a stand-alone mode.
2. PCI express board [3]. All plug-ins have been implemented. Data rates between 400 MBytes/s (reading) and

700 MBytes/s (writing) have been measured.

3. CBM readout board [4]. Three boards were used in a test beam time to read out front-end boards equipped with nXYTER chips. They were sending the data via Ethernet with a UDP based protocol to a PC. The DABC plug-ins did some processing and storage. Through a data server (MBS stream server protocol) standard analysis programs Go4 [5] has been used to perform some more detailed monitoring on-line.

Controls and monitoring Parameters and commands can be specified in the application plug-ins. The GUI builds up displays from all services provided by the DIM servers. Special parameters like rates or states are visualized.

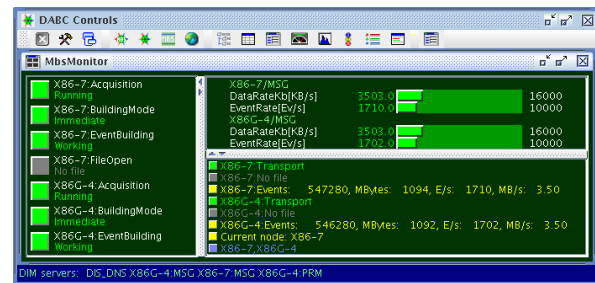


Figure 2: MBS rate meters and status displays.

Status and outlook DABC version 1.0 will be published begin of 2009 (see [6]). The plug-in API has been implemented after a redesign. No more external packages except DIM are needed. In 2008 DABC was used in a first test beam time to test CBM detectors and front-end components. More complex setups will follow in 2009.

References

- [1] J. Adamczewski, H.G. Essel, N. Kurz, S. Linev, "Data Acquisition Backbone Core DABC", IEEE Trans. on Nucl. Science, Vol.55, No.1, pp. 251-255, Feb. 2008
- [2] "CBM progress report 2007", GSI, February 2008
- [3] J.Adamczewski et al. "Data Communication Tests on Active Buffer Board", GSI report 2007
- [4] S.Linev "Software Development for CBM Readout Controller Board", GSI report 2008 (this report)
- [5] J. Adamczewski-Musch, H.G. Essel, S. Linev, "Go4 Analysis Framework v4", GSI report 2008 (this report)
- [6] Web site: dabc.gsi.de

D^0 decay feasibility study in the CBM experiment

I. Vassiliev^{1,2} and I. Kisel^{1,2}

¹GSI, Darmstadt, Germany; ²KIP, Ruprecht-Karls University, Heidelberg, Germany

One of the major experimental challenges of the CBM experiment is to trigger on the displaced vertex of the D -meson hadronic decay mode $D^0 \rightarrow K^- \pi^+$ in the environment of a heavy-ion collision. This task requires fast and efficient track reconstruction algorithms and high-resolution secondary vertex determination. Particular difficulties in recognizing the displaced vertex of the rare D meson decays are caused by weak decays of K_S^0 and hyperons, which produce displaced vertices downstream of the target, the very low multiplicity of the D meson and its low branching ratio, and multiple scattering in beam pipe and detectors.

To study the feasibility of a D^0 and \bar{D}^0 measurement in the CBM experiment, a set of 10^4 central Au+Au UrQMD events at 25 AGeV were simulated. One D^0 (\bar{D}^0) decay to $K^\mp \pi^\pm$ was added to each event in order to simulate a signal in the environment of background hadrons. The most realistic MVD/STS geometry with 2 MAPS at 5 cm (thickness 300 μm) and 10 cm (thickness 500 μm) and 8 double-sided segmented strip detectors was tested. The inner radius of the first MVD detector has been chosen to 5.5 mm in order to reduce radiation damage. The primary vertex was reconstructed with high accuracy (5.7 μm in z direction, 1.0 μm in x and y) from about 400 tracks fitted in the STS with a non-homogeneous magnetic field by the SIMDized Kalman filter procedure described in [1].

An ultra-fast track finder was developed to reconstruct the D mesons. After finding the primary vertex using all reconstructed tracks, the algorithm reconstructs the D^0 meson from its two daughter particles using the primary vertex as the production point. Since the geometrical acceptances of the MVD and STS detectors are not the same, the sample of the reconstructed D^0 mesons consists of 3 subsets shown in Fig. 1 with different z_{vertex} resolutions (36 μm , 56 μm and 66 μm , respectively).

Because of originating from a displaced decay vertex, the D^0 meson daughter tracks have a non-vanishing impact parameter at the target plane. Since the majority of the primary tracks have very small impact parameters, a significant part (99%) of the background tracks is rejected using a cut on their χ^2 distance to the primary vertex. The remaining combinatorial background is suppressed mainly by the vertex quality cuts χ_{geo}^2 and χ_{topo}^2 . Numbers for multiplicity, cut efficiencies, acceptance, z_{vertex} resolution, mass resolution, signal-to-background ratios, and yields per 10^{12} central interactions are presented in Table 1.

After applying all cuts, the $D^0 \rightarrow K^- \pi^+$ reconstruction efficiency is 4.4%. Fig. 1 shows the reconstructed signals on top of the combinatorial background, the shape of which was estimated using the event mixing technique. We obtain

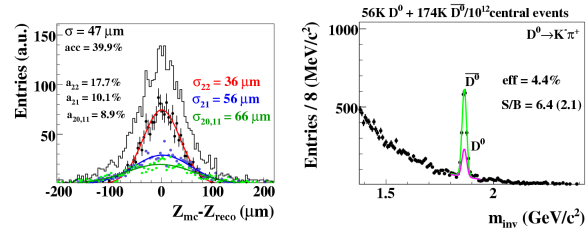


Figure 1: (Left) z_{vertex} resolution of the reconstructed D^0 mesons. Black dots correspond to the case where each of two daughter particles has 2 MAPS hits, blue dots - one of the daughter particles has no hit in the first MVD station, green dots - one of the daughter particles has no hit in the MVD stations or both daughter particles have no hits in the first MVD station. (Right) $D^0 + \bar{D}^0$ signal and combinatorial background invariant mass spectra. The estimated signal and combinatorial background correspond to 10^{10} central events.

a signal to background ratio of about 2.1 for $D^0 \rightarrow K^- \pi^+$ and about 6.4 for $\bar{D}^0 \rightarrow K^+ \pi^-$.

Table 1: Acceptance and efficiencies, mass resolution, signal-to-background ratio (S/B) in a $2\sigma_m$ region around the peak, and yields for open charm reconstruction in central Au+Au collisions at 25 AGeV beam energy. The total efficiency is calculated from the product of geometrical acceptance, reconstruction efficiency, and cut efficiencies.

	D^0	\bar{D}^0
decay channel	$K^- \pi^+$	$K^+ \pi^-$
multiplicities	$0.37 \cdot 10^{-4}$	$1.15 \cdot 10^{-4}$
branching ratio	3.8%	
geometrical acceptance	39.9%	
reconstruction efficiency	99%	
z_{vertex} resolution	47 μm	
total efficiency	4.4%	
$\sigma_m [MeV/c^2]$	10.0	
S/B $_{2\sigma}$ ratio	2.1	6.4
yields / 10^{12} events	56k	174k

References

- [1] S. Gorbunov et al., *Fast SIMDized Kalman filter based track fit*, Comp. Phys. Comm. 178 (2008) 374-383

D^+ decay feasibility study in the CBM experiment

I. Vassiliev^{1,2} and I. Kisel^{1,2}

¹GSI, Darmstadt, Germany; ²KIP, Ruprecht-Karls University, Heidelberg, Germany

The measurement of the different charmed mesons and the Λ_c is important for getting a solid estimate on the total charm production cross section near threshold. D^\pm mesons have a lifetime of 312 μm ; therefore, the most important step in their identification is the precise detection of the secondary decay point. For this purpose, the high-resolution MVD detector (two MAPS detectors of 300 μm at 5 cm and of 500 μm at 10 cm downstream of the target) is used in order to suppress the background from kaons and pions emitted at the primary vertex. No kaon or pion identification with TOF is applied; however, it is important to use the time-of-flight measurements in order to reject proton tracks from the sample. A novel ultra-fast track finder (10 times faster than the standard one) was developed for the selection of D^\pm meson daughter particles. Only tracks with momentum above 1 GeV/c from the target region were selected.

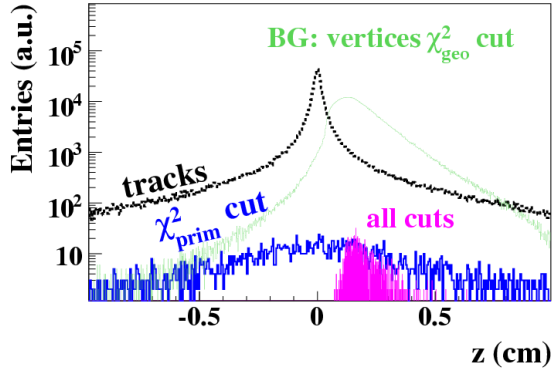


Figure 1: Distribution of single tracks and secondary vertices along the beam line for $D^+ \rightarrow K^- \pi^+ \pi^+$ reconstruction. The black line shows all primary tracks, the blue line those selected by the χ^2_{prim} cut as single track candidates for D^+ daughters. The light green curve shows the 3-particle secondary vertices after first geometrical cuts, the magenta line denotes the finally selected D^+ candidates including more stringent topological cuts.

In order to reconstruct the D^\pm -mesons with a satisfactory signal-to-background ratio, a set of mainly topological cuts were applied to single tracks as well as to reconstructed vertices. As an example, Fig. 1 presents the resulting background suppression of such cuts for the 3-particle decay of the D^+ meson. The χ^2_{prim} cut on single tracks relies mainly on the back-extrapolation of the tracks to the primary vertex requiring them to miss it. For the reconstructed charmed mesons, the back-extrapolation

is required to point to the primary vertex, which allows to strongly reduce the geometrically reconstructed 3-particle vertices.

The reconstructed invariant-mass spectra of the D^\pm mesons in central Au+Au collisions at 25A GeV beam energy are shown in Fig. 2. Numbers for efficiency and acceptance are presented in Table 1. The multiplicities were taken from the HSD model. It should be noted that the statistical model predicts multiplicities which are higher by a factor of 2–3.

Table 1: Acceptance and efficiencies, mass resolution, signal-to-background ratio (S/B) in a $2\sigma_m$ region around the peak, and yields for open charm reconstruction in central Au+Au collisions at 25A GeV beam energy. The total efficiency is calculated from the product of geometrical acceptance, reconstruction efficiency, and cut efficiencies.

	D^+	D^-
decay channel	$K^- \pi^+ \pi^+$	$K^+ \pi^- \pi^-$
multiplicities (HSD)	$4.2 \cdot 10^{-5}$	$8.9 \cdot 10^{-5}$
multiplicities (SM)	$8.4 \cdot 10^{-5}$	$2.9 \cdot 10^{-4}$
branching ratio	9.5%	
geometrical acceptance	39.6%	
reconstruction efficiency	97.5%	
z_{vertex} resolution	47 μm	
total efficiency	2.6%	
$\sigma_m [\text{MeV}/c^2]$	10.0	
S/B $_{2\sigma}$ ratio	1.1	2.4
yields / 10^{12} events	103k	195k

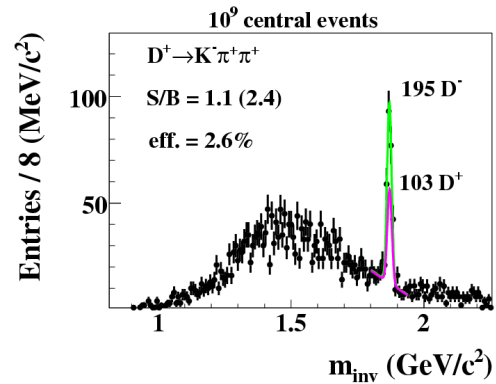


Figure 2: Reconstructed D^+ (magenta) and D^- mesons (green) in 10^9 central Au+Au collisions at 25A GeV

H -dibaryon $\rightarrow \Lambda\Lambda$ detectability study in the CBM experiment

I. Vassiliev^{1,2} and I. Kisel^{1,2}

¹GSI, Darmstadt, Germany; ²KIP, Ruprecht-Karls University, Heidelberg, Germany

Recent measurements found evidence for the existence of a H -dibaryon ($uuddss$, $I = J = 0$) decaying into a pair of Λ hyperons [1]. In the following, we discuss the possibility to detect H -dibaryons via the $\Lambda\Lambda$ channel with the CBM setup. Our simulations are based on a H -dibaryon decay length of $c\tau \approx 1 - 5$ cm as predicted by [2]. The Silicon Tracking System (STS) of CBM is well suited to reconstruct Λ hyperons (decay length 7.89 cm) and to distinguish the signals from the background.

The feasibility study of H -dibaryon detection is based on 10^4 central Au+Au UrQMD events at 25A GeV. In each event, a decay of a $(\Xi^0\Lambda)_b$ ($c\tau = 3$ cm) into $\Lambda\Lambda$ has been added in order to simulate the signal in the environment of background hadrons.

The background is dominated by about 32 primary Λ hyperons which are produced per central UrQMD event. Within the STS detector acceptance, 11 Λ particles are reconstructed on average. The STS comprises 2 silicon pixel detectors (MAPS) at 10 cm and 20 cm (thickness 500 μm), and 8 detector layers consisting of double-sided silicon micro-strip sensors. Particle identification via time-of-flight is performed for protons only (not for kaons or pions) in order to reconstruct $\Lambda \rightarrow p\pi^-$ decays. A typical signal event $H \rightarrow \Lambda\Lambda \rightarrow p\pi^-p\pi^-$ is shown in Fig. 1.

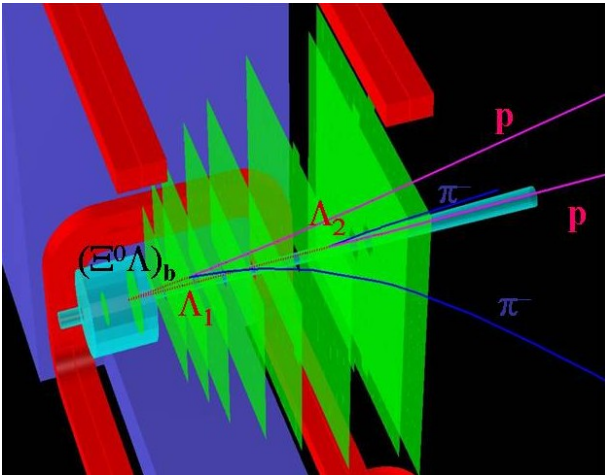


Figure 1: Event display of a H -dibaryon decay into $\Lambda\Lambda$

The H -dibaryon decay vertex is typically located between the MAPS stations about 5 - 15 cm downstream from the target. Λ particles mostly decay in between the STS detector stations. The reconstruction of the event topology comprises several steps: (i) track reconstruction, where all tracks are found but only tracks with $\chi^2_{primary} > 3\sigma$ are selected; (ii) Λ search, where protons identified by the

TOF detector are combined with the π^- tracks, and the invariant mass of the reconstructed particle is compared with the PDG's Λ mass value; (iii) rejection of primary Λ , where only Λ with $\chi^2_{primary} > 3\sigma$ are chosen; and (iv) finally, the reconstruction of detached H -dibaryons (vertex located more than 5 cm downstream from the target). In the last step, good geometrical ($\chi^2_{geo} < 3\sigma$) and topological ($\chi^2_{topo} < 3\sigma$) vertices are required for the reconstructed H -dibaryons. The shape of the background invariant-mass spectrum was obtained using the event mixing technique.

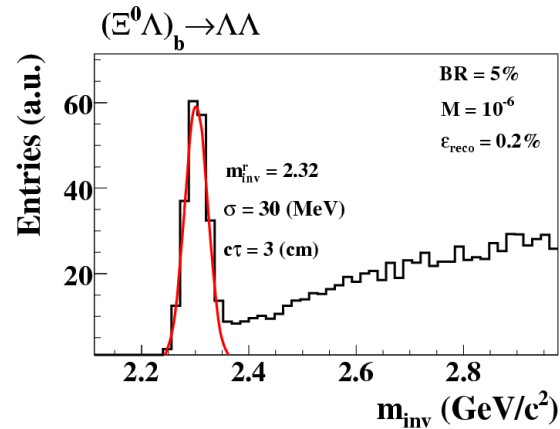


Figure 2: Invariant-mass distribution of reconstructed $\Lambda\Lambda$ candidates

The signal and background invariant-mass spectrum is shown in Fig. 2. The signal reconstruction efficiency is about 0.2%. For the simulations, we assume a multiplicity of 10^{-6} and a branching ratio of 5%, which means in 20 million events there is only one H -dibaryon decay. The reconstructed mass value of 2.32 ± 0.03 GeV/c^2 is in a good agreement with the simulated one (2.318 GeV/c^2). The invariant-mass resolution ($\sigma = 30$ MeV/c^2) is limited by the fact that the tracks of the Λ daughter particles produce hits in 4 or 5 detector stations only.

References

- [1] C. J. Yoon et al., Phys. Rev C 75 (2007) 022201(R)
- [2] J. Schaffner-Bielich, R. Mattiello, and H. Sorge, arXiv:nucl-th/9908043v2 (2000)

Event-by-event fluctuations of the K/π yield ratio in the CBM experiment

D. Kresan and C. Höhne

GSI, Darmstadt, Germany

Non-statistical event-by-event fluctuations are considered an important signal for the critical endpoint of the QCD phase diagram. In future, the CBM experiment at FAIR will investigate the intermediate region of this phase diagram in great detail, searching for the first-order phase transition line and the expected critical endpoint. It is therefore important to closely investigate its sensitivity towards particle ratio fluctuations in Au + Au collisions at 10-45 A GeV beam energy.

A detailed description of the track reconstruction and hadron identification in the STS, TRD, and TOF systems of CBM is given in [1]. In this report, we employ a more advanced TOF detector response simulation, including features like segmentation and double hits, as well as improved TRD track reconstruction algorithms [2], which yield a global track reconstruction efficiency of 86.4 %. Figure 1 shows the reconstructed squared mass of the particles as function of momentum. The m^2 distribution is nearly Gaussian, with small tails caused by track mismatches between TRD and TOF, and by double hits in the TOF detectors. For this fluctuation study, particles are identified on a track-by-track basis using a momentum-dependent window in m^2 around the expectation value. As the width of the m^2 distribution is a quadratic function of p , the required purity of kaon selection sets an upper momentum limit; clean kaon identification is possible up to $p = 3.5$ GeV. The momentum range can be extended to $p = 5$ GeV when a contamination of maximal 50 % is allowed.

Figure 2 (left) shows the eventwise distribution of the ratio $(K^+ + K^-)/(\pi^+ + \pi^-)$ derived for central Au+Au collisions at 25 A GeV generated with UrQMD, after full detector simulation, reconstruction, and particle identification. It is dominated by statistical fluctuations arising from finite number statistics and detector resolution. This background is reproduced using the event mixing technique

which destroys all correlations inside one event. Dynamical fluctuations are then extracted by geometrically subtracting the relative width of the mixed-event distribution from that obtained for same events.

The dependence of the fluctuation result on the required purity of the kaon sample is shown in Fig. 2 (right). The restricted momentum range for a higher purity of the selected kaons introduces a shift of the dynamical fluctuations on the (1 - 2) % level compared to an analysis in the full acceptance or in 4π . This acceptance effect is also seen when using the MC truth for the kaon identification, but applying the same upper limit on momentum. From this agreement we conclude that the kaon identification procedure does not introduce a significant bias in the non-statistical K/π fluctuation results. The acceptance changes the measured fluctuation by less than 1 %, which expresses the sensitivity of the CBM experiment to the physical fluctuation signal.

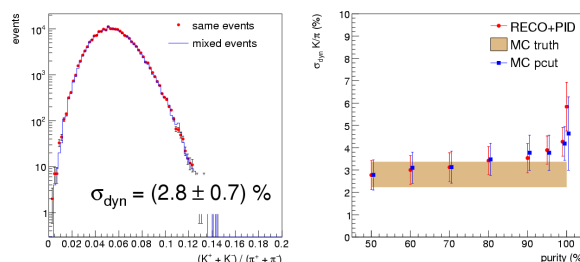


Figure 2: (Left) Distributions of the event-wise kaon-to-pion ratio for data and mixed events, obtained for central Au+Au collisions at 25 A GeV from UrQMD. A minimal kaon purity of 50 % was required. (Right) Dynamical fluctuations of the kaon-to-pion ratio as a function of purity of the kaon identification.

References

- [1] D. Kresan and V. Friese, *Global tracking and hadron identification in the CBM experiment*, CBM Progress Report 2006, Darmstadt 2007, p. 7
<http://www.gsi.de/documents/DOC-2007-Mar-137.html>
- [2] A. Lebedev et al., *Track reconstruction in the TRD and MUCH detectors of CBM*, this report

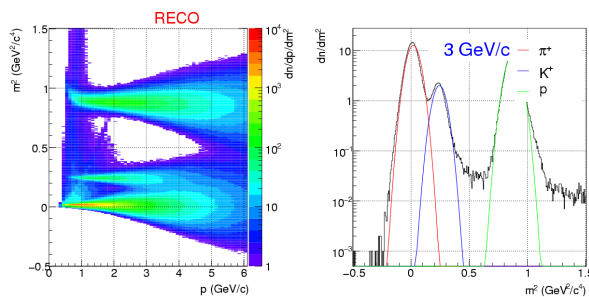


Figure 1: (Left) Squared mass vs. momentum of reconstructed hadrons; (right) m^2 distribution for $p = 3$ GeV.

Systematic investigations on di-electron reconstruction in CBM

T. Galatyuk^{1,2}, C. Höhne¹, and J. Stroth^{1,2}

¹GSI, Darmstadt, Germany; ²IKF, Frankfurt am Main, Germany

The CBM experiment at the future accelerator facility FAIR will make use of proton beams with energies of 10 – 89 GeV, and of nuclear beams with energies of 10 – 44 GeV/u. The experimental strategy how to assess best the low-mass vector mesons by means of their electromagnetic decay at different collision energies and system sizes is under careful investigation. The systematic behaviour of the signal-to-background (S/B) ratio as function of collision energy will be presented in this report.

The general challenge of di-electron measurements in heavy-ion collisions is to cope with the large background of electrons originating from other than the desired sources. Several topological cuts have been developed to reduce the background. The analysis strategy described in Ref. [1] was applied for electron pair reconstruction in central $Au + Au$ collisions at 15 and 35 GeV/u beam energy. The S/B ratio for the three beam energies (15, 25 and 35 GeV/u), assuming no excess over the known decay sources, is depicted in Fig. 1. It is naturally higher at lower energies, as particle multiplicities at lower energies decrease (see Ref. [2]). This of course reduces the signal and combinatorial background at the same time. However, the signal decreases linearly while the background goes down quadratically. The larger increase of the S/B ratio from 15 to 25 GeV/u beam energy compared to the one from 25 to 35 GeV/u is due to the fact that the pion multiplicity increases by 27% in the first and only by 13% in the second step.

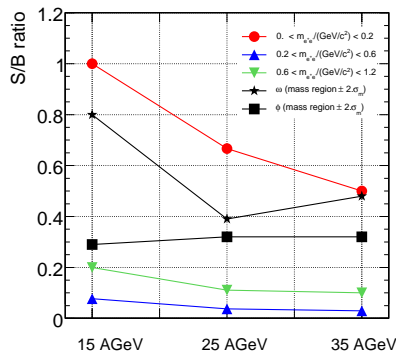


Figure 1: Signal-to-background ratio for central $Au + Au$ collisions at different beam energies after all cuts have been applied

Clear signs of an excess of dileptons above the known decay sources were obtained by the HELIOS/CERES and NA60 Collaborations at SPS energies and by the PHENIX Collaboration at RHIC energies. A clear correlation between the S/B ratio and $dN_{ch}/d\eta$ can be seen. Interestingly,

all experiments so far seem to follow this dependence (see Fig. 2), although the sources of the combinatorial background are very different. The $dN_{ch}/d\eta$ for CBM were taken from Ref. [3]. Thus for central $Au + Au$ collisions at 15 GeV/u beam energy, we expect 250 charged particles per rapidity unit at midrapidity, 300 for $Au + Au$ collisions at 25 GeV/u beam energy, and 350 for $Au + Au$ collisions at 35 GeV/u beam energy. From a parametrization of the published enhancement factors as function of center of mass energy, for CBM we might expect an enhancement factor not smaller than 6. We therefore deduce a S/B ratio of $6 \times 1/9$ for central $Au + Au$ collisions at 15 GeV/u, $6 \times 1/16$ for central $Au + Au$ collisions at 25 GeV/u and $6 \times 1/18$ for central $Au + Au$ collisions at 35 GeV/u ($M_{inv} > 0.2 \text{ GeV}/c^2$). As Fig. 2 demonstrates, this performance is well competitive with previous experiments measuring dileptons in heavy-ion collisions at similar charged track densities.

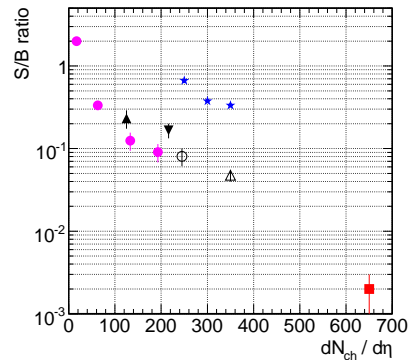


Figure 2: Integrated S/B ratios for M_{inv} larger than $0.2 \text{ GeV}/c^2$ measured by existing dilepton experiments as a function of the number of charged particles in one rapidity unit. Circles: NA60 data for four centrality bins; triangles, open circle: CERES data, square: PHENIX data, star: CBM simulations assuming an enhancement factor of 6.

References

- [1] T. Galatyuk *et al.*, *Strategies for electron pair reconstruction in CBM*, GSI Scientific Report 2005/FAIR-QCD-CBM-06
- [2] CBM Collaboration, *Compressed Baryonic Matter experiment, Technical Status Report*, QCD.CBM-report-2005-001
- [3] A. Andronic, P. Braun-Munzinger, and J. Stachel, *Hadron production in central nucleus-nucleus collisions at chemical freeze-out*, Nucl. Phys. A 772 (2006) 167

Feasibility studies for a J/ψ trigger in the electron-positron decay mode

A. Maevskaya¹, C. Höhne², and A. Kurepin¹

¹INR RAS, Moscow, Russia; ²GSI, Darmstadt, Germany

The investigation of charmonium production in heavy ion collisions is one of the main objectives of the CBM experiment. However, as the J/ψ and Ψ' multiplicities are predicted to be very low, e. g. about $1.92 \cdot 10^{-5}$ for J/ψ and $2.56 \cdot 10^{-7}$ for Ψ' obtained by the HSD model in central Au+Au collisions at 25 AGeV [1], measurements have to be performed with the highest available interaction rates. Fast and efficient on-line event selection based on J/ψ signatures is therefore mandatory in order to reduce the data volume to the recordable rate. Currently, highest interaction rates of 10 MHz and data recording rates of 25 kHz are foreseen; thus, an on-line event suppression by at least a factor of 400 is required. In the here presented study, first steps towards the development of a J/ψ trigger for the e^+e^- decay channel were undertaken. A special software package was developed for performance studies of a J/ψ trigger. The efficiency of event selection based on fast tracking in the STS and particle identification in the TRD is presented in this report.

Figure 1 shows the transverse momentum distributions of electrons from different background sources detected in CBM. It is clear that the simple selection criterium to record only events containing 2 electrons with $p_T > 1$ GeV/c could already considerably reduce the background.

The simulations were performed with an implementation of the standard CBM detector layout with 8 strip stations in the STS and a 250 μm gold target. To test the event selection algorithm, 10^4 central and minimum bias UrQMD events at 25A GeV beam energy were transported through the full CBM set-up. In the event reconstruction, particles are first reconstructed in the Silicon Tracking System

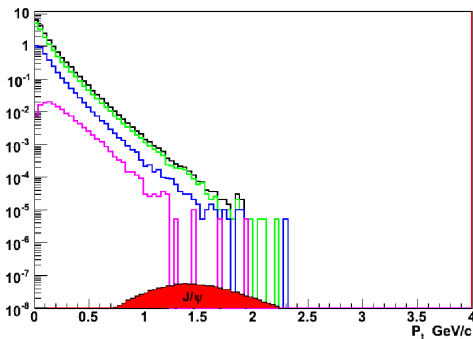


Figure 1: Transverse momentum distribution of electrons and positrons in the CBM-TRD from various sources as calculated with UrQMD for central Au+Au collisions at 25 AGeV beam energy. Black: all electrons; green: γ conversion in the target (250 μm Au); blue: π^0 Dalitz decay; magenta: η Dalitz decay; red: J/ψ calculated with PLUTO assuming $T = 170$ MeV.

placed inside a dipole magnetic field, providing the measurement of momenta. Only tracks with transverse momenta higher than 1 GeV/c were selected as candidates for J/ψ decays to electrons. Vertices of these tracks are not taken into account because all high momentum tracks originate in the target. These selected tracks were extrapolated to TRD and were reconstructed by the LIT TRD tracking package. Pion to electron separation in TRD is provided for high momenta ($p_T > 1$ GeV/c). In this work, MC information on the particle type was used to estimate the event rejection factor depending on the achieved hadron suppression. A track was called “ J/ψ electron candidate” if it was a real MC electron or a hadron chosen statistically according to the selected hadron suppression. An event was selected as “ J/ψ ” event if it had 2 electron candidates without applying any charge selection.

Table 1: Data volume reduction factor for different hadron rejection levels in the TRD

hadron rejection factor	full/selected central	full/selected minbias
100	82	500
200	150	1000
500	2400	5000

Table 1 shows the ratio of the number of generated events to events with 2 “ J/ψ electron candidates” for different hadron suppression factors. With the targeted pion suppression factor of 100 in the TRD, the required on-line event suppression can be reached.

As next steps, the existing TRD electron identification routines based on a statistical analysis of the energy loss spectra will be implemented in the trigger study. First studies show that a comparable event selection can be achieved at no loss of J/ψ efficiency. The proposed trigger algorithm however requires tracking in the STS at 10 MHz interaction rate which poses a high challenge on the tracking algorithms. Fast tracking algorithms are under development [2], but also different online event selection algorithms are under investigation which would be based on TRD information alone.

References

- [1] O. Linnyk et al., Nucl. Phys. A 786 (2007) 183
- [2] H. Bach et al., *Porting a Kalman filter based track fit to NVIDIA CUDA*, this report

Measurement of direct photons via conversions into e^+e^- pairs in CBM

M. Klein-Bösing¹, C. Höhne², F. Uhlig², and J. P. Wessels¹

¹IKP, Münster, Germany; ²GSI, Darmstadt, Germany

In CBM, the ECAL is foreseen to provide photon identification. In addition, a measurement of di-electrons from γ conversions can be used to increase the precision: this method is very auspicious especially at low momenta because of the good momentum resolution of the electron tracking. Moreover, it does not suffer much from misidentified charged and neutral hadron background.

The e^+e^- pairs from γ conversions can be measured with the charged particle tracking (STS and TRD) and electron identification detectors (RICH, TRD, and TOF). They can subsequently be used for photon reconstruction, which is based on a Kalman filter method. Most of the γ conversions (86%) occur in the target and here, the main contamination is caused by e^+e^- pairs from π^0 Dalitz decays.

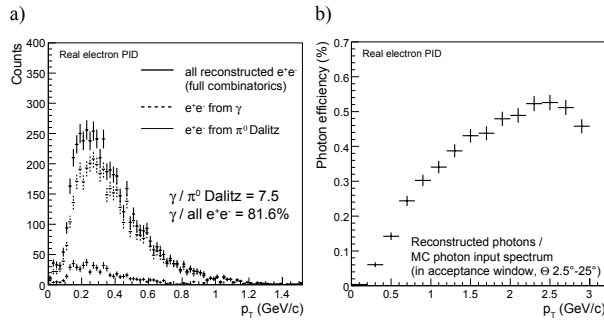


Figure 1: a) p_T distribution of all reconstructed e^+e^- pairs (thick), contribution from γ conversions (dashed), and π^0 Dalitz decays (thin) from 20000 central Au+Au events at 25.4 GeV; b) reconstruction efficiency for γ by conversions into e^+e^- pairs as function of p_T .

In Fig. 1a, the p_T distribution of the reconstructed e^+e^- pairs can be seen after applying cuts to the opening angle ϑ and the invariant mass. With these cuts, the γ/π^0 -Dalitz ratio increases from 4.2 to 7.5, and the fraction of γ mothers to all (true and fake) reconstructed e^+e^- pairs increases from 3.2% to 81.6%. This is the purity of the reconstructed photon signal. In Fig. 1b, the corresponding γ reconstruction efficiency is shown for the condition that two out of three PID detectors have given a positive electron decision. The reconstruction efficiency is determined by the ratio of the number of reconstructed photons to the number of photons in the MC input spectrum. The efficiency decreases towards low p_T because of the smaller PID efficiency and electron acceptance. The difference to the theoretical conversion probability of photons in the gold target (250 μm) of 2.9% is reflected in the losses due to electron/positron acceptance and efficiency.

The momentum resolution of the reconstructed photons

as a function of momentum is flat and below 2.5% for $p < 8$ GeV/c, considerably better than the expected momentum resolution in the ECAL.

The measurement of direct photons requires precise knowledge of the contribution from decays (mainly $\pi^0 \rightarrow \gamma\gamma$) to the inclusive photon spectrum. An enhancement of photons compared to the expectation from hadron decays is attributed to a direct photon signal. The π^0 -signal is determined by an invariant-mass analysis of the reconstructed photon pairs. Considering all possible $\gamma\gamma$ -combinations in addition to the π^0 -signal leads to a large combinatorial background. This background can be determined through *event mixing*: the result obtained by combining particles within one event is compared to the result for particle combinations from different events, which are by definition not correlated.

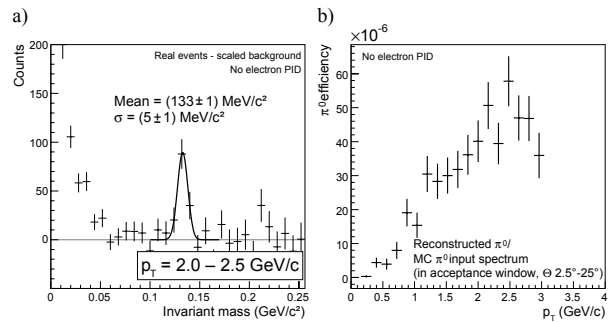


Figure 2: a) Invariant-mass distribution of $\gamma\gamma$ -pairs after background subtraction; b) p_T distribution of the π^0 reconstruction efficiency.

After subtraction of the normalized background, a π^0 -peak can be extracted (see Fig. 2a). Here, no PID conditions are applied in order to increase the statistical accuracy. The RMS of a Gaussian fit to the π^0 -peak is of the order of 5 MeV/c². The efficiency of π^0 reconstruction with photons via conversions is shown in Fig. 2b. The low overall reconstruction efficiency is a consequence of the photon reconstruction efficiency entering squared. In addition, the efficiency decreases towards low p_T because of the larger opening angle for photon pairs, which reduces the geometrical acceptance. Multiplying this efficiency with the π^0 -signal of an UrQMD spectrum (central Au+Au collisions at 25 AGeV), one can deduce that $5 \cdot 10^8$ UrQMD events lead to 100 π^0 s at $p_T = 2$ GeV/c. With an expected data storage rate of 20 kHz in CBM, this would require 7 hours of data taking in order to obtain a π^0 -signal with a statistical error of 7.3%, with decreasing yield towards large p_T .

Muon measurements at different beam energies in CBM

A. Kiseleva¹, C. Höhne¹, E. Kryshen², A. Lebedev¹, and M. Ryzhinskiy³

¹GSI, Darmstadt, Germany; ²PNPI, Gatchina, Russia; ³SPbSPU, St.Petersburg, Russia

The CBM muon detection system is designed to measure muon pairs from the decay of vector mesons (ρ , ω , ϕ , J/ψ) produced in heavy-ion collisions. At FAIR energies, the sensitivity to low-energetic muons is essential for the measurement of low-mass vector mesons. We thus developed a muon detection concept with a dynamical definition of absorber thickness according to the muon momentum. The current design of the muon detector system consists of 6 hadron absorber layers (iron plates of thickness 20, 20, 20, 30, 35, 100 cm) and 15-18 gaseous tracking chambers located in triplets behind each iron slab. The absorber/detector system is placed downstream of the Silicon Tracking System (STS), which determines the particle momentum. The experimental definition of a muon depends on its momentum, which varies with the mass of the vector mesons and with beam energy. As an example, for beam energies above 15 AGeV, muons from the decay of J/ψ mesons have to pass all 6 absorber layers with a total iron thickness of 225 cm, corresponding to 13.4 interaction lengths λ_I . Muons from the decay of low-mass vector mesons (ρ , ω , ϕ) only have to penetrate through 5 iron absorber layers with a total thickness of 125 cm ($7.5 \lambda_I$).

The multiplicity of vector mesons is estimated using the HSD event generator, whereas the dimuon decay kinematics is computed with the PLUTO code. The signals are embedded in a heavy-ion collision background simulated with the UrQMD event generator. Both signal and background tracks are transported through the detector setup using the TGEANT3 code within the CBMROOT simulation framework. The L1 tracking procedure [1] is used for track finding and momentum reconstruction in the STS. LIT tracking [2] is used for track finding in the muon system. Tracks reconstructed in both the STS and the full hadron absorber system are accepted as muons. For the track reconstruction, we assume that the detector layers are segmented into pads according to an occupancy of 5%. The efficiency for vector meson detection and the signal-to-background ratio,

Table 1: Signal-to-background (S/B) ratio and efficiency for vector mesons in central Au+Au collisions at 15, 25 and 35 AGeV

	ρ	ω	ϕ	J/ψ	ψ'
beam energy	S/B ratio				
15 AGeV	0.002	0.08	0.01	3	-
25 AGeV	0.002	0.1	0.03	7	0.09
35 AGeV	0.001	0.09	0.03	11	0.2
	efficiency (%)				
15 AGeV	1.4	1.3	2.2	11.8	-
25 AGeV	1.9	1.9	4.3	16	19
35 AGeV	1.8	3.3	5.4	16	19

calculated in a $\pm 2\sigma$ window around the signal peaks, are presented in Table 1 for Au+Au collisions at 15, 25, and 35 AGeV.

The signal-to-background ratio (S/B) for low-mass vector mesons does not vary significantly with the beam energy, whereas it increases strongly with beam energy for J/ψ mesons because of the steeply rising charm production excitation function close to threshold. The signal efficiency decreases with decreasing beam energy because of muon absorption; muons with momenta below 1.6 GeV/c are stopped in 125 cm of iron. The efficiency for muons from low-mass vector mesons can be improved by accepting tracks as muons which pass only 4 iron absorber layers with a total thickness of 90 cm ("soft muons"). By reconstructing pairs composed of "soft" muons and "hard" muons (which pass 125 cm of iron), the efficiency can be increased by about a factor of 2 without deterioration of the S/B ratio.

We also investigated the possibility to perform muon measurements at beam energies below 10 AGeV. For such low beam energies, we employ two different definitions of muons: tracks which pass at least 3 iron layers (60 cm) and tracks which pass at least 4 iron layers (90 cm). Simulations were performed for ω mesons produced in central Au+Au collisions at 8 AGeV. The resulting signal-to-background ratios and signal efficiencies are S/B = 0.05 and $\epsilon = 1.65$ for 60 cm iron, and S/B = 0.1 and $\epsilon = 0.95$ for 90 cm iron. At low beam energies, the detector acceptance can be improved by reducing the magnetic field. The simulations show that a reduction of the magnetic field by 50% enhances the signal efficiency by up to 22%.

Finally, we performed a simulation of vector mesons in proton-carbon collisions at the maximum SIS100 energy of 30 GeV. The resulting S/B ratios and efficiencies are listed in Table 2 for both the PLUTO and the HSD event generator.

Table 2: Signal-to-background ratio and efficiency for ω and J/ψ mesons in p+C collisions at 30 GeV simulated with HSD and PLUTO

	PLUTO		HSD
	ω	J/ψ	J/ψ
S/B ratio	11	147	115
efficiency (%)	4.3	22.7	13.3

References

- [1] I. Kisel, Nucl. Instr. Meth. Phys. Res. A 566 (2006) 85–88
- [2] A. Lebedev et al, *Track reconstruction in the MUCH and TRD detectors of CBM*, this report

Muon reconstruction at high particle multiplicities in CBM

A. Kiseleva¹, C. Höhne¹, E. Kryshen², A. Lebedev¹, and M. Ryzhinskiy³

¹GSI, Darmstadt, Germany; ²PNPI, Gatchina, Russia; ³SPbSPU, St.Petersburg, Russia

The major technical challenge of muon measurements in CBM is the large hit density of up to 1 hit/cm² per event in the muon tracking chambers after the first iron absorber with 20 cm thickness. According to simulations using the TGEANT3 transport code, about 50% of all hits in these chambers are caused by secondary electrons knocked out of the absorber by the primary particles. The electron hits per event calculated for central Au+Au collisions at 25 AGeV are shown in Fig. 1 for the different muon tracking chambers grouped in triplets. When using the transport codes TGEANT4 and TFLUKA, the multiplicity of secondary electrons is increased by 60% and 80%, respectively, compared to TGEANT3. Because of lack of experimental data, it is unclear which of the results is closer to reality. Therefore, we performed simulations where we artificially increase the number of secondary electrons in order to test the robustness of our track reconstruction algorithms.

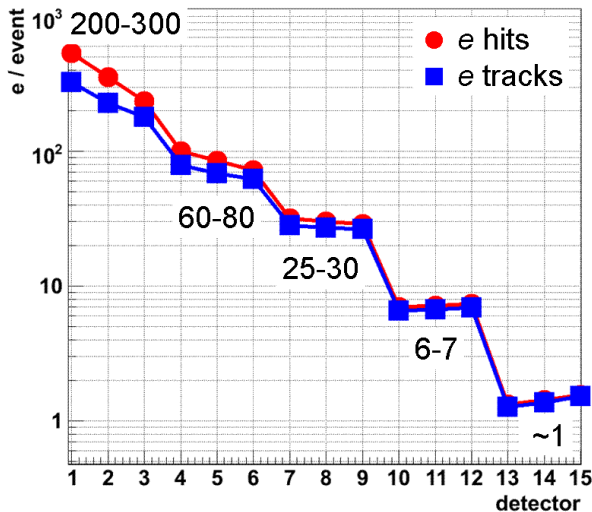


Figure 1: Number of electron hits and tracks in the muon system for central Au+Au collisions at 25 AGeV

Our first approach was to add uncorrelated hits in the tracking chambers. To generate a realistic noise pattern, we randomly produce additional hits according to the distribution of secondary electrons as calculated with TGEANT3. The results of the track reconstruction with additional noise hits are shown in Table 1 for ω mesons in central Au+Au collisions at 25 AGeV. The signal-to-background ratio (S/B) decreases by about 30% when injecting 10 noise hits per secondary electron as calculated with TGEANT3. The increase of hits from secondary electrons by a factor of 10 corresponds to an increase in total multiplicity by a

factor of 5.3. In this case, the ω reconstruction efficiency decreases by almost a factor of 2.

Table 1: Signal-to-background ratio and efficiency for ω mesons in central Au+Au collisions at 25 AGeV without and with up to 10 additional electron hits per secondary electron from TGEANT3

additional hits	0	1	5	10
$N_{hits+noise}/N_{hits}$	1	1.4	3.2	5.3
S/B ratio	0.1	0.09	0.07	0.07
efficiency (%)	1.9	1.6	1.4	1

In reality, hits from secondary electrons in the different muon chambers will be correlated in configuration space. Thus, a second approach is based on the generation of additional electron tracks. According to the simulations with TGEANT3, about 98% of the secondary electrons produced in the absorber have a total momentum of less than 0.5 GeV/c and a transverse momentum of less than 0.2 GeV/c. Using these data as an input for the BOX generator in the CBMROOT framework, we randomly generated up to 10 additional electron tracks for each secondary electron obtained from the transport simulation. The results of this simulation with additional electron tracks are presented in Table 2. The effect on the S/B ratio is similar to the case of uncorrelated hits, but the reconstruction efficiency is less affected. This can be understood since now the additional hits belong to trajectories which can be recognised by the tracking algorithm.

Table 2: Signal-to-background ratio and efficiency for ω mesons in central Au+Au collisions at 25 AGeV without and with up to 10 additional electron tracks per secondary electron from TGEANT3

additional tracks	0	1	5	10
$N_{hits+e_{Box}}/N_{hits}$	1	1.5	3	5.4
S/B ratio	0.1	0.09	0.09	0.06
efficiency (%)	1.9	2	2	1.4

The di-muon trigger for CBM

A. Kiseleva¹, D. Gonzalez Diaz¹, C. Höhne¹, E. Kryshen², and M. Ryzhinskiy³

¹GSI, Darmstadt, Germany; ²PNPI, Gatchina, Russia; ³SPbSPU, St.Petersburg, Russia

High statistics measurements of lepton pairs from the decay of vector mesons (ρ , ω , ϕ , J/ψ) produced in heavy-ion collisions require high reaction rates, and, hence, a selective trigger. The low particle multiplicities behind the hadron absorber of the CBM muon detection system enable the implementation of a fast trigger on muon pairs. The concept is to develop a flexible trigger scheme according to the muon momentum which depends on the mass of the vector meson and on the beam energy. For beam energies above 15 AGeV, we will use only the last 3 muon chambers (MuCH) located behind the full absorber of 225 cm iron for the generation of a charmonium trigger, whereas the trigger on low-mass vector mesons will be derived from hits in the 3 muon tracking chambers in front of the last absorber, i. e. after 125 cm of iron. The trigger generation proceeds via the following steps: (i) selection of events with at least 6 hits in the last (or second last) detector triplet, (ii) calculation of a tracklet by a linear fit of the hit positions, (iii) extrapolation of the tracklet to the vertex and selection of tracks according to the fit parameters (χ^2 and vertex constraint), and (iv) selection of the proper time-of-flight using the RPC-TOF wall (for charmonia). The event selection will be performed on-line by the CBM computer farm based on many-core processors.

The quality of the track extrapolation depends on the position resolution of the muon trigger chambers. Therefore, the trigger performance was investigated for different granularities (version 1: pad size 2.23×8.96 cm², version 2: pad size 2.23×4.48 cm²). In the simulations, we assume a detector efficiency of 100%. The track selection criteria, i. e. the χ^2 of the fit and the x - and z -distributions at $z = z_{\text{target}}$ vary with the pad size. If these selection criteria (“MuCH cut”) are fulfilled, the time-of-flight information is used for final track selection (“ToF cut”). For the ToF detector, we assume a position resolution of 300 μ and a time resolution of 80 ps. The momentum of the particle is calculated from the time-of-flight (assuming a muon mass), and the invariant mass of the muon pair is derived from the momenta and the opening angle of two tracks. Figure 1 shows the distribution of opening angle and invariant mass for the J/ψ signal (left panel) and for the background (right panel). The different shapes of the distributions permit to reduce the background further by a “ToF cut”.

The trigger performance is quantified by the background suppression factor (which is the fraction of minimum bias events which survive the trigger cuts) and by the efficiency for J/ψ mesons which pass the trigger conditions. The background suppression factor and the J/ψ trigger efficiency for minimum bias Au+Au collisions at 25 AGeV are listed in Table 1 for the detector segmentation version 2.

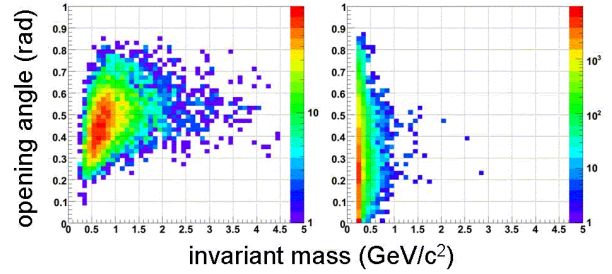


Figure 1: Invariant mass versus opening angle for J/ψ (left panel) and for the background (right panel) calculated for minimum bias Au+Au collisions at 25 AGeV

The background suppression factor decreases by about a factor of 2 if the pad size of the muon detectors is increased by a factor of 2 (segmentation version 1).

Table 1: Background suppression factor for minimum bias Au+Au collisions at 25 AGeV and detection efficiency for J/ψ mesons after different trigger cuts

trigger cuts	no cuts	MuCh	MuCh+ToF
suppression factor	1	606	2222
J/ψ efficiency (%)	20.3	15.2	13.7

The CBM data acquisition system is able to process minimum bias Au+Au collisions up to a reaction rate of 25 kHz without trigger reduction. Hence, the CBM experiment can be operated at the full design luminosity of 10 MHz if the event rate is reduced by a factor of 400. This factor is easily achieved by the dimuon trigger even without time-of-flight selection (see Table 1).

To test the robustness of the trigger concept with respect to additional detector noise, we added 10 hits in each muon chamber of the trigger triplet. Using the “MuCh+ToF” trigger conditions, the background is suppressed by a factor 1923, i. e. the background suppression factor is reduced by only 15 % as compared to the calculations without additional noise.

For low-mass vector mesons, only the selection criteria based on the track quality can be applied (“MuCh cuts”). Because of the high hit density in the detector triplet in front of the last absorber layer, a background suppression factor of only about 20 can be achieved without appreciable loss of signals. This factor would permit to run the CBM experiment with about 500 kHz. Studies are in progress to improve the trigger concept for low-mass vector-mesons.

Development of a trigger algorithm for the measurement of rare probes in the CBM experiment at FAIR

Partha Pratim Bhaduri^{*1}, Subhasis Chattopadhyay¹, Premomoy Ghosh¹, and Bipasha Bowmik²

¹Variable Energy Cyclotron Centre, Kolkata, India; ²Calcutta University, Kolkata, India

Introduction

The planned Compressed Baryonic Matter (CBM) experiment [1] at the upcoming FAIR center at GSI Darmstadt is aiming at the investigation of baryonic matter at high density produced in relativistic heavy-ion collisions. The proposed key observables include the measurement of charmonia, which can be measured via their decay into the dimuon channel [2]. However, the multiplicity of charmonium is extremely small at FAIR energies ($E_L = 10 - 40$ AGeV), which requires extreme interaction rates (up to 10^7 events per second) to have sufficiently good statistics. The foreseen Data Acquisition system (DAQ) will be able to record events at a rate of 25 kHz. In this report, we describe the development of an algorithm for online event selection which rejects the majority of the background events not containing charmonium decays.

Algorithm

The on-line event selection has to be sensitive to muon pairs from charmonium decays. Since our muon detection system is placed outside of the magnetic field, high momentum muons coming from the decay of J/ψ will have an approximately straight trajectory up to the last detector station. The present algorithm is based on the following steps:

1. Search for a hit triplet in the last three muon stations. The members of a triplet should belong to the same straight line. The angular (both polar and azimuthal) information is used for the formation of a triplet.
2. The selected events should have at least two hit triplets, since we are looking for di-muons.
3. The projection of the triplets to the target region (main vertex) using the information from the non-bending plane.

Until now we have implemented the first two steps. A schematic diagram depicting the different steps of the algorithm is shown in fig. 1.

Preliminary results

For the estimation of background suppression factors, we have considered central and minimum bias UrQMD events. The signal reconstruction efficiencies have been calculated employing the PLUTO generator (generating the phase space of the J/ψ decay) embedded in a background generated by UrQMD. The suppressions obtained by applying the criteria 1 and 2 from above are 375 and 65 for

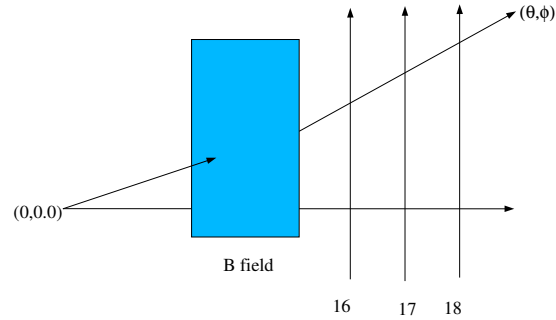


Figure 1: Schematic of the trigger logic for selection of rare events

minimum bias and central events, respectively, with relatively larger error for central events. The suppression factor obtained for minimum bias events is close to the value which is necessary to arrive at the archival bandwidth.

An estimation of the J/ψ reconstruction efficiency shows that with the application of the trigger algorithm, the efficiency in central events is reduced from 18% to 5.4%. We are working on improving the performance of the algorithm by (i) optimising the criteria for event selection and (ii) finding new criteria based on informations from other stations.

Summary

Muons are a potential candidate for the measurement of observables like low-mass vector mesons and charmonia. Due to their extremely low production rate at CBM energies, very high event rates are required for their measurement with a well defined statistics. An algorithm to filter out the rare events is under development in order to suppress the background events as much as possible without reducing the signal reconstruction efficiency. The algorithm is being optimized to achieve yet higher suppression rates.

References

- [1] P. Senger, J. Phys. G: Nucl. Part. Phys. 31 (2005) S1111-S1114
- [2] A. Kiseleva, P. P. Bhaduri et al., Proceedings of Quark Matter 2008, to be published in Indian Journal of Physics

* partha.bhaduri@veccal.ernet.in

Feasibility study of $\eta \rightarrow \gamma\gamma$ reconstruction with ECAL

S.M. Kiselev

ITEP, Moscow, Russia

Simulations with the CbmRoot package (AUG07 version with the fast ECAL option) of 10^5 UrQMD central Au+Au events at 15A, 25A, and 35A GeV beam energy were performed. The ring part of ECAL, $9^\circ < \theta_{lab} < 20^\circ$, located at 12 m from the target was analyzed. It corresponds to the central rapidity region covering in the c.m.s. $\theta_{c.m.s.} = 50^\circ - 90^\circ$, $60^\circ - 105^\circ$ and $70^\circ - 115^\circ$ for 15A, 25A and 35A GeV, respectively. Photons entering the ECAL with $p > 0.3$ GeV/c were used for the analysis. Ideal ECAL reconstruction was assumed (the full ECAL reconstruction is in progress).

The origin of photons weakly depends on the beam energy: about 85% are from π^0 decays, 10% from e^\pm conversions, and 3% from η decays. At 25A GeV, out of 12 primary η per event only ~ 0.5 photon pairs reach the ECAL ring because of the $\eta \rightarrow \gamma\gamma$ branching ratio (40%) and acceptance (10%).

Three values for the ECAL energy resolution, namely $3\%/\sqrt{E}$, $6\%/\sqrt{E}$ and $9\%/\sqrt{E}$, were chosen to demonstrate the sensitivity of the results to this parameter. The coordinate resolution due to the finite cell size (6×6 cm²) was neglected.

As an example (all results are presented in [1]), Fig. 1 shows the invariant-mass spectrum for the signal and background photon pairs at 25A GeV beam energy and $6\%/\sqrt{E}$ energy resolution. The $\eta \rightarrow \gamma\gamma$ signal is about 1000 times lower than the background. S/B ratios and significances are presented in Table 1 for different beam energies and assumptions on the ECAL resolution. The S/B ratio is of the order of 10^{-3} ; it decreases with increasing energy resolution and with increasing beam energy because of the increasing multiplicity (110, 156, and 185 photons in the

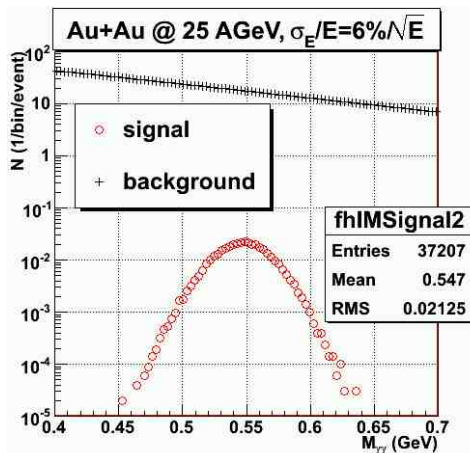


Figure 1: Invariant-mass distributions of two photons for central Au+Au events at 25A GeV

Table 1: Signal-to-background ratios and significances (in brackets) in the $\pm 2\sigma$ region for different beam energies and ECAL resolutions

σ_E/E	$3\%/\sqrt{E}$	$6\%/\sqrt{E}$	$9\%/\sqrt{E}$
15 AGeV	0.19 (7.1)	0.10 (5.1)	0.07 (4.2)
25 AGeV	0.14 (6.9)	0.07 (4.9)	0.04 (4.0)
35 AGeV	0.11 (6.8)	0.05 (4.7)	0.04 (3.9)

ECAL ring for 15A, 25A, and 35A GeV, respectively). The dependences on p_t and beam energy, assuming an ECAL resolution of $6\%/\sqrt{E}$, are given in Table 2. The S/B ratio increases with p_t , reaching up to ~ 0.2 -0.3%. In order to reach a significance level of 10 at high p_t , the event statistics must be increased by two orders of magnitude, i. e. to 10^7 events.

The current estimate of S/B agrees with previous ones obtained for the two-arm ECAL setup [2]. It should be noted that the WA98 collaboration, using the mixed event technique, observed an η signal in 7.7×10^6 central Pb+Pb events at 158A GeV [3], with a S/B ratio of about 0.3% at $1.0 < p_t < 1.2$ GeV/c. The extrapolation of our estimate to the SPS energy yields a lower value. However, it must be taken into account that the UrQMD generator overestimates the pion multiplicity and, as a consequence, the combinatorial background.

In a next step, the analysis will be repeated using simulations with the full ECAL option and real ECAL reconstruction procedures.

Table 2: Signal-to-background ratios and significances (in brackets) in the $\pm 2\sigma$ region for different p_t and beam energies, assuming an ECAL resolution of $6\%/\sqrt{E}$

p_t [GeV/c]	0.4-0.8	0.8-1.2	1.2-1.6
15 AGeV	0.11 (3.5)	0.19 (2.1)	0.33 (1.1)
25 AGeV	0.08 (3.4)	0.13 (2.2)	0.23 (1.3)
35 AGeV	0.06 (3.3)	0.11 (2.2)	0.18 (1.3)

References

- [1] S. M. Kiselev, 12th CBM collaboration meeting, October 2008, Dubna, <http://cbm2008-oct.jinr.ru/presentations/cbm.php>
- [2] S. M. Kiselev, 10th CBM collaboration meeting, September 2007, Dresden, <https://www.fzd.de/workshops/CBM/program.html>
S. M. Kiselev, CBM Progress Report 2007, GSI, Darmstadt 2008, p. 28a
- [3] M. M. Aggarwal *et al.*, (WA98), Phys. Rev. Lett. **85** (2000) 3595

Study of hadron azimuthal correlations with CBM

V. Pozdnyakov and Yu. Vertogradova

JINR, Dubna, Russia

The analysis of collective phenomena in heavy-ion interactions can be used to constrain the equation of state of the nuclear matter [1]. The spacial anisotropy of interacted volumes of nuclei formed in mid-central collisions and scattering of produced particles during the system evolution both convert to the spacial hadron anisotropy with respect to the so-called 'reaction plane' (RP) determined by the axis of the ion collisions and the line of the impact parameter. The observation of this in-plane transverse collective motion ('flow') can be interpreted as hydrodynamical effects in the compressed nuclear matter [2]. The Fourier decomposition of the azimuthal distributions of the produced particles (ϕ_p) with respect to the reaction plane (ϕ_{RP}), brings to the flow components expressed in terms of the Fourier coefficients [3] with the variables $v_i \equiv \langle \cos[i \cdot (\phi_p - \phi_{RP})] \rangle$ being called directed ($i=1$) and elliptic ($i=2$) flows.

The study of the flow(s) requires the determination of event centrality and reaction plane angle. A high-precision tracking system (STS) and a forward calorimeter (PSD) to register projectile spectators are the main devices to both determine the centrality and reconstruct the reaction plane.

The analysis¹ presented below was performed on UrQMD Au+Au events at 25 GeV per nucleon, which were transported through the CBM setup (production AUG07). The PSD was located at 15 meters from the target and it was considered as a ring with a radius of 60 cm. A particle entering PSD was considered to be fully absorbed in the detector, providing a detector response for this particle. Such a simplified consideration will allow us to calculate the experimental reaction plane resolution as a function of different $R\phi$ segmentations of the detector.

The number of the charged particles reconstructed in the STS and the total energy deposition in PSD were used to determine the centrality. The correlation between these two observables allows to select centrality domains as demonstrated in fig. 1, where they are denoted by the percentage of the total ion-ion cross section. The expected behaviour of the directed and elliptic flows for mid-central events is shown in [4].

The main device to reconstruct the event plane (EP , denotes an experimental estimator of RP) is the PSD calorimeter. Different PSD segmentations in the $R\phi$ -plane were considered to calculate the accuracy of the RP reconstruction. The relationship between the variable v_n measured in the experiment and the true one looks like $v_{n,measured} = v_{n,true} \langle \cos[n \cdot (\phi_{EP} - \phi_{RP})] \rangle$, where the cosine is the correction factor. Its behaviour is shown in fig. 2 as a function of the collision impact parameter.

In conclusion, the CBM setup is well suitable to study

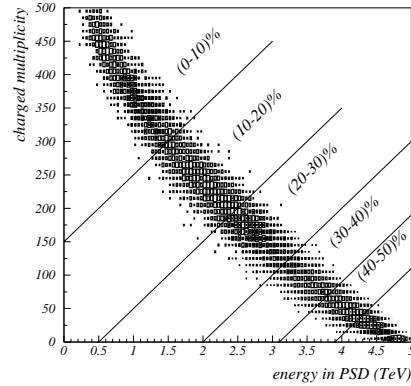


Figure 1: Distribution of the multiplicity of charged particles reconstructed in STS vs. the energy deposited in PSD

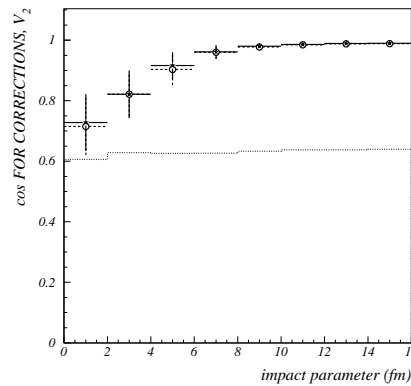


Figure 2: Value of $\langle \cos[2 \cdot (\phi_{EP} - \phi_{RP})] \rangle$ as a function of the ion-ion impact parameter for 3 (hist), 10 (open circle) and 17 (stars) PSD segmentations

azimuthal correlations. The analysis of the information from the zero degree calorimeter PSD together with the charged particles reconstructed in STS allows to select mid-central events. The segmentation of the PSD into more than ten parts will allow to reconstruct the reaction plane of ion-ion collisions with sufficiently high accuracy.

References

- [1] C. A. Ogilvie *et al.*, Phys. Rev. C 42 (1990) R10
- [2] H. H. Gutbrod *et al.*, Rep. Prog. Phys. 52 (1989) 1267
- [3] S. Voloshin and Y. Zhang, Z. Phys. C 70 (1996) 665
- [4] V. Pozdnyakov and Yu. Vertogradova, CBM-PHYS-note-2008-001 (2008)

¹Details of the analysis can be found in [4].

CBM radiation levels studies

D. Bertini¹ and E. Paulova¹

¹GSI, Darmstadt, Germany

The CBM experiment focuses on detecting extreme conditions produced in heavy ions collisions by observing rare probes such as charmonium particles. The achievement of this goal depends on collecting high statistics data which requires extreme collision rates of up to 10^7 minimum bias Au+Au events per second on a 1 % radiation length target during 2 months operation time per year.

The radiation environment produced by such high interaction rates may pose severe constraints on the operation of detectors and electronics in the CBM cave. Its precise knowledge is thus a prerequisite for the design of the CBM detector system.

The radiation simulations were run with the FLUKA package [1]. A simplified CBM geometry including major materials and the surrounding cavern has been implemented using a Combinatorial Geometry in terms of bodies and regions (see fig. 1). 200k UrQMD minimum bias Au + Au collisions at 25 AGeV were injected into FLUKA which transported the produced particles in this geometry. Both the total ionising dose and the fluence were recorded on a 3-dimensional mesh as well as in the planes of the different detectors.

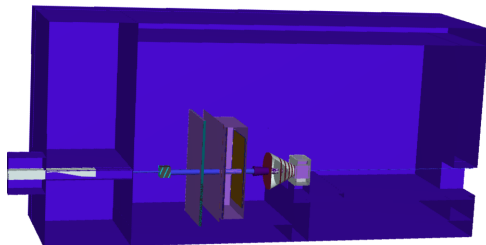


Figure 1: Implementation of the CBM cave in FLUKA

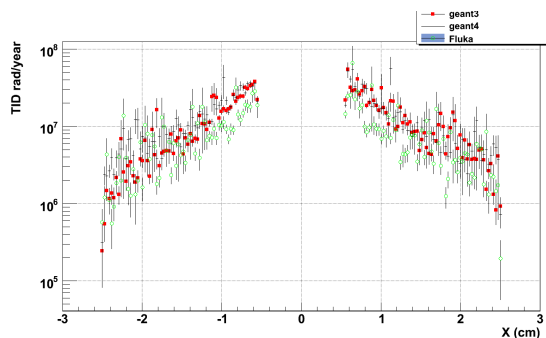


Figure 2: Comparison of the total ionising dose at the first MVD station ($z=5$ cm) obtained with different Monte-Carlo engines

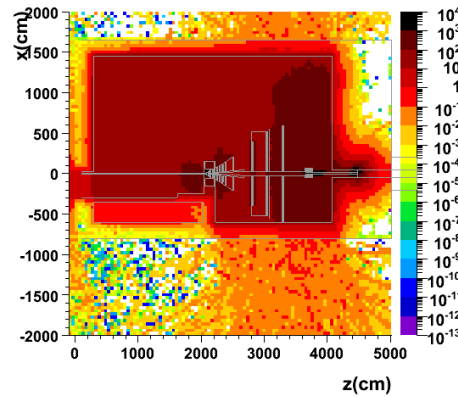


Figure 3: Total ionizing dose in the CBM Cave in rad per year

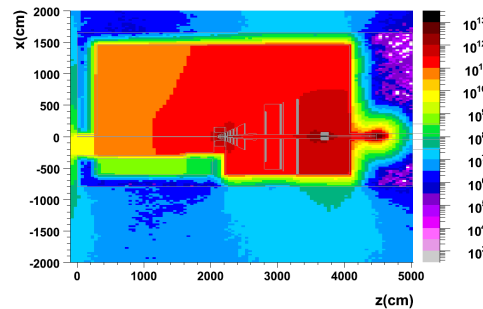


Figure 4: Fluence in the CBM Cave in 1 MeV $n_{eq}/cm^2/year$

All results obtained with FLUKA have been cross-checked with other Monte Carlo transport codes such as Geant3 or Geant4 using the FairRoot simulation environment [2]. Figure 2 shows such a comparison for the total ionizing dose cumulated at the first vertex detector plane situated at 5 cm from the target.

The results for both the total ionising dose and the fluence in the CBM cave per run year are shown in figs. 3 and 4, respectively. Global as well as local diagnoses are documented in detail on the CBM web space [3].

References

- [1] A. Fasso, A. Ferrari, J. Ranft and P. R. Sala, "FLUKA, a multi-particle transport code", CERN-2005-10(2005), INFN/TC-05/11, SLAC-R-773 FLUKA, and references therein.
- [2] <http://fairroot.gsi.de>
- [3] <http://cbm-wiki.gsi.de>

Status of the FairRoot simulation and analysis framework

M. Al-Turany¹ and F. Uhlig¹

¹GSI, Darmstadt, Germany

Introduction

The FairRoot framework [1, 2], is an object-oriented simulation, reconstruction and data analysis framework based on ROOT [3], and the Virtual Monte-Carlo (VMC) interface [4]. It includes core services for detector simulations and offline analysis.

Event Display

The event display in FairRoot is based on the Eve (Event Visualization Environment) package in ROOT [3]. Combined with trajectory visualization in FairRoot, the event display can be used directly from the macro to display TGeoTracks (MC Tracks), Monte Carlo points, and hits, together with the detector geometry. The FairEventManager implemented in FairRoot delivers an easy way to navigate through the event tree and to make cuts on e. g. energy, p_t , or particle PDG in user events. However, the drawback of this ansatz is that the tracks have to contain some visualization information in order to be displayed. In the following, we describe a solution where the track information is created at visualization level without the need to store track information during the simulation. This is achieved using Geane.

Geane

GEANE [5, 6] is a package to calculate the average trajectories of particles through dense materials and to calculate the transport matrix as well as the propagated covariance matrix in a given track representation. GEANE was fully integrated in FairRoot as a package. The framework defines the basic classes relevant for track following, i. e. configuration, geometry description (from the Monte Carlo, parameters files), and the magnetic field map definition. The exact geometry and field used in the simulation can be taken into account by the track follower.

Event Display with Geane as track propagator

The fact that both Eve and Geane use the ROOT geometry description for the detector geometry makes it natural to integrate Geane as a track propagator for the event display. With this integration, reconstructed tracks and/or Monte-Carlo tracks can be visualized with good accuracy. The main advantage of this integration is that any set of reconstructed or simulated tracks can be visualized without the need of special visualization modes. Moreover, only selected tracks will be propagated on the fly which enhances the performance of the display. Figure 1 shows a schematic

diagram of the interface to Geane. An example of the event display is shown in fig. 2.

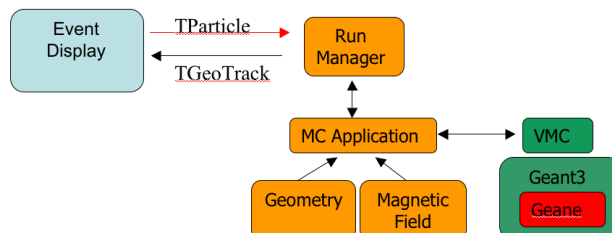


Figure 1: Event Display and Geane

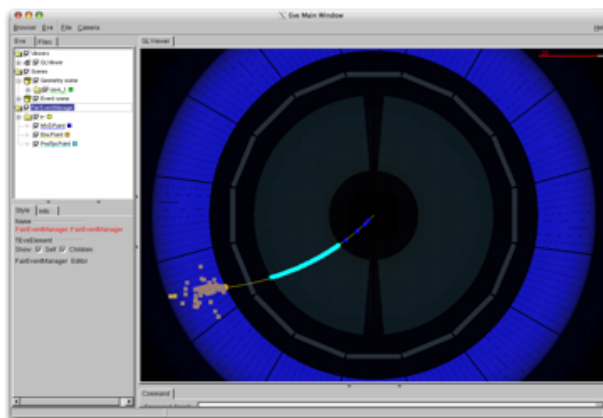


Figure 2: Event display example: Panda inner tracker and EMC

References

- [1] <http://fairroot.gsi.de>
- [2] D. Bertini et al., J. Phys. Conf. Ser. 119 (2008) 032011
- [3] R. Brun and F. Rademakers, Nucl. Instr. Meth. Phys. Res. A 389 (1997) 81
- [4] R. Brun et al., *Virtual Monte-Carlo*, in *Computing in High Energy and Nuclear Physics*, La Jolla, California, 2003, p. 24–28
- [5] V. Innocente, M. Maire, and E. Nagy, *GEANE: Average Tracking and Error Propagation Package*, CERN, Geneva, 1994
- [6] A. Fontana et al., J. Phys. Conf. Ser. 119 (2008) 032018

Grid setup for CBM

M. Al-Turany, K. Schwarz, and F. Uhlig

GSI, Darmstadt, Germany

The Compressed Baryonic Matter Experiment [1, 2] will have to cope with about 5 PB of raw data per run year. It is not likely that storage, reconstruction and analysis of this amount of data will be performed at a single dedicated computing center. A possible computing model for CBM is a global computational grid, in which computing and storage capacities will be supplied by a network of worldwide distributed computing centers.

AliEn

The Grid software AliEn [3], developed by the ALICE experiment was chosen as flexible middleware for the secure and coordinated access to the worldwide distributed computing resources. AliEn is a lightweight and simple Grid environment build on top of existing open source software. This includes the latest Internet standards for information exchange and authentication. To choose AliEn out of many available Grid flavors has some pragmatic reasons. One of the most important is the expertise of the GSI IT department with AliEn due to the operation of an ALICE tier2 center at GSI. Moreover, the PANDA experiment [4], using the same software framework, FairRoot, as CBM, has already successfully tested AliEn. This preparatory work enabled us to setup the CBM Grid within 3 months with only limited manpower.

The heart of the Grid implementation of CBM is the central installation of the CBM Virtual Organization at GSI. These central services consist of the LDAP database which holds organizational data like information about hard- and software of the participating sites, people and their roles, and many more. The information about the virtual file space used to organize the data inside of AliEn is stored in a MySQL database. This database includes information about e. g. running jobs and the file catalogue. The file catalogue provides the mapping between the Physical File Name (PFN) on some storage element to the Logical File Name (LFN) used inside AliEn. Besides these two main parts, there are several other services dedicated e. g. for optimization of the file catalogue, optimization of the job submission, or user authentication. For monitoring purposes, we use the MonaLisa package [5], with the server also running at GSI.

Since the AliEn software is only provided for Scientific Linux, one of the main tasks during the installation procedure was to port the complete software to Debian.

On each site (computing center) there are several services for the communication with the central services on one hand and the real computing environment on the other hand. These are for example the Computing Element (CE) which is the interface to the local batch system (LSF, PBS,

BQS, DQS, Globus, Condor), or the SE (Storage Element) which is the interface to the local storage. The first and at present only site is GSI. Here, the CE is the front-end to the local LSF batch system, and the SE stores the data via *xrootd* [6] on the lustre [7] file system.

First results

To study the behavior of the AliEn environment and the interplay between the site services and the central services, in a first step after the installation of the central services, a stand-alone virtual site on a single computer has been installed. This computer executed the jobs locally and also used only the local hard-disk as storage. Only after the successful test of this test-bed, the GSI Grid site has been set up. By end of December 2008, the complete system was in a state that the first real test of the CBM Grid environment could start. Since there was urgent need for a large-scale (100,000 Events) simulation and reconstruction with the complete experimental detector setup including the computationally consumptive electromagnetic calorimeter, we choose this configuration as our first real production run. To make use of the batch farm system, the dataset was subdivided into 100 jobs with 1,000 events each. The run time per job was about 48 hours. After 4 days, all jobs finished successfully, and 0.5 TB were stored on the lustre file system. These data are now available for further analysis.

In conclusion, the Grid software AliEn was successfully ported to Debian. The central and the site services were installed at GSI and successfully tested in a production run. In the near future, other sites will be included into the CBM Virtual Organization. First steps to connect the Laboratory of Information Technology (LIT) of JINR, Dubna, have already been taken. In addition, CBM users will have to be trained for the usage of the CBM Grid facilities, which will be achieved by online documentation as well as by workshops with hands-on exercises.

References

- [1] <http://www-cbm.gsi.de>
- [2] C. Höhne, *The CBM experiment at FAIR – exploring the QCD phase diagram at high net baryon densities*, Int. J. Mod. Phys. E 16 (2007) 2419
- [3] <http://alien.cern.ch>
- [4] <http://www.gsi.de/panda>
- [5] <http://monalisa.cern.ch/monalisa.html>
- [6] <http://project-arda-dev.web.cern.ch/project-arda-dev/xrootd/site/index.html>
- [7] <http://www.lustre.org>

Cellular automaton track finder in a realistic STS detector geometry

D. Golubkov¹, R. Karabowicz², I. Kisel^{*2,3}, I. Rostovtseva¹, and Yu. Zaitsev¹

¹ITEP, Institute for Theoretical and Experimental Physics, Russia; ²GSI, Darmstadt, Germany; ³KIP, University of Heidelberg, Germany

The cellular automaton (CA) based track finder of the CBM experiment [1, 2] is a flexible algorithm operating on space-points, which makes it maximally independent of the actual geometry of the STS detector. Nevertheless, the requirements on the speed and accuracy of the algorithm due to its application at the trigger level force to optimize and continually adjust the algorithm to the changing geometry of the STS detector and sometimes even influence the choice of the detector configuration.

Following the recent developments of the STS detector, several important modifications have been implemented in the CA track finder:

1. Change of the detector geometry from a single-layer one to the geometry with overlapping sensors;
2. adaptation to various updates of the STS digitization which include realistic detector response and clusterization;
3. making the algorithm independent of the number of stations;
4. support for different stereo-angles of the strips located on the front and back-planes of the STS sensors.

The largest amount of modifications to the algorithm and the most detailed studies were dedicated to the introduction of the geometry with overlapping sensors since the required changes were related to the procedure of extrapolation through an inhomogeneous magnetic field, which is the most computationally expensive part of the algorithm.

In the original geometry, all hits in a station had the same position Z_{station} , and the track candidates were extrapolated between the centers of the stations. The more realistic geometry with overlapping sensors has 8 sensors located at different Z positions in each station (with a typical distance in Z between the sensor and the center of the station of $\Delta Z \leq 0.25$ cm). Using the unmodified algorithm with such a geometry results in an efficiency loss of $\sim 20\%$. On the other hand, a straightforward solution involving extrapolation through an inhomogeneous magnetic field to each sensor would be too computationally expensive. Therefore, the task was split in two separate steps:

- Extrapolation of the track candidate to the center of the station Z_{station} ;
- linear extrapolation of the track candidate to Z_{hit} inside the station, $\Delta Z \leq 0.25$ cm.

The described modifications were implemented throughout the algorithm in both the tracklet construction and in the Kalman Filter track fit. After the modification, the CA track finder recovered the high efficiency and speed for the STS geometry with overlapping sensors.

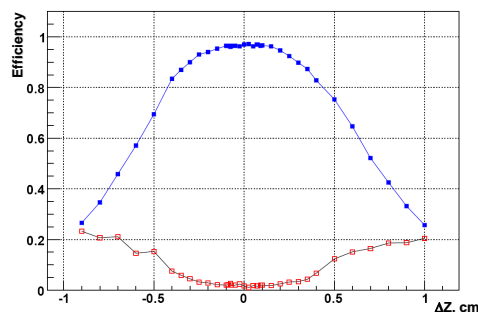


Figure 1: Track finding efficiency for fast primary tracks (filled squares) and ghost fraction (open squares) versus the distance of the linear extrapolation ΔZ

The validity of the linear extrapolation step has been further investigated in detail. Neglecting energy loss, multiple scattering, and magnetic field variation inside a station, an estimate of the accuracy of the linear extrapolation depending on the field strength and track momentum was obtained. Fig. 1 shows the track finding efficiency as a function of the distance of the linear step of the extrapolation inside a station. The results were obtained using an MC sample of central Au+Au collisions at 25 AGeV and demonstrate that the linear extrapolation is valid without losses of efficiency up to the distances of $\Delta Z \sim 0.2$ cm [3].

All mentioned modifications have been included in the CBMROOT framework of the CBM experiment. Both the STS detector geometry and the digitization scheme are still under development, which will require further adaptation of the CA track finder. Currently, we also investigate the parallelization of the CA algorithm and its behavior depending on the smoothness of the magnetic field.

References

- [1] Compressed Baryonic Matter Experiment, *Technical Status Report*, Darmstadt, 2005, <http://www.gsi.de/documents/DOC-2005-Feb-447.html>
- [2] I. Kisel, Nucl. Instr. Meth. Phys. Res. A 566 (2006) 85–88
- [3] I. Kisel and I. Rostovtseva, *Study of L1 CA track finder with new STS geometry and possibilities of parallel computing*, 12th CBM collaboration meeting, Dubna, 14 October 2008

*I.Kisel@gsi.de

Scalability of a Kalman filter based track fit on Intel many-core CPUs

H. Bjerke¹, S. Gorbunov², I. Kisel^{*2,3}, V. Lindenstruth², P. Post⁴, and R. Ratering⁴

¹CERN, Geneva, Switzerland; ²KIP, University of Heidelberg, Germany; ³GSI, Darmstadt, Germany; ⁴Intel, Cologne, Germany

As a result of increasing density of transistors and heat and power constraints, computers increasingly implement parallelism in hardware in order to speedup computation. This has manifested itself in multi-core processors and wider vector instructions. Future computer architectures are expected to increase parallelism in both dimensions.

There are many strategies for extracting parallelism from a workload or a set of workloads. Popular taxonomies for parallel computing are Multiple Instructions Multiple Data (MIMD), Multiple Instructions Single Data (MISD), Single Instruction Multiple Data (SIMD), and Single Instruction Single Data (SISD).

The feasibility of a strategy depends on the characteristics of the parallelism exhibited by the algorithm and its data-structures. Also, the forward scalability of a strategy depends on the level of parallelism given by it and its constraints. Programs that exhibit data level parallelism can often be characterized as forward scalable, although the degree of parallelism in the data can put a constraint on the scalability. Parallelizing with an SIMD model alleviates the constraint of shared resources, but adds the constraint of synchronization. Finally, parallelizing any program usually also adds a new set of constraints intrinsic to the problem, which also has to be taken into account.

Table 1: Speed-up of the Kalman filter based fit on the Xeon 5140 (Woodcrest) at 2.4 GHz using icc 9.1

Type	Time/track, μ s	Speed-up
Scalar double	2.6	–
Vector double	1.6	1.6
Vector single	0.7	2.3

A Kalman filter based track fit of the CBM experiment has shown to be a well suitable benchmark for parallelizing the algorithms of data reconstruction in high-energy physics [1]. It is therefore important to investigate its scalability and the usage of Intel many-core architectures for the Kalman filter based algorithms.

Table 1 shows that a total speedup of 3.7 is reached when changing the data representation from the scalar double precision to the vector (SIMD) single precision. As demonstrated in Fig. 1, a maximum speedup of 30 is reached on the Xeon 5345 (Clovertown) when running 16 threads of the SIMD version of the Kalman filter tracking routine in parallel. The real-time performance of the multi-

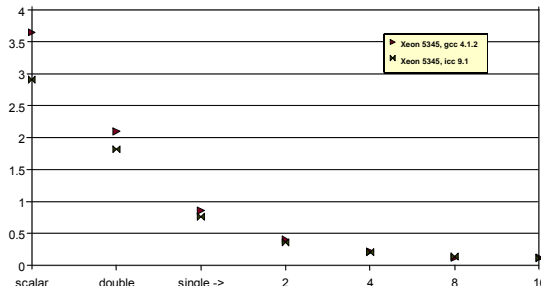


Figure 1: Real-time performance of the Kalman filter based fitting routine per track fitted on the Xeon 5345 (Clovertown) at 2.4 GHz

threaded SIMD Kalman filter benchmark on different Intel CPU platforms is shown in Table 2.

Table 2: Real-time performance of the multi-threaded SIMD Kalman filter based fitting routine per track fitted on different Intel CPU platforms

Type	Cores	Clock, GHz	Time/track, μ s
Core 2	2	2.66	0.26
Core i7	4	3.2	0.1

In addition to multi-core CPU architectures, a many-core architecture code named Larrabee [2] can be considered an interesting platform to further scale the Kalman filter based tracking code in the threading and vectorization dimensions. Larrabee uses multiple in-order x86 CPU cores that are augmented by a wide vector processor unit as well as by some fixed-function logic blocks. This provides dramatically higher performance per watt and per unit of area than out-of-order CPUs on highly parallel workloads. It also greatly increases the flexibility and programmability of the architecture as compared to standard GPUs.

Less architecture-dependent programming frameworks, such as OpenCL and Intel Ct, may also better support future changes in architecture.

References

- [1] S. Gorbunov et al., *Comp. Phys. Comm.* 178 (2008) 374–383
- [2] L. Seiler et al., *Larrabee: a many-core x86 architecture for visual computing*, *ACM Transactions on Graphics*, Vol. 27, No. 3 (2008)

*I.Kisel@gsi.de

Porting a Kalman filter based track fit to NVIDIA CUDA

M. Bach¹, S. Gorbunov¹, I. Kisel^{*1,2}, V. Lindenstruth¹, and U. Kebschull¹

¹KIP, University of Heidelberg, Germany; ²GSI, Darmstadt, Germany

Finding particle trajectories is usually the most time-consuming part of modern experiments in high-energy physics. In many present experiments with high track densities and complicated event topologies, a Kalman filter based track fit is used already at this combinatorial part of the event reconstruction. Therefore, speed of the track fitting algorithm becomes very important for the total processing time.

In 2007, a Kalman filter based track fitting algorithm of the CBM experiment [1] was ported to SSE and the Cell SPE [2]. On the CPU, a speed-up of 10,000 compared to the initial version was achieved. To gain this speedup, two major changes to the existing Kalman filter implementation were done. The magnetic field map was replaced by a functional approximation based on fourth order polynomials. In addition, the algorithm was tuned to work with single precision calculations only, without the need for compensating computations or numerical instabilities.

Today, CPUs are no longer able to increase their peak performance by increasing clock speeds. Modern GPUs, however, continue to increase their peak performance utilising manycore architectures, with NVIDIA GT200 based GPUs nearly reaching 1 TFlop/s in single precision [3]. Thus, they are a promising candidate for further acceleration of the algorithm.

This performance comes at a cost. In contrast to the situation on CPUs, access to the main memory is not cached. All threads running on one multiprocessor, which is similar to a core of a GPU, share a small 16 kB processor local storage called shared memory, which needs to be explicitly programmed. To compensate for that, each multiprocessor has a large register file of 16,384 registers and can have 1024 threads concurrently active. On eight ALUs, it processes warps of 32 threads in 4 cycles, switching between warps without costs, allowing to hide memory accesses by calculations. A GT200 chip contains 30 of these multiprocessors.

In contrast to single instruction multiple data (SIMD) based architectures, NVIDIA GPUs are based on a single instruction multiple threads (SIMT) model, which means that each ALU is connected with its own instruction counter. Therefore, the algorithm needs to be parallelized on a thread level instead of SIMDization. While in the SIMD case, we have one thread that works on a vector of numbers, in SIMT we have multiple threads working on scalars. However, in both cases a number of arithmetic units is fed by the same instruction decoder, making it important for the code not to rely on different code branches depending on the data of each thread.

The original port relied on operator overloading to have only one implementation of the algorithm for multiple platforms. To accommodate for the SIMT nature of the GPU, instead of a vector type the scalar type `float` is now the basis of the algorithm.

The implementation of the algorithm requires 91 registers, reducing the maximum amount of threads that fit into one multiprocessor to 160. This makes it difficult to hide memory access by calculations. Therefore, access to the memory was minimized by storing the parameters for the magnetic field in the small cached constant memory of the GPU. The track and hit data are explicitly transferred to shared memory and back using cooperation between threads executing in one warp for optimal memory transfer speed.

Table 1: Real-time performance of the SIMDized version of the Kalman filter based fitting routine for a single track

NVIDIA Unit	Clock, GHz	Throughput, 10 ⁶ tr/s
8800 GTS 512	1.6	13.0
GTX 280	1.3	21.7

In Tab. 1, the performance for computations located solely in the local caches and storages is shown [4]. Keeping in mind the slow clock, the GPU can show how well it can profit from the high parallelism of the track fitting problem. While its latency for a single track is at a comfortable 44 μ s, it profits from calculating 960 instead of four tracks in parallel. This way, the performance peaks at a rate of 21.7×10^6 tracks/s. Fitting larger datasets located in the GPU's main memory, the NVIDIA GTX 280 is still able to process tracks at a rate of 9.6×10^6 tracks/s.

References

- [1] Compressed Baryonic Matter Experiment, *Technical Status Report*, Darmstadt, 2005, <http://www.gsi.de/documents/DOC-2005-Feb-447.html>
- [2] S. Gorbunov et al., *Comp. Phys. Comm.* 178 (2008) 374–383
- [3] NVIDIA, *NVIDIA CUDA programming guide*, version 2.1, 2008
- [4] M. Bach, *Utilization of Graphics Processing Units in Applications for High Energy Physics*, Diploma Thesis, University of Heidelberg, 2009

*I.Kisel@gsi.de

A standalone package for on-line event selection in the CBM experiment

I. Kisel^{*1,2}, I. Kulakov³, and I. Vassiliev^{1,2}

¹GSI, Darmstadt, Germany; ²KIP, University of Heidelberg, Germany; ³University of Kyiv, Ukraine

One of the most challenging tasks of the CBM experiment [1] is the on-line identification of D mesons [2] at input rates up to 10 MHz. In order to investigate the feasibility of such an on-line selection, a package of reconstruction and selection procedures has been implemented (Fig. 1). It includes a cellular automaton based track finder [3], a Kalman filter based track fitter [4] (both are SIMDized), a primary vertex finder, a procedure for finding short-lived decayed particles (both are implemented within the KF Particle package [5]), and a procedure for selecting charm track candidates. These routines exist already in the CBMROOT framework, but in order to develop and test the full selection chain on different modern and future CPU/GPU architectures, they have been substantially modified and re-organized into a standalone package. Input data consist of detector geometry, simulated data in form of registered hits, and Monte Carlo tracks for performance evaluation. Each part of data is stored in a separate text file produced with a special routine.

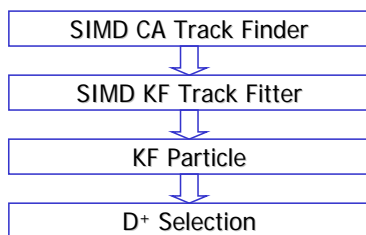


Figure 1: D⁺ selection chain

The total reconstruction efficiency for all tracks is about 92% (see Fig. 2). The reconstruction efficiency clearly depends on the particle momentum. High-energetic particles show an efficiency of about 97%. Secondary tracks from D⁺ decay have momentum larger than 1 GeV/c and, in addition, come from the target region, which can be exploited during the reconstruction; therefore, they have an even higher efficiency of 99%. It should be noted that only simple Gaussian smearing of the hit position was used in these investigation, and no double hit effects in the sensor were considered. Most of the other secondary tracks are low-energetic tracks, which suffer significant multiple scattering in the detector material. The efficiency for these low-energetic tracks is about 82%. Particles with momentum lower than 100 MeV/c are mostly out of the geometrical acceptance of the STS detector. Splitting of reconstructed tracks into short parts is negligible. The level of wrongly reconstructed tracks (ghost tracks) is about 3%;

these tracks are similar to short tracks of low-energetic particles.

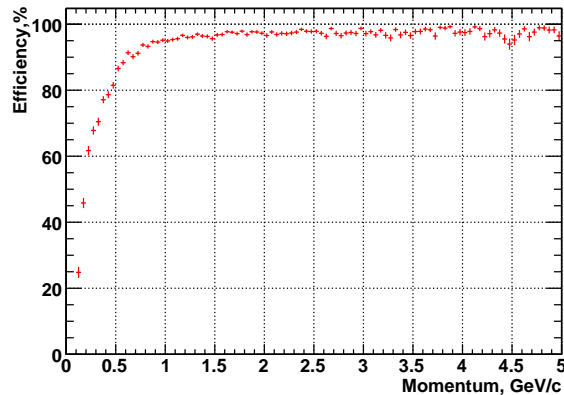


Figure 2: Track reconstruction efficiency of the standalone package as a function of momentum

The test of the SIMD KF track fit part of the package was done by comparing with results obtained with the SIMD KF track fitter of the CBMROOT framework. Both implementations of the fitting routine show similar results.

Testing of the KF Particle part of the package was performed using simulated data with D⁺ signal events only. The efficiency of D⁺ selection was found to be 48.9%, which is similar to the result obtained within the CBMROOT framework.

In conclusion, a standalone package for feasibility studies of the on-line event selection was created by extracting the corresponding routines from the CBMROOT framework. Comprehensive tests of the package show good agreement between the results obtained by the package and those of the corresponding routines of the CBMROOT framework.

References

- [1] Compressed Baryonic Matter Experiment, *Technical Status Report*, Darmstadt, 2005, <http://www.gsi.de/documents/DOC-2005-Feb-447.html>
- [2] S. Gorbunov, I. Kisel, and I. Vassiliev, *Analysis of D⁰ meson detection in Au+Au collisions at 25 AGeV*, CBM-PHYS-note-2005-001, <http://www.gsi.de/documents/DOC-2005-Jun-181.html>
- [3] I. Kisel, *Nucl. Instr. Meth. Phys. Res. A* 566 (2006) 85–88
- [4] S. Gorbunov et al., *Comp. Phys. Comm.* 178 (2008) 374–383
- [5] S. Gorbunov and I. Kisel, *Reconstruction of decayed particles based on the Kalman filter*, CBM-SOFT-note-2007-003, <http://www.gsi.de/documents/DOC-2007-May-14.html>

*I.Kisel@gsi.de

Track reconstruction in the MUCH and TRD detectors of CBM

A. Lebedev^{1,2}, C. Höhne¹, I. Kisel^{1,3}, and G. Ososkov²

¹GSI, Darmstadt, Germany; ²LIT JINR, Dubna, Russia; ³KIP, University of Heidelberg

In this report, we present new developments and results for the LIT track reconstruction package for CBM in the CbmRoot framework. The package is organized to be flexible with respect to feasibility studies of different physics channels and to the optimization of the detector geometries. The tracking software has been redesigned to make it more general and to simplify the support. The main components of the reconstruction package include track finding, fitting, propagation, and selection.

The track propagation algorithm has been improved considerably. The algorithm consists of track extrapolation, calculation of material effects, and the geometry navigator, managed by the track propagator which performs the transport of the track. The geometrical track extrapolation is governed by the equation of motion, which, in the presence of a magnetic field, is solved with the 4th order Runge-Kutta method with a parallel integration of the derivatives. In the absence of a magnetic field, a straight line model is used for the tracks. Material effects are taken into account by updating the track parameters and the covariance matrix, considering energy loss (ionization, bremsstrahlung and direct pair production) and multiple Coulomb scattering (Highland formula). The implementation of the geometry navigator is based on the ROOT geometry package which allows track propagation independently of the specific detector geometry. The track propagation algorithm is done in steps to allow a more precise calculation of material effects. The GEANE algorithm is also included in the track reconstruction as an alternative to the LIT propagation algorithm. A detailed description of the developed track propagation algorithm and its comparison with GEANE is given in Ref. [1].

The track finding algorithm was divided into two parts, namely track recognition and track selection. The track recognition is based on the track following method with branches and Kalman Filter. Reconstructed tracks are selected for their quality afterwards. The track selection is

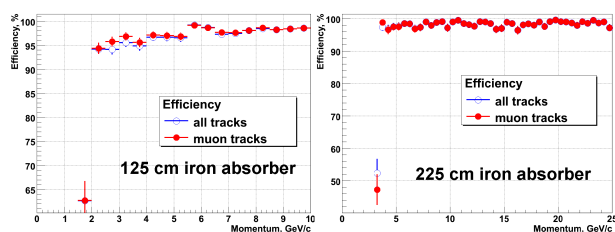


Figure 1: Track finding efficiency in MUCH in dependence on momentum for the compact geometry (left) and the standard geometry (right)

based on track quality criteria and checks for hits shared by different tracks.

The detailed layout of the detectors is still under discussion. In the high track density region of the TRD and MUCH stations, a pad layout is foreseen based on MWPC or GEM technology. For the upstream detector stations in MUCH, where track densities are low, straw tube chambers are under discussion. As these detectors provide not pad-like but strip-like hits, the tracking algorithm was modified in order to support all these structures.

The track reconstruction algorithm was tested for the standard TRD setup and three different MUCH geometries: "compact" (125 cm iron absorber, 6x2 pad detectors), "standard" (225 cm iron absorber, 6x3 pad detectors), and "straw" (same as "standard" but with straw tube detectors in the last 9 stations). For the testing of the algorithm, central Au+Au collisions at 25A GeV beam energy from UrQMD were used as background. For the reconstruction in TRD, 25 primary e^+ and 25 primary e^- with momenta $1 \text{ GeV}/c \leq p \leq 10 \text{ GeV}/c$ were embedded in each event. The performance in the MUCH system was evaluated by embedding 5 primary μ^+ and 5 primary μ^- per event with momentum $1.5 \text{ GeV}/c \leq p \leq 10 \text{ GeV}/c$ for the compact MUCH and $2.5 \text{ GeV}/c \leq p \leq 25 \text{ GeV}/c$ for the standard and straw MUCH, respectively.

The mean TRD track finding efficiency for reference tracks (primary tracks with $p > 1 \text{ GeV}/c$) is 96% at a ghost rate of 3%. The reconstruction efficiency for electrons is 91%. The MUCH track finding efficiency for the three discussed geometries is presented in Table 1; Fig. 1 depicts its momentum dependence.

In summary, the improved LIT track reconstruction package provides excellent results in the TRD and MUCH detectors. The reconstruction efficiency is only slightly different for the different MUCH layout options.

Table 1: Track finding efficiency for the compact, standard, and straw MUCH geometries in %

Geometry	Compact	Standard	Straw
All	96.2	97.5	95.4
Reference	97.1	97.6	95.4
Muon	96.8	97.5	95.4
Ghost	1.5	0.2	0.2

References

- [1] A. Lebedev and G. Ososkov, *LIT Track Propagation for CBM*, CBM-SOFT-note-2008-002 (2008), <http://www.gsi.de/documents/DOC-2008-Dec-182.html>

Study of the electron energy losses in the TRD

T. P. Akishina, O. Yu. Denisova, and V. V. Ivanov

LIT JINR, Dubna, Russia

We analyze and compare the electron energy loss measurements obtained during the test beam with $p=1.5$ GeV/c at GSI (February 2006) for a single-layer TRD prototype with Monte-Carlo (MC) simulations of the n -layered TRD realized in the CBMROOT framework for momenta in the range from 1 GeV/c to 13 GeV/c.

The distribution of the overall electron energy loss (dE/dx and transition radiation (TR)) in a TRD layer is approximated with high accuracy by the weighted sum of two log-normal distributions [1]

$$f(x) = A \left(\frac{a}{\sqrt{2\pi}\sigma_1 x} \exp^{-\frac{1}{2\sigma_1^2}(\ln x - \mu_1)^2} + \frac{b}{\sqrt{2\pi}\sigma_2 x} \exp^{-\frac{1}{2\sigma_2^2}(\ln x - \mu_2)^2} \right) + c, \quad (1)$$

where σ_1 and σ_2 are dispersions, μ_1 and μ_2 mean values, a and $b = 1 - a$ contributions of the first and second log-normal distributions, correspondingly, c is a shift parameter, and A is a normalizing factor.

As the behavior of the ionization losses of charged particles in a medium is well known, one can fix the parameters σ_1 and μ_1 in (1); they are obtained by fitting the dE/dx distribution for electrons. However, the TR losses are of more complicated character.

The approximation of the overall energy loss of electrons by eq. (1) permits to extract the individual contributions of dE/dx and TR (Fig. 1).

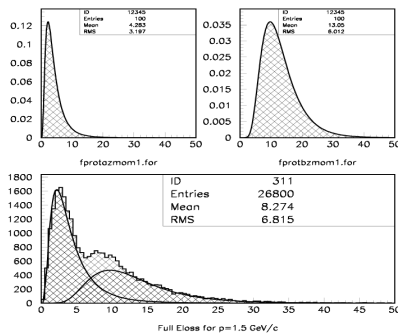


Figure 1: Distribution of e energy losses (bottom plot); contributions of dE/dx (top left plot) and TR (top right plot)

Table 1 shows that the statistical characteristics for the MC simulation and for the approximation by a weighted sum of two log-normal distributions with fixed parameters are very close. This demonstrates that our procedure of extraction of the TR contribution out of the distribution of the overall electron energy losses is correct.

Table 1: Comparison of mean values (m.v.) and RMS of the electron energy loss

p, GeV/c	1.5	3	5	7	9	11
m.v.(MC)	8.27	9.07	9.26	9.26	9.27	9.34
m.v.(fit)	8.20	9.05	9.13	9.21	9.23	9.32
RMS (MC)	6.82	7.36	7.49	7.47	7.48	7.50
RMS(fit)	6.65	7.28	7.21	7.32	7.36	7.42

A similar procedure was applied to the measurements obtained with the TRD prototype. In this case, the values of the parameters σ_1 and μ_1 were taken from an approximation of the dE/dx distribution for electrons with $p = 1.5$ GeV/c obtained by the MC simulation.

We compared the TR part for real measurements obtained with the TRD prototype with the MC simulation and found that in the region of $p = 1.5$ GeV/c, both the statistical characteristics (mean value and RMS) and the TR contributions to the overall energy loss differ significantly (Fig. 2). As a consequence, we may loose in the pion suppression factor (by about 10 times) and in the efficiency of the electron identification.

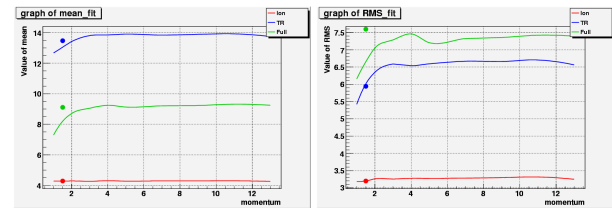


Figure 2: Mean value (left) and RMS (right) of the e^- energy loss from simulation as function of momentum. The red lines shows the contribution from dE/dx, the blue lines that of TR, and the green lines the overall energy loss. The circle denotes the result from prototype measurements.

It must be noted that the developed procedure of extracting the individual contributions of dE/dx and TR into the overall energy loss of electrons may permit one to bring the MC simulations into the agreement with real measurements.

References

- [1] E. P. Akishina et. al: *Distribution of energy losses for electrons and pions in the CBM TRD*, JINR Communications, E10-2007-158, Dubna, 2007

Systematic study of e/π identification with the TRD applying a multilayer perceptron

T. P. Akishina, O. Yu. Denisova, and V. V. Ivanov

LIT JINR, Dubna, Russia

We compare two neural networks (a multi-layered perceptron – MLP) from the JETNET3 and ROOT packages for the e/π separation using the Transition Radiation Detector (TRD). The method is based on a set of energy loss measurements $\{\Delta E_{i=1,\dots,n}\}$ in n TRD layers for π and e with momenta $1 \text{ GeV}/c \leq p \leq 11 \text{ GeV}/c$.

To obtain reliable and comparable results, it is important to correctly select the architecture of the network [1]. The choice of the MLP architecture includes the determination of a) the number of MLP layers and b) the number of neurons in each layer.

In our case, the network included $n = 12$ input neurons, 12 neurons in the hidden layer, and 1 output neuron. To choose the number of neurons in the hidden layer, we analyzed the error distribution, i. e. the difference between the target value (-1 for π and +1 for e) and the MLP output signal. It has to satisfy the following criteria: 1) to be symmetrical, 2) to have zero mean value, and 3) the dispersion must be minimal.

To obtain an acceptable level of pion suppression, it is required to transform the energy losses in the TRD layers to more “effective” variables:

$$\lambda_i = \frac{\Delta E_i - \Delta E_{mp}}{\xi_i} - 0.225, \quad i = 1, 2, \dots, n,$$

where ΔE_i is the energy loss in the i -th absorber, ΔE_{mp} is the most probable energy loss, and $\xi_i = \frac{1}{4.02}$ FWHM of the distribution of the pion energy loss [2]. This transformation permits to obtain a reliable level of e/π identification by the network after a minimal number of training epochs (about 50) in conditions of practical absence of fluctuations against the trend (top curve in Fig. 1). In case of original data, in spite of a large number of training epochs, the needed level of particle identification cannot be reached (bottom curve in Fig. 1).

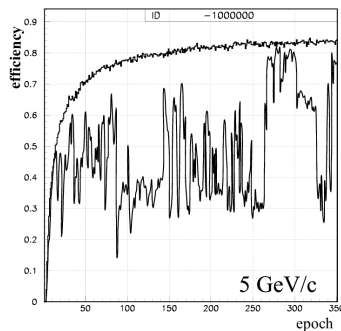


Figure 1: Efficiency of e/π identification by the MLP for the original (bottom curve) and the transformed (top curve) samples for momentum 5 GeV/c

We understand the efficiency of e/π identification as part of all processed $\{\Delta E_{i=1,\dots,n}\}$ sets for which the absolute value of difference between the target value and the MLP output signal does not exceed 0.05.

The formulas for enumerating the transformation parameters depending on the momentum are:

$$\Delta E_{mp}(p) = 0.000579p^3 - 0.01647p^2 + 0.1708p + 0.892,$$

$$\text{FWMH}(p) = 0.000687p^3 - 0.02038p^2 + 0.2181p + 1.98.$$

At the stage of the MLP testing, the event type is determined by the value of the output signal: when it does not exceed the preassigned threshold, then the event is assumed to be a pion, in the opposite case an electron. The dependence of the output threshold of the network on the momentum of the recorded particle is shown in Fig. 2.

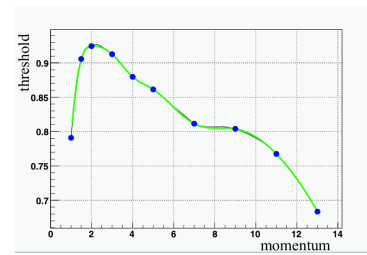


Figure 2: Threshold as function of momentum and its approximation by a third degree spline

To estimate the efficiency of e/π identification and pion suppression by MLP, the networks were trained for each momentum separately and with corresponding transformation parameters. Table 1 demonstrates that for a correctly chosen MLP architecture, both networks give close results. In the opposite case, the pion suppression factor for networks may be essentially different.

Table 1: Pion suppression factors for 90% electron efficiency applying the MLP

p [GeV/c]	1	1.5	2	5	7	9	11
JETNET	158	330	431	470	344	410	303
ROOT	145	326	431	470	336	371	318

References

- [1] N. A. Ignat'ev, *Selection of the minimum configuration of the neural networks*, Comp. Techn., t. 6, No. 1 (2001), p. 23 - 28
- [2] E. P. Akishina et al.: *Electron/pion identification in the CBM TRD applying a multilayer perceptron*, JINR Communications, E10-2007-17, JINR, Dubna, 2007

Electron identification in the CBM experiment

S. Lebedev^{*1,2}, C. Höhne¹, and G. Ososkov²

¹GSI, Darmstadt, Germany; ²JINR LIT, Dubna, Russia

In this contribution, we present systematic studies and improvements for electron identification in the CBM experiment.

A RICH ring recognition algorithm based on the Hough Transform (HT) [1] was improved especially for a high ring density environment. This is necessary since an optimization of the RICH detector for CBM with respect to minimization of its dimensions was done [2], resulting in an increased ring density in the photodetector plane of this "Compact RICH".

In systematic studies of the ring recognition algorithm, different parameters were varied. Up to 120 e^+ and 120 e^- were simulated for each event. The number of rings in such events is roughly 250; consequently, the majority of rings in the inner and central part of the RICH PMT plane overlap. The ring finding efficiency varies from 91% for rings with more than 5 hits to 95% for rings with more than 15 hits. So far, for the H8500 photodetector only the quantum efficiency was implemented, however an additional reduction of the photodetector collection efficiency (CE) by 30% might be realistic. In this case, the ring finding efficiency drops by 2% in comparison to 100% CE. The ring finding efficiency was also investigated in dependence on the number of hits per ring and the ratio of the minor half axis (B) and major half axis (A) of the ellipse, as typically the rings are slightly distorted. It was found that the efficiency drops to less than 80% once the number of hits per ring reaches a low probability value, i. e. the mean value minus 2-RMS. The efficiency in dependence on the B/A ratio stays constant in the range between 0.8 and 1 and drops rapidly for smaller ratios. The B/A ratio is thus an important parameter for the Compact RICH design [2].

An algorithm for electron identification in the RICH detector based on an Artificial Neural Network (ANN) was implemented. After studying the distributions of different parameters related to the RICH rings, 9 of them were chosen, among them major and minor half axes and the rotation angle. These parameters are used as input to a trained ANN. It shows somewhat better results in comparison to the standard cuts (see Table 1).

A systematic study of electron and pion identification in the TRD was also performed. The ANN method [3] was used for this task. The dependence of energy loss on momentum was investigated. Three approaches of ANN training were proposed and investigated. The momentum information is needed for two of these approaches.

The electron identification algorithm in the TRD was adopted to identify electrons which have 6 to 12 hits in the TRD. This is necessary because 1) different geometries

Table 1: Electron identification efficiency and pion suppression averaged over all momenta

	Standard RICH		Compact RICH	
	Std. cuts	ANN	Std. cuts	ANN
RICH, eff. %	87.1	90.3	81.9	83.8
RICH, π supr.	240	250	110	250
RICH+TRD, efficiency %	81.0	83.3	73.4	74.6
RICH+TRD, π suppression	9800	10500	6800	13000

with different number of layers have to be investigated; 2) detector inefficiencies will lead to losses of hits; 3) tracks which do not pass through all layers should also be identified; 4) track finding algorithm might find only a part of track. The algorithm was also optimized for an alternative geometry (Münster-Bucharest), which uses a double gas layer.

These improved methods result in a high purity and efficiency of reconstructed electron rings (see Table 1). For momenta above 2 GeV/c, the ring reconstruction efficiency for electrons embedded in central Au+Au collisions at 25 AGeV beam energy is 95%, resulting in an electron identification efficiency of 90% at a pion suppression factor of 500. Including information from the TRD, a pion suppression of 10^4 is reached at 80% electron efficiency (see fig. 1).

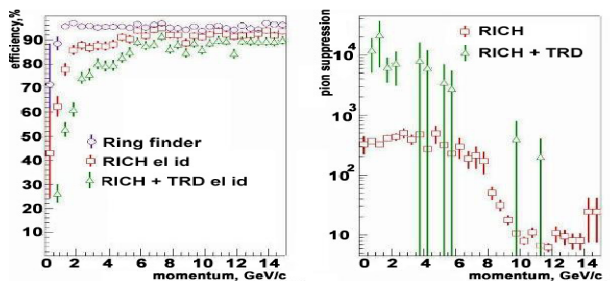


Figure 1: Efficiency of electron identification (left) and pion suppression factor (right) as function of momentum for electrons embedded in central Au+Au collisions at 25 AGeV beam energy and the standard RICH layout

References

- [1] S. Lebedev et al., CBM-RICH-note-2008-001, GSI, 2008
- [2] C. Höhne, *CBM-RICH layout optimization*, CBM Progress Report 2007, Darmstadt, 2008, p. 17
- [3] E. Akishina et al., JINR Comm. E10-2007-17, Dubna, 2007

*s.lebedev@gsi.de

Wavelet application for handling invariant mass spectra

S. Lebedev^{*1,2} and G. Ososkov²

¹GSI, Darmstadt, Germany; ²JINR LIT, Dubna, Russia

Wavelet transformation is known as an efficient multi-scale technique to reduce the presence of statistical noise and then extract physical parameters from the obtained smoothed form [1, 2]. The one-dimensional wavelet transform (WT) of a signal $f(x)$ with the wavelet function ψ has a biparametric form:

$$W_\psi(a, b)f = \frac{1}{\sqrt{C_\psi}} \int_{-\infty}^{\infty} \frac{1}{\sqrt{|a|}} \psi\left(\frac{b-x}{a}\right) f(x) dx, \quad (1)$$

where $C_\psi < \infty$ is the normalization constant. A scale parameter a characterizes the dilatation, and b is the translation in time or space. Due to freedom in the choice of the wavelet function ψ , many different types of wavelets were invented.

Since any real signal to be handled by a computer is discrete, *discrete wavelets transforms* (DWT) look as a good tool to deal with experimental data. The DWT concept was built by Mallat [3] as a multi-resolution analysis. It consists in representing given data as a signal decomposition into basis functions φ and ψ , which must be compact. Developing the corresponding C++ DWT software, we focused on the so called DWT shrinking approach [4]. Wavelet shrinkage means that certain wavelet coefficients are reduced to zero $W_\psi = 0$, if $|W_\psi| < \lambda$. So one can eliminate from the wavelet transformed invariant mass spectrum some of the objectionable high and low frequencies, which will filter the corresponding part of the original signal after the inverse transform. Our innovation is the *adaptive shrinkage*, i.e. setting $\lambda_k = 3\sigma_k$, where k is the decomposition level of the scale parameter; σ_k is the RMS of W_ψ for this level. Very promising results for invariant mass spectra simulated for low-mass dileptons (muon channel) were obtained by our DWT approach to observe ω and ϕ mesons as shown in figure 1.

Another study was devoted to applying the family of continuous wavelets, of which the *Gaussian wavelets* (GW) are normalized derivatives of the Gauss function $g(x, A, x_0) = A \exp\left(-\frac{(x-x_0)^2}{2\sigma^2}\right)$. When a signal is bell-shaped, it can be approximated by a Gaussian. Then it can be derived analytically that its wavelet transformation looks as the corresponding wavelet [5]. For instance, considering for simplicity $G_2(x) = (1-x^2)e^{(-x^2/2)}$ one has $W_{G_2}(a, b)g = \frac{Aa^{5/2}\sigma}{(a^2+\sigma^2)^{3/2}} G_2\left(\frac{b-x_0}{\sqrt{a^2+b^2}}\right)$, the maximum of which on the scale parameter a is $a_{max} = \sqrt{5}\sigma$ and can be used to estimate the σ parameter.

Thus, one can work directly in the wavelet domain instead of the time/space domain and use this analytical for-

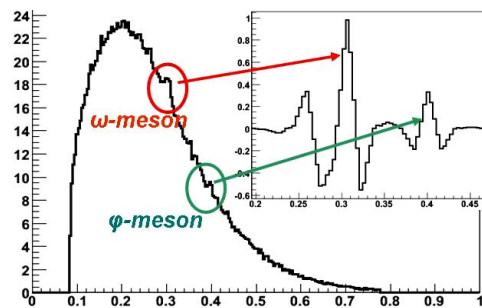


Figure 1: Low-mass dileptons (muon channel) invariant mass spectra after adaptive shrinking with specially chosen multipliers M in $\lambda_k = M\sigma_k$ for each level k of DWT

mula for the $W_{G_2}(a, b, x_0, \sigma)g$ surface in order to fit it to the surface, obtained by transforming a real invariant mass spectrum by the G_2 wavelet. The most remarkable point is: Since the parameters in question x_0 and σ can be estimated directly in the G_2 domain, *we do not need the inverse transform!* In [5], we choose a GW of 8th order to study a resonance structure in the invariant mass distributions of $\gamma\gamma$ pairs without background subtraction. Results of the continuous wavelet analysis presented in [5] confirm a peak observed at $m_{\gamma\gamma} \approx 360$ MeV in the $\gamma\gamma$ invariant mass distribution obtained within the standard method with the subtraction of the background from mixing events.

References

- [1] I. Daubechies, *The wavelet transform, time frequency localization and signal analysis*, IEEE Trans. Inform. Theory 36 (1990) 961
- [2] G. Ososkov and A. Shitov, *Comp. Phys. Comm.* 126 (2000) 149
- [3] S. A. Mallat, *Theory for multi-resolution signal decomposition: the wavelet representation*, IEEE Trans. Pattern Analysis and Machine Intelligence (1989)
- [4] I. Johnstone and B. Silverman, *Boundary coiflets for wavelet shrinkage in function estimation*, J. Appl. Probab. Volume 41A, Issue (2004), 81-98
- [5] K. U. Abraamyan *et al.*, arXiv:0806.2790v3[nucl/ex]

*s.lebedev@gsi.de

CBM publications 2008

- K. Davkov *et al.*
[Development of segmented straws for very high-rate capability coordinate detector](#)
Nucl. Instr. Meth. Phys. Res. **A 584** (2008) 285
- M. Klein-Bösing *et al.*
[Position resolution of a high efficiency transition radiation detector for high counting rate environments](#)
Nucl. Instr. Meth. Phys. Res. **A 585** (2008) 83
- J. Adamczewski *et al.*
[Data Acquisition Backbone Core DABC](#)
IEEE Trans. on Nucl. Science **178** (2008) 251
- S. Gorbunov *et al.*
[Fast SIMDized Kalman filter based track fit](#)
Comp. Phys. Comm. **178** (2008) 374
- J. M. Heuser
[The Compressed Baryonic Matter experiment at FAIR](#)
J. Phys. **G35** (2008) 044049
- P. Senger
[Probing dense matter with strangeness production in nuclear collisions](#)
Nucl. Phys. **A804** (2008) 274
- S. Chattopadhyay
[Physics at High baryon density at FAIR](#)
J. Phys. **G35** (2008) 104027
- C. Höhne
[Di-lepton spectroscopy in CBM](#)
J. Phys. **G35** (2008) 104160
- C. Höhne *et al.*
[Development of a RICH detector for electron identification in CBM](#)
Nucl. Instr. Meth. Phys. Res. **A 595** (2008) 187
- D. Bertini *et al.*
[The FAIR simulation and analysis framework](#)
J. Phys. Conf. Ser. **119** (2008) 032011
- V. Friese
[The CBM Experiment at FAIR](#)
PoS(CPOD07)056
- M.S. Borysova *et al.*
[Silicon tracker for the compressed baryonic matter experiment](#)
Nuclear Physics and Atomic Energy **3(25)** (2008) 94

In press

- M. Golubeva *et al.*
[Longitudinally segmented lead/scintillator hadron calorimeter with micro-pixel APD readout](#)
Nucl. Instr. Meth. Phys. Res. **A 598** (2009) 268
- D. Gonzalez-Diaz *et al.*
[The role of the resistive plate response function in bringing an RPC to a stationary situation](#)
in press Nucl. Instr. Meth. Phys. Res.

CBM Notes 2008

Public notes

- S. Lebedev, G. Ososkov and C. Höhne
[Ring recognition in the CBM RICH detector](#)
CBM-RICH-note-2008-001
- A. Lebedev and G. Ososkov
[Event Reconstruction in the CBM TRD](#)
CBM-SOFT-note-2008-001
- E.A. Matyushevsky *et al.*
[Superconducting Dipole Magnet for CBM](#)
CBM-note-2008-001
- A. Lebedev and G. Ososkov
[LIT Track Propagation for CBM](#)
CBM-SOFT-note-2008-002
- V. Pozdnyakov and Yu. Vertogradova
[Hadron azimuthal correlations to be studied at CBM setup](#)
CBM-PHYS-note-2008-001

Internal notes

- A. Marie
[Towards a Monte Carlo Platform for the CBM Experiment at FAIR Facility](#)
CBM-SOFT-note-internal-2008-001
- K. Piasecki, B. Sikora and K. Wisniewski
[Optimization of the shape of the reduced-size muon detector and its influence on the efficiency of the muon tagging in CBM](#)
CBM-MID-note-internal-2008-001

CBM Meetings, Workshops, Conferences

- [CBM-India Meeting](#)
Jammu, India, 12 - 15 February 2008
- [11th CBM Collaboration Meeting](#)
GSI Darmstadt, 26 - 29 February 2008
- [2nd joint meeting of CBM and MPS STS working groups](#)
IHEP Protvino, 5 - 6 June 2008
- [3rd CBM Indian Collaboration Meeting](#)
VECC Colcata, 22 - 23 July 2008
- [12th CBM Collaboration Meeting](#)
JINR Dubna, 13 - 18 October 2008

List of CBM member institutions

- Aligarh, India, Department of Physics, Aligarh Muslim University
- Beijing, China, Department of Engineering Physics, Tsinghua University
- Bergen, Norway, Department of Physics, University of Bergen
- Bhubaneswar, India, Institute of Physics
- Bucharest, Romania, National Institute for Physics and Nuclear Engineering
- Bucharest, Romania, Atomic and Nuclear Physics Department, University of Bucharest
- Budapest, Hungary, Eötvös University
- Budapest, Hungary, KFKI
- Chandigarh, India, Department of Physics, Panjab University
- Coimbra, Portugal, LIP
- Darmstadt, Germany, GSI
- Dresden, Germany, FZD, Institut für Strahlenphysik
- Dubna, Russia, JINR-LHE
- Dubna, Russia, JINR-LPP
- Dubna, Russia JINR-LIT
- Frankfurt, Germany, Institut für Kernphysik, Universität Frankfurt
- Gatchina, Russia, PNPI
- Guwahati, India, Department of Physics, Gauhati University
- Hefei, China, Department of Modern Physics, University of Science & Technology of China
- Heidelberg, Germany, Kirchoff-Institut für Physik, Universität Heidelberg
- Heidelberg, Germany, Physikalisches Institut, Universität Heidelberg
- Heidelberg, Germany, Zentrales Institut für Technische Informatik, Universität Heidelberg
- Jaipur, India, Physics Department, University of Rajasthan
- Jammu, India, Department of Physics, University of Jammu
- Katowice, Poland, University of Silesia
- Kharagpur, India, Department of Physics and Meteorology, Indian Institute of Technology
- Kolkata, India, High Energy Physics Division, Saha Institute of Nuclear Physics
- Kolkata, India, Department of Physics and Department of Electronic Science, University of Calcutta
- Kolkata, India, Variable Energy Cyclotron Centre
- Kraków, Poland, AGH University of Science and Technology
- Kraków, Poland, Jagiellonian University
- Kyiv, Ukraine, Taras Shevchenko National University of Kyiv
- Kyiv, Ukraine, High Energy Physics Department, Kiev Institute for Nuclear Research (KINR)
- Moscow, Russia, Institute for Nuclear Research
- Moscow, Russia, ITEP
- Moscow, Russia, SINP, Moscow State University
- Moscow, Russia, Kurchatov Institute
- Moscow, Russia, MEPhi
- Münster, Germany, Institut für Kernphysik, Universität Münster
- Nikosia, Cyprus, Cyprus University
- Obninsk, Russia, Obninsk State University of Atomic Energy
- Prag, Czech Republic, Technical University
- Protvino, Russia, IHEP
- Pusan, Korea, Pusan National University
- Rez, Czech Republic, Czech Academy of Sciences
- Seoul, Korea, Korea University
- Split, Croatia, University of Split
- Srinagar, India, Department of Physics, University of Kashmir
- St. Petersburg, Russia, Khlopin Radium Institute (KRI)
- St. Petersburg, Russia, St. Petersburg State Polytechnic University
- Strasbourg, France, Institut Pluridisciplinaire Hubert Curien IN2P3-CNRS/ULP (IPHC)

- **Varanasi, India, Department of Physics, Banaras Hindu University**
- **Warszawa, Poland, University, Nuclear Physics Division**
- **Wuhan, China, Institute of Particle Physics, Hua-zhong Normal University**
- **Zagreb, Croatia, Rudjer Bošković Institute**

Contacts

Spokesman

Peter Senger

[\(p.senger@gsi.de\)](mailto:p.senger@gsi.de)**Technical Coordinator**

Walter Müller

[\(w.f.j.mueller@gsi.de\)](mailto:w.f.j.mueller@gsi.de)**Physics Coordinator**

Volker Friese

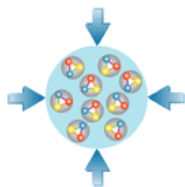
[\(v.friese@gsi.de\)](mailto:v.friese@gsi.de)**Chairman of the Collaboration Board**

Mihai Petrovici

[\(mpetro@ifin.nipe.ro\)](mailto:mpetro@ifin.nipe.ro)

Management Board

N. Herrmann, F. Rami, D. Röhrich, J. Stroth, J. Wessels, Yu. Zaitsev

<http://www.gsi.de/fair/experiments/CBM>



CBM-India Meeting and ROOT @ Heavy-Ions
International Workshop, Jammu, February 12-16, 2008



CBM-MPD Silicon Tracking System Consortium:
2nd Work Meeting, Protvino, Russia, June 5-6, 2008



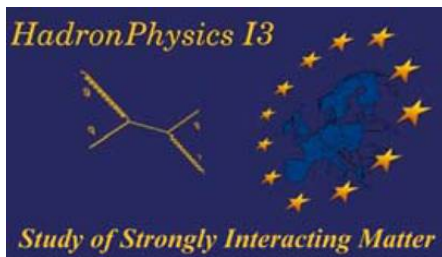
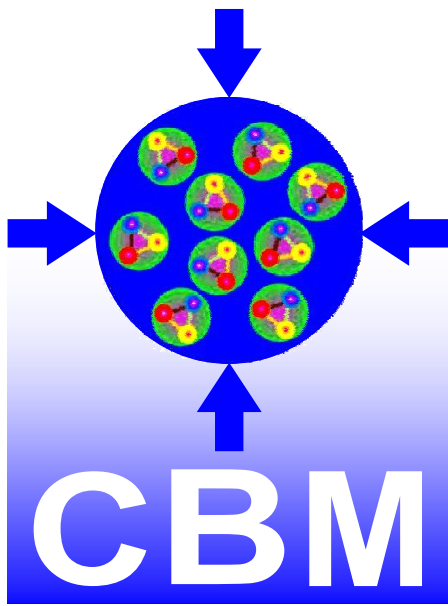
Beam test, GSI, September 28-30, 2008



12th CBM collaboration meeting, October 18, 2008



CBM silicon tracking detector prototype
in the SVD-2 experiment, IHEP Protvino, Russia,
November 19 - December 1, 2008



This work is supported by the EU Integrated Infrastructure Initiative Hadron-Physics Project (I3HP) under Contract number RII3-CT-2004-506078, by INTAS Ref. № 06-100012-8781, and by the German Federal Ministry for Education and Research.

